UNIVERSITÀ DEGLI STUDI DI TRIESTE

UNIVERSITÀ DEGLI STUDI DI TRIESTE

XXXV CICLO DEL DOTTORATO DI RICERCA IN

FISICA

Borsa finanziata dal Dipartimento di Fisica su fondi Elettra – Sincrotrone Trieste S.C.p.A.

Schemes for the production of ultra-short photon pulses (sub-10 fs) in the FERMI Free-Electron Laser

Settore scientifico-disciplinare: FIS/03

DOTTORANDO
Filippo Sottocorona

COORDINATORE
PROF. Francesco Longo

SUPERVISORE DI TESI
PROF. Luca Giannessi

ANNO ACCADEMICO 2021/2022

Contents

Chapter 1

Introduction

Free-electron lasers (FELs) are capable of generating intense pulses of a few fs from VUV to hard X-rays [1, 2, 3, 4, 5, 6, 7, 8]. This possibility is opening a wide range of new scientific opportunities. The time scale of a few fs allows probing ultrarapid, out-of-equilibrium dynamics, driving transitions in regimes where excitation is not exhausted by fast decaying side channels, such as the Auger effect [9]. Ultrashort pulses can probe THz-stimulated dynamics, such as coherent phonons [10] or collective excitations in condensed matter, paving the way for the observation of coherent, field-dependent phenomena. When sort pulses are combined with a correspondingly high peak power, nonlinear optics is possible at EUV/soft X-ray wavelengths. These are examples showing the importance of generating short intense pulses at a FEL facility such as FERMI. In this thesis work, we discuss some of the schemes available to produce ultrashort photon FEL pulses. The work starts from a briefly review from analytical and theoretical point of view, highlighting the limitation in the short pulse generation due to the finite gain bandwidth of a FEL. FERMI, as a seeded FEL source, aims at generating close to the Fourier limit pulses [5, 6]. The interplay between pulse duration, spectral purity, and quality of the electron beam longitudinal phase space are analyzed. Several options available for the production of short pulses are then addressed from a computational point of view. In some promising cases it was finally possible to carry out experiments which were compared to the theoretical predictions. In the last three years, we have deepened the analysis of mainly two schemes: the superradiance cascade scheme[11, 12, 13, 14], consisting in multiple harmonic jumps, with a small harmonic number, to quickly saturates the bunch, reaching the overbunched condition and to allow just the first peak to fully evolve in the superradiant evolution. This condition allows to reach a few fs pulses, due to the shortening of the bunching factor and the overbunched condition. The second peak is cleared by the out-of-resonance condition. The second one is the spoiled beam condition [15], in which the longitudinal length is reduced by the implementation of the scraper, which is composed by two blades that scatter away the tails of the electron charge distribution. By removing the outer charge, only the core distribution is allowed to propagate, resulting

in a shorter electron bunch. We have proved that this will also reduce the FEL pulse duration. The first method, superradiance, was tested experimentally at FERMI in several conditions. This method has some limitations in terms of applicability, requiring specific undulator configurations to properly work, but it is now considered sufficiently mature to be applied in user experiments. The second method seems promising and applicable in the long wavelength range of FERMI but is still in the stage of simulation work. The personal contribution on the development of these scheme at FERMI starts from the analysis of the experiment carried out at November 2019, the simulations provided in Chapter 6 and all the experiments/simulations concerning the spoiled beam.
Before discussing the FEL properties, we want to briefly review some of the major schemes and concepts that concerns the production of ultrashort FEL pulses.

Chapter 2

Generation of short pulses in FELs

The ability to generate short pulse duration from lasers has become increasingly important in a wide range of fields, as it allows researchers to study faster dynamics and interactions. In particular, the use of femtosecond and attosecond pulses has enabled the observation of dynamics on the atomic and electronic timescales in fields such as chemistry, atomic physics, and solid state physics. This has led to a deeper understanding of these processes and has opened up new possibilities for research and applications.

Ultrafast processes in atomic physics started with the real-time observation of the femtosecond Auger decay in krypton, in which the attosecond dynamics was firstly introduced [17]. From this, other important results in the field of ultrafast atomic physics has been achieved, such as the real-time observation of electron tunneling [18] and the measurement of temporal delays of the order of a few tens of attoseconds in the photoemission of electrons from different atomic orbitals of neon [19] and argon [20]. Attosecond pulses allowed quantum mechanical electron motion and its degree of coherence to be measured in atoms by using attosecond transient absorption spectroscopy [21].

In the past few years, attosecond pulses have also been used to measure ultrafast electronic processes in simple molecules [22]. Sub-femtosecond electron localization after attosecond excitation has been observed in H2 and D2 molecules [23], and control of photo-ionization of D2 and O2 molecules has been achieved by using attosecond pulse trains (APTs) [24, 25]. More recently, an APT, in combination with two near-infrared fields, was used to coherently excite and control the outcome of a simple chemical reaction in a D2 molecule [26].

In ultrafast pump–probe experiments, the pump pulse is used to clock with femtosecond accuracy the atomic or molecular motion. The second femtosecond pulse, can be used to probe the time evolution of the system. Since the synchronization of a few femtoseconds can be achieved in a straightforward way using relatively simple split-and-delay stages, the sequence of snapshots taken

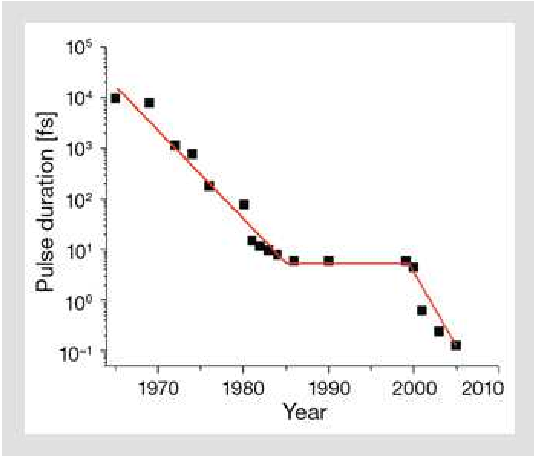

Figure 2.1: Pulse duration achievable from laser source over the years [16]

at variable t delays can be used as a stroboscopic probe of dynamics in real time.
The femtosecond dynamics [27] of electrons in metals has been given much attention. Several experimental methods have been developed that allow determining the relaxation time and relaxation length of an excited electron. A very important point was the invention of methods that allow directly investigating the time characteristics of the dynamics of excited states and, first and foremost, the method of time resolved two-photon photoemission spectroscopy (TR2PPE). In this method, the first (pumping) photon excites an electron into an intermediate state, and the second photon (probing photon), which comes after a certain time delay, transfers the electron from the intermediate state to the vacuum. Such experiments can be carried out at a low intensity of laser radiation, when investigating the dynamics of excitation of a single electron, or at a high intensity, when studying collective excitation. From the considerations reported above, it is therefore important to develop femto to attoseconds laser source capable of probing new dynamics. In the following we are going to review a few of the most common schemes and setups proposed and in some cases implemented in order to produce short pulses in FELs.

2.1 Electron beam Manipulation

Several methods were proposed to generate femto and sub-femtosecond photon pulses in FELs, by manipulating and/or shaping the electron bunch, before starting the exponential amplification in a FEL. These methods generally apply to self amplified spontaneous radiation FELs, where the pulse duration depends only on the electron beam parameters, but can in principle extended to seeded

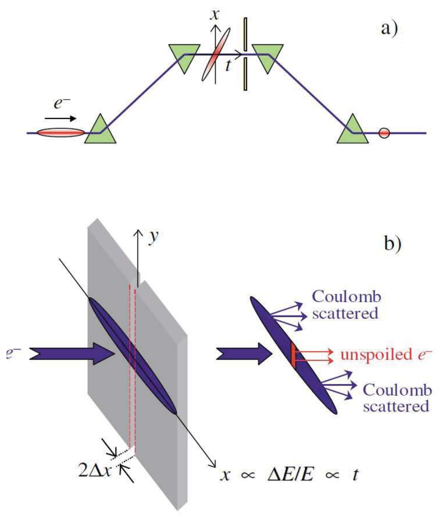

Figure 2.2: Description of the scraping technique. a) the electron bunch is tilted in a bunch compressor and then b) passes through two blades that scatter the tails and leaves unspoiled electrons, compatible with the aperture of the scraper $2\Delta x$. [15]

FEL's also as the duration of the lasing region over the electron beam dominates over the seed properties, i.e., if we consider a bunch length of 10fs and a seed pulse of 50fs, the emitted photon pulse will not generally have a duration larger than 10fs if supported by the FEL amplification gain bandwidth. From this simple consideration we can conclude the importance of the electron shaping techniques in shortening the FEL pulse duration.

2.1.1 Slotted-foil method

The first scheme that we review is the slotted-foil method, proposed in [15]. The idea uses the fact that in a magnetic bunch compressor, the electron bunch is tilted with a large angle, from the longitudinal axis to the traversal plane. In this way the longitudinal length is exchanged by the transverse length.
In Fig. 2.2 is reported the representation of the scheme. The tilting of the electron bunch is necessary because, usually, the longitudinal length of the beam is much greater than the transverse sizes. After this rotation, a scraper, which is a device made by two symmetrical blades, with respected of the longitudinal axis, is placed. The scraper has a vertical aperture that allows the core electrons in the bunch to be left unspoiled or unscattered. The tail electrons suffer the presence of the blade and are scattered by Coulomb scattering and the the traversal emittances are increased. In this way, the can manipulate the longitudinal length of the beam, decreasing it by the same ratio between the

aperture of the scraper and the unmodified transverse rms, therefore

$$\Delta t_{\mathrm{FWHM}} \approx \frac{2\Delta x}{\sigma_x}\sigma_t, \tag{2.1}$$

where σ_t is the longitudinal length and σ_x is the transverse length, both without the scraper. [15] showed that it is possible to keep the peak current constant, while lowering the aperture of the scraper. This suggests a linearity behavior between the unspoiled charge and the longitudinal length of the unscattered electrons. This is very important, since the peak current plays a crucial role in the gain of a FEL and this linearity assures the possibility to keep the same gain, while lowering the bunch duration. Further, they provide evidences of high peak power photon pulses with 2fs FWHM pulse duration in a SASE FEL with the possibility to reach sub-femtosecond pulses. This scheme was also studied at FERMI and in Chapter 7 we will provide both computational and experimental results.

2.1.2 Single-spike FEL operation

The idea of a ultra-low charged beam provided further ideas. While the scarpering technique relies on the Coulomb scattering in order to cut the tails in the charge distribution, it has the negative side of generating a lot of radiations, which are dangerous also for the electronic equipment. Another way for generating bunch with a low value of charge is presented in [28]. Here, the choice of the bunch length, dictated by the physics of the FEL and the two downstream compression processes, deduces the correct scaled beam charge Q that should be used to obtain the desired pulse length. Therefore, by the machine constrains a specific amount of charge Q is extracted by a RF gun, from the photoinjector. Then, the scaling laws described in the paper allow the evaluation of the beam properties. After the two compressions, it is possible to achieve a narrow high-peaked profile for the current. Finally, from a 1pC bunch with 28fs of longitudinal length, the authors provide the generation of very intense photon pulses (over 100MW of peak power), with an high level of spectrum stability and 12fs of pulse duration.

2.1.3 Enhanced SASE

Another scheme that relies in the manipulation of the beam prior to the undulators line is the one proposed by [29]. The authors suggest to induce an energy modulation in the beam, with an external optical laser pulse, with a short pulse duration (∼50fs). The beam modulated is then accelerated up to the nominal energy, without impacting negatively in the modulated region. After the linac, a dispersive section generates the microbunching structure and an enhanced peak current profile, compatible to the modulated region.
In Fig. 2.3 is reported the simulated current profile (plot b)), after the chicane, in the region correspondent region of the energy modulation (plot a)). As we said, the current plays a crucial role in the gain of an FEL process, therefore,

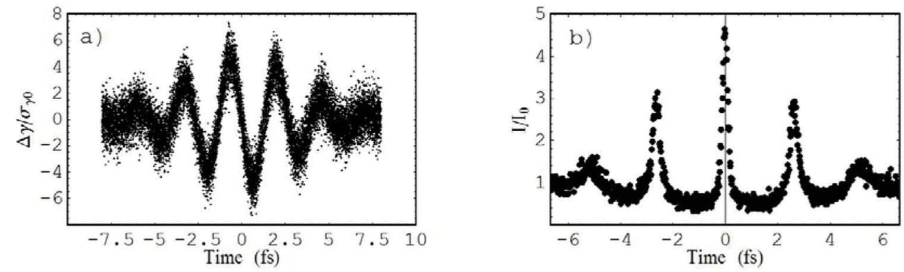

Figure 2.3: Energy modulation, impressed by a laser pulse in a wiggler magnet, and correspondents peak current resulting from a simulation of the proposed scheme[29]

by shaping this profile, it is possible to generate single spikes with a very short FWHM. This behavior will be impressed in the peak power profile, allowing the generation of very intense, ultrashort FEL pulses. Here the authors show that it is possible to obtain FEL pulses with a FWHM duration of

$$\Delta\tau \approx \frac{4M_G\lambda_x}{c},$$

where M_G is the gain length of the process, in number of wiggler periods, λ_x is the wavelength of the external laser used for imprinting the energy modulation and c is the speed of light. Further, it shows that this result provides photon pulses very close to the FTL condition and with a higher degree of temporal coherence, since the SASE output from a microbunch with length Δz_0 has the condition $\Delta z_0 \leq 2\pi M_G\lambda_x$[30].

2.1.4 Laser heater beam spoiler

A somehow complementary scheme to the one reported above, uses a laser heater to increase the energy spread in the tails of the electron bunch to suppress any kind of FEL emission [31]. The laser is applied before the two-stage compression. In this way, the electron beam has a central region in which the electrons are at their nominal energy, with a natural energy spread, and two tails with a higher value of energy spread. The large energy spread is necessary to put out of resonance the tail electrons, while the core electrons are on resonance. The two compressors enhance the effect,since the energy spread is increased by the same compression factor C. This allows the selection of a variable region of unspoiled electrons, therefore the final FEL pulse duration will be lowered. Despite the setup, the authors show the possibility to fine control the parameters, to obtain pulses with a time duration lowered by a factor 5 (see Fig. 2.4).

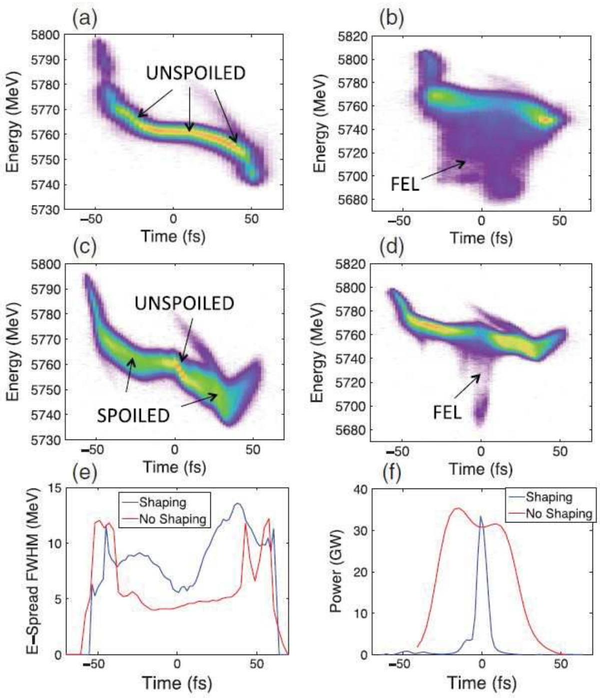

Figure 2.4: Experimental results of the LH shaping scheme [31]. (a),(b) Longitudinal phase space of the electron bunch with lasing suppressed and lasing on, respectively, for the unshaped electron bunch. (c),(d) Longitudinal phase space of the electron bunch with lasing suppressed and lasing on, respectively, for the temporally shaped electron bunch. (e) Slice energy spread as a function of time for the unshaped electron bunch (red) and the temporally shaped electron bunch (blue). (f) X-ray profile for the unshaped electron bunch measured from the energy loss to the FEL (red) and the shaped electron bunch (blue).

2.1.5 Chirp and taper

The generation of a isolated, attosecond spike radiation pulses in a single pass FEL, operating in SASE mode, has been proposed also by [32]. In this paper, the authors provide a combination of energy chirp in the electron beam and a strong, negative taper in the undulators line. The energy chirp is necessary to detune the beam's local resonant frequency, while the undulators tapering allows the continuous gain of a spike initiated in the rear of the bunch as it moves forward. Without tapering, the radiation emitted would exit the local gain bandwidth. The chirp is applied by using an external seed laser and a modulator to energy modulates the electrons. Then, using an appropriate undulator taper, only a short slice around zero-crossing produces powerful FEL pulse. The main part of the bunch is unmodulated and suffers from the presence of strong negative undulator tapering. With this scheme, the author provided simulated results of 100GW, 200as pulses in an isolated single spike. More recent, [33] provided experimental demonstration of this scheme, showing one order of magnitude of power emitted, between tapered and untapered condition and with a FTL pulse duration of ∼50fs at 540nm.

2.2 Seeded FELs

2.2.1 Chirped-Pulse Amplification

Acting directly on the e-beam is a common technique for SASE FELs. If we consider seeded FELs then we can expand the range of possibilities to provide shorter pulses. A scheme that relies on particular characteristics of the seed is the Chirped Pulse Amplification (CPA). This is a technique that was first developed in atomic laser research in the late 1980s by Mourou and Strickland [34]. Ultrashort pulses contain a broad spectral bandwidth according to their Fourier transform. This fact enables the possibility to add a phase shift to different frequencies or wavelengths, using a grating pair with a specific characteristics of the medium, of the laser pulse just after its generation in a mode-locked laser cavity. The result is a stretched pulse containing a correlation between the longitudinal position and the frequency, i.r.a chirp. The pulse has in this case a lower peak power and can be amplified without damaging optical components. After amplification the pulse can be compressed to very short duration by adding a spectral phase with an opposite sign to that introduced by the grating. To demonstrate the effectiveness of the CPA technique, the authors performed experiments using a Ti:sapphire laser system. They were able to increase the peak power of the laser pulse by a factor of 1000, from 50 kW to 50 MW, without causing damage to the amplifying material. In FELs the idea is similar, we introduce a chirp in the seed laser. The FEL photon pulse inherits the amplitude and phase from the seed laser. The undulators line amplifies the chirped pulse that should have a duration comparable to the entire electron bunch. A larger fraction of the bunch charge interacts with radiation with respect to the bunch fraction that would have interacted with the short pulse.

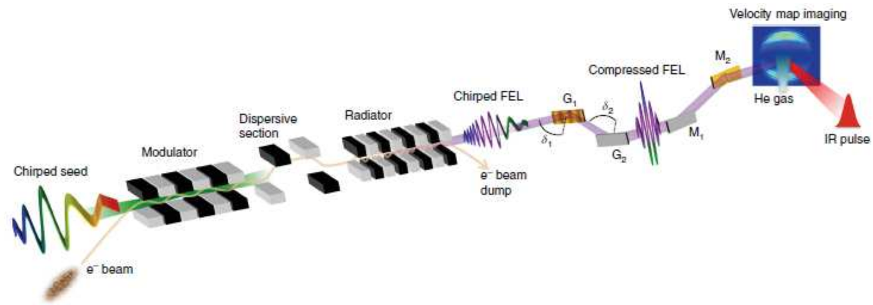

Figure 2.5: A Gaussian laser pulse with a frequency chirp is used to seed the FEL in CPA mode. Electrons are modulated by the seed, and the resulting density modulation is transformed into bunching when passing through the dispersive section. The modulated electrons emit coherently in a long undulator tuned at an harmonic of the seed. The FEL beam is directed towards the experimental chamber, where the FEL pulse duration is measured by photo-ionizing He gas atoms and acquiring a photo-electron distribution using a VMI spectrometer.[36].

The chirped light after amplification is then dechirped by a grating pair, shortening the pulse and increasing the peak power (see Fig. 2.5). This scheme was proposed in FELs by [35]. At FERMI the scheme was implemented and tested for the first time [36] providing a compression of the pulse duration of about a factor 4. While promising in reaching ultrashort duration at short wavelengths, this scheme is prone to phase distortions of the amplified pulse that cannot be easily re-compressed to the ideal values. In addition, optical compressors have a transmission efficiency pretty low at short wavelengths, making not trivial to recover by compression the original peak power prior to compression. Different other schemes rely on the properties of the seed laser to manipulate the FEL photon pulse.

2.2.2 Superradiance

The saturation process in a free-electron laser (FEL) can be exploited to generate ultrashort pulses. As the electrons pass through the field, they are amplified, and the emitted radiation becomes more intense. However, as the intensity of the radiation increases, it can cause the electrons to lose energy, which slows down the amplification process. This phenomenon is known as saturation, and it can be used to generate ultrashort pulses of radiation [11]. In this non-linear regime achievable after saturation, the pulse light slips over the electron bunch faster than it did in the exponential regime. This regime has the unique property of a pulse duration that scales with the inverse squared root of the position along the undulators line. By carefully controlling the electron beam and magnetic field, it is possible to produce pulses as short as a few femtoseconds [14]. This is one of the methods explored at FERMI and it is a central argument of this thesis, an extensive description including the achieved experimental results is provided in Chapter 5.

Chapter 3

Introduction to FEL Theory

It is well known that an accelerated electric charge emits radiation. This is the basic principle on which synchrotrons are built: the trajectory of electrons is bent by magnetic fields, in order to form a circular trajectory. In a circular motion, electrons experience a centripetal acceleration, and emit radiation called synchrotron radiation. In the case of an FEL, the light is emitted by electrons traveling through a series of a small bending magnets, with an alternate sign of the magnetic field [37]. A collection of this small bending magnets form an undulator. In this situation, the electrons will "wiggle" in the undulator, forming an oscillating trajectory. In the following we are going to review the physics behind the FEL emission, for a single electron, which will be extended in the Appendix A.

3.1 Motion in a Magnetic Field

We start from studying the case of a single particle in an oscillating magnetic field of a planar undulator. As we discussed before, the oscillating magnetic field is generated by a collection of permanent magnets, with alternate signs. The strength of the magnetic field is determined by the magnetic material and by the undulator geometry, mainly by the gap between the upper and the lower series of poles. For simplicity we assume that the motion is along the z direction and the oscillations are in the transverse x direction. Using the fact the the curl and the Laplacian are zero in the gap of the undulator, the magnetic field on axis can be expressed as

$$\mathbf{B} = B_0 \sin(k_u z) \quad \text{with} \quad \mathrm{k_u} = \frac{2\pi}{\lambda_\mathrm{u}}, \tag{3.1}$$

where λ_u is the period of the undulator.
In order to describe the dynamics of an electron passing through the magnetic field of an undulator we recover the relativistic equations of motion. From

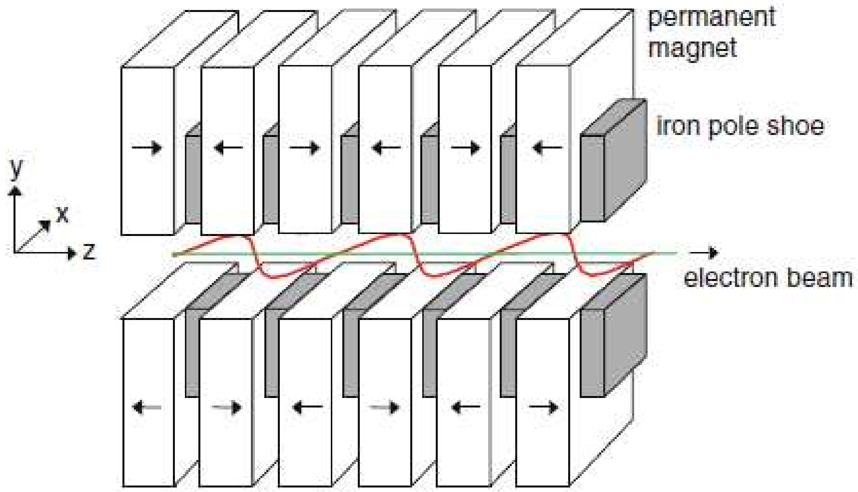

Figure 3.1: Scheme of a generic planar undulator. The permanent magnets generate the magnetic field that impress the oscillator motion to the e-beam. [38]

special relativity, we know that the dynamics of a relativistic particle is given by (assuming gamma as constant)

$$\mathbf{p} \quad = \quad mc\gamma\boldsymbol{\beta}, \tag{3.2}$$

where c is the speed of light in vacuum and m is the mass of the particle, in our case an electron, and where we use definitions of the Lorentz transformation parameters

$$\beta = \frac{v}{c} \quad \text{and} \quad \gamma = \frac{1}{\sqrt{1-\beta^2}}.$$

The force impressed by an electromagnetic field on the particle is

$$\frac{d\mathbf{p}}{dt} = \frac{e_0}{c}\left(\mathbf{v} \times \mathbf{B} + \mathbf{E}\right) = e_0\left(\boldsymbol{\beta} \times \mathbf{B} + \mathbf{E}\right) \tag{3.3}$$

In order to integrate the equation of motion with the field given by Eq. 3.1 and to find the expression of the electron trajectory and velocity, we have to integrate Eq. 3.3. Substituting the expression of the field in Eq. 3.3 we obtain the following system of equations

$$\begin{cases} \beta_x^{'} = \frac{e_0}{mc\gamma} B_y \sin(k_u z)\, \beta_z, \\ \beta_y^{'} = 0, \\ \beta_z^{'} = -\frac{e_0}{mc\gamma} B_y \sin(k_u z)\, \beta_x, \end{cases} \tag{3.4}$$

The first of Eq. 3.4 can be integrated over time finding the expression for the particle transverse velocity

$$\beta_x = \beta_{x0} + \frac{e_0}{mc\gamma} B_y \int\limits_0^t \sin(k_u z)\, \beta_z dt = \beta_{x0} + \frac{e_0}{mc^2\gamma} B_y \int\limits_0^z \sin(k_u z)\, dz =$$

$$= \beta_{x0} - \frac{e_0 B_y}{mc^2\gamma k_u} \left[\cos(k_u z) - 1\right] = -\frac{e_0 B_y}{mc^2\gamma k_u} \cos(k_u z)\,. \tag{3.5}$$

In the second step we have used the fact that $c\beta_z dt = dz$ and defined the integration constant $\beta_{x0} = -e_0 B_y / mc^2\gamma k_u$. This choice for the initial condition for the transverse velocity ensures a purely oscillatory motion in the x-plane. We introduce the undulator strength parameter

$$K = \frac{e_0 B_y}{mc^2 k_u} = \frac{\lambda_u e_0 B_y}{2\pi mc^2} = 0.934 B_0\, [T]\, \lambda_u\, [cm]$$

The magnetic field intensity and the length of the undulator period (that we expressed in Tesla and cm respectively in the practical units expression) are the two physical quantities that can be varied to modify the undulator strength. While the length of the period is a parameter generally fixed once the undulator has been built, the intensity of the magnetic field can be varied by changing the gap of the undulator, i.e. the transverse distance between the poles.
In order to find the relation for β_z, instead of integrating the last relation in Eq. 3.4, we use the fact that we assume the energy of the electron as a constant of motion, and the modulus of the velocity is preserved. This condition will be relaxed when we will deal with the interaction of the electron with the field of a co-propagating electromagnetic wave. In this derivation we assume

$$\beta^2 = 1 - \frac{1}{\gamma^2} = \beta_x^2 + \beta_z^2 = const.$$

Therefore, substituting Eq. 3.5 and manipulating the expression, we end up with

$$\beta_z = 1 - \frac{1}{2\gamma^2} \left(1 + \frac{K^2}{2}\right) - \frac{K^2}{4\gamma^2} \cos(2k_u z)\,. \tag{3.6}$$

This relation shows that the longitudinal motion is composed by an average longitudinal velocity

$$\bar{\beta}_z = 1 - 1/\left(2\gamma^2\right)\left(1 + K^2/2\right), \tag{3.7}$$

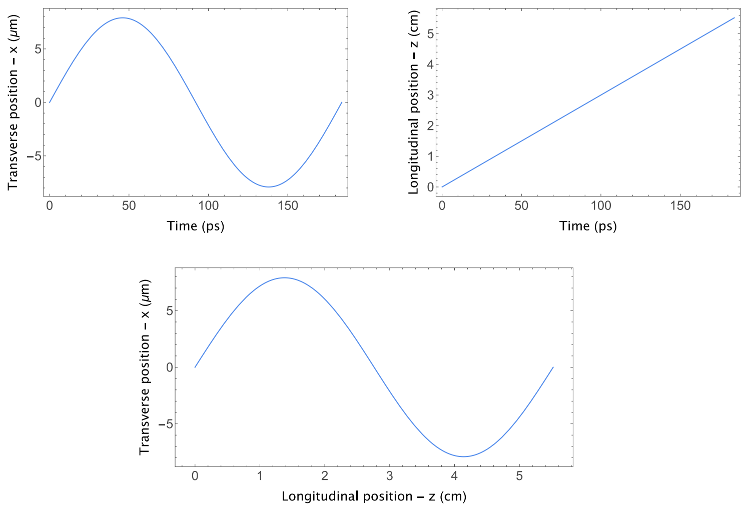

Figure 3.2: Plots of the trajectories in Eqs. 3.8 and 3.9. While the transverse component oscillate around the center of the z axis, the longitudinal is a linear function in time, therefore the oscillating term doesn't contribute to the motion. This is because of the term γ^2in the denominator, which is of the order of 10^6. Here we have used $c = 3 \cdot 10^8$, $\beta_z = 0.999999$, $\gamma = 2000$, $K = 1.8$, $\lambda_u = 0.0552cm$ and the time correspond to a single wiggler period. .

and a term oscillating with twice the frequency of the transverse motion induced by the magnetic field, Eq. 3.5. The oscillation has an amplitude proportional to $(K/\gamma)^2$. In order to calculate the electron trajectory in the case of an ultra-relativistic beam where $\gamma >> K$, we neglect the longitudinal oscillatory motion and integrate once more over time, to obtain the equation of motion in the undulator

$$x\left(t\right) = -\frac{cK}{\gamma}\int_0^t \cos\left(k_u\bar{\beta}_z ct\right) dt = \frac{K}{\gamma k_u}\sin\left(k_u ct\right). \tag{3.8}$$

As expected the transverse trajectory is oscillating around the z axis. For the longitudinal component, we have

$$z\left(t\right) = c\int_0^t \left[\bar{\beta}_z - \frac{K^2}{4\gamma^2}\cos\left(2k_u z\right)\right] dt = \bar{\beta}_z ct - \frac{K^2}{8\gamma^2 k_u}\sin\left(2k_u ct\right) \tag{3.9}$$

A charged particle that experiences acceleration emits light. From the third plot of Fig. 3.2, it is clear that the electron experiences an acceleration in the x direction. This configuration, as we will see later, will produce photons with linear horizontal polarization. In case of an oscillatory motion in the y-z plane instead of the x-z plane, the light would be polarized in the vertical plane.

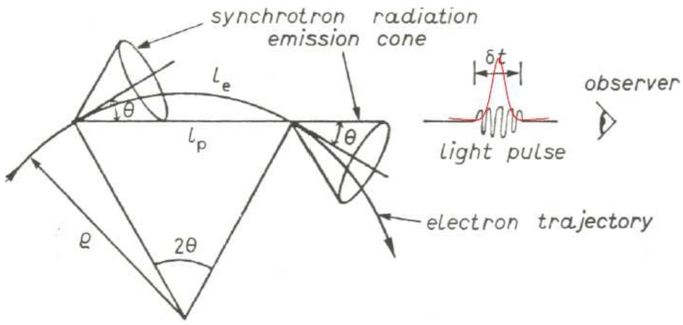

Figure 3.3: Sketch of the trajectory of one electron and the light pulse emitted during the acceleration.

Superimposing these two motions with half a period of phase mismatch, would generate an helical motion along the z axis and the light would be be circularly polarized.
The duration of the light pulse depends on the different propagation velocity of electrons wiggling along the undulator and the light propagating along the axis. We define the time that the photons take to travel through the undulator as δt_p and the correspondent time of propagation of the the electrons as δt_e (see Fig. 3.3 for a simple representation). These two quantities are given by

$$\delta t_p = \frac{L_u}{c} \quad \text{and} \quad \delta t_e = \frac{L_u}{v_z} = \frac{L_u}{c\left[1 - \frac{1}{2\gamma^2}\left(1 + \frac{K^2}{2}\right)\right]},$$

where $L_u = N\lambda_u$ is the length of the undulator and where we have considered the averaged longitudinal velocity Eq. 3.7. The slippage between light and electrons is the difference

$$\delta t_e - \delta t_p = \frac{L_u}{c\beta_z}\left[1 - \frac{1}{2\gamma^2}\left(1 + \frac{K^2}{2}\right) - 1\right] = \frac{N\lambda_u}{2\gamma^2 c}\left(1 + \frac{K^2}{2}\right),$$

corresponding to the duration of a pulse composed by N cycles, each of wavelength

$$\lambda_0 = \frac{\lambda_u}{2\gamma^2}\left(1 + \frac{K^2}{2}\right). \tag{3.10}$$

The wavelength of the light emitted by the electron depends on the period of the undulator, the energy of the electron and the undulator strength parameter. Assuming a given value for the period λ_u, which usually is set once the undulator has been built, by changing the energy of the electron and the gaps of the undulator, i.e. the Kparameter, we can tune the final wavelength covering an extremely wide spectral range: several orders of magnitudes from terahertz to hard-X ray and $\gamma-$ray wavelengths.

Synchrotron radiation is emitted in a cone of aperture $1/\gamma$ with respect to the direction of motion. The electron is following a curved trajectory; by considering the ratio between the transverse velocity and the longitudinal velocity the deflection angle is

$$\theta \simeq \frac{\beta_x}{\beta_z} \sim \frac{K}{\gamma} \tag{3.11}$$

where we have expanded the *arctan* of the angle because for an ultrarelativistic beam $\gamma >> 1$. The field generated by the electron in motion is given by
From Liènard-Wiechert theory of potentials [39], the electric field generated by the charge is

$$\mathbf{E}(\mathbf{R},t) = e_0 \frac{\mathbf{n}-\boldsymbol{\beta}}{\gamma^2 (1-\boldsymbol{\beta}\cdot\mathbf{n})^3 |\mathbf{r}'|^2} + \frac{e_0}{c} \frac{\mathbf{n}\times\left[(\mathbf{n}-\boldsymbol{\beta})\times\boldsymbol{\beta}'\right]}{(1-\boldsymbol{\beta}\cdot\mathbf{n})^3 |\mathbf{r}'|}\Bigg|_{t_r}, \tag{3.12}$$

where $\mathbf{n} = \mathbf{r}'/|\mathbf{r}'|$and the prime indicates the time derivative. The expression of the electric field is evaluated at the retarded time $t_r = t - r'(t)/c$, since the fields propagate at c in vacuum. As we can see, the electric field that comes from the Liènard-Wiechert potentials is made by two terms: the first one is proportional to the inverse of γ^2 and decays as the square of the distance. If velocity and acceleration are zero, only this term survives which corresponds to the electrostatic electric field generated by a charge. The first term is usually referred to as a generalized Coulomb field. The second term is proportional to the particle acceleration and decays as the inverse first power of the distance, therefore it is dominant one at large distances.
Spectral brightness is the measure of the amount of light that is emitted by a source per unit frequency and per unit of solid angle [39]

$$\frac{dI(\omega)}{d\omega d\Omega} = \frac{c}{4\pi^2}\left|\int_{-\infty}^{+\infty} e^{i\omega t}\left[\mathbf{r}'(t)\,\mathbf{E}(\mathbf{R},t)\right]_{t_r}\right|^2 dt. \tag{3.13}$$

Now we substitute in Eq. 3.13 the electric field proportional to β' in Eq. 3.12,

$$\frac{dI(\omega)}{d\omega d\Omega} = \frac{e_0^2}{4\pi^2 c}\left|\int_{-\infty}^{+\infty} e^{i\omega t}\left[\frac{\mathbf{n}\times\left[(\mathbf{n}-\boldsymbol{\beta})\times\boldsymbol{\beta}'\right]}{(1-\boldsymbol{\beta}\cdot\mathbf{n})^3}\right]_{t_r} dt\right|^2.$$

In order to evaluate this expression, we change variable and integrate over the retarded time

$$t_r = t - \frac{\mathbf{n}\cdot\mathbf{r}'(t)}{c} \Rightarrow dt_r = dt - \mathbf{n}\cdot\boldsymbol{\beta}dt,$$

$$\frac{dI(\omega)}{d\omega d\Omega} = \frac{e_0^2}{4\pi^2 c}\left|\int_{-\infty}^{+\infty} e^{i\omega\left(t_r - \frac{\mathbf{n}\cdot\mathbf{r}'(t_r)}{c}\right)} \frac{\mathbf{n}\times\left[(\mathbf{n}-\boldsymbol{\beta})\times\boldsymbol{\beta}'\right]}{(1-\boldsymbol{\beta}\cdot\mathbf{n})^2} dt_r\right|^2. \tag{3.14}$$

This expression is further simplified by noting that

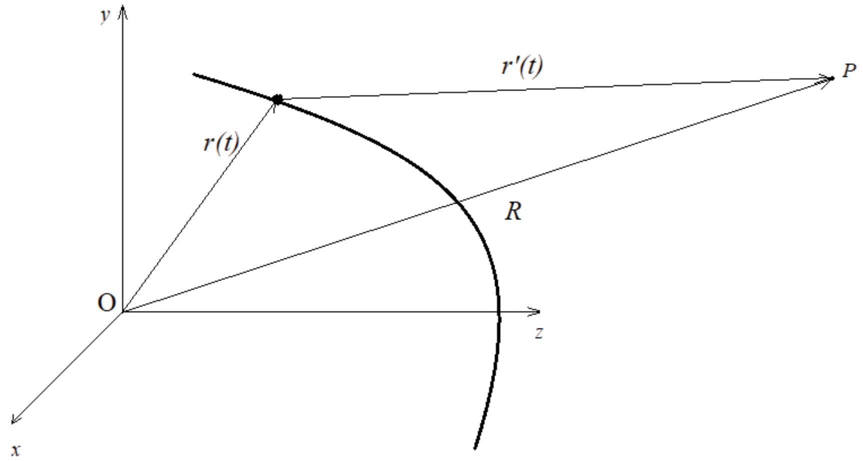

Figure 3.4: System of coordinates for the description of the energy emission from a particle. The point P correspond to a static observer.

$$\frac{\mathbf{n}\times\left[(\mathbf{n}-\boldsymbol{\beta})\times\boldsymbol{\beta}'\right]}{(1-\boldsymbol{\beta}\cdot\mathbf{n})^2}=\frac{d}{dt}\frac{\mathbf{n}\times(\mathbf{n}\times\boldsymbol{\beta})}{(1-\boldsymbol{\beta}\cdot\mathbf{n})}=\frac{d}{dt_r}\mathbf{n}\times(\mathbf{n}\times\boldsymbol{\beta}),$$

Therefore we have

$$\frac{dI(\omega)}{d\omega d\Omega}=\frac{e_0^2}{4\pi^2 c}\left|\int_{-\infty}^{+\infty}e^{i\omega\left(t_r-\frac{\mathbf{n}\cdot\mathbf{r}'(t_r)}{c}\right)}\frac{d}{dt_r}\left[\mathbf{n}\times(\mathbf{n}\times\boldsymbol{\beta})\right]dt_r\right|^2.$$

Integrating by parts by parts one gets

$$\frac{dI(\omega)}{d\omega d\Omega}=\frac{e_0\omega^2}{4\pi^2 c}\left|\int_{-\infty}^{+\infty}e^{i\omega\left(t_r-\frac{\mathbf{n}\cdot\mathbf{r}'(t_r)}{c}\right)}\mathbf{n}\times(\mathbf{n}\times\boldsymbol{\beta})\,dt_r\right|^2.$$

We now consider a generic charged particle following the trajectory Eq.3.8, 3.9, and we define the system of reference shown in Fig. 3.4.
For an electron moving along the z axis with an oscillation in the x axis, we have (in the limit of a far field, as we will explain later in this chapter)

$$\mathbf{n}=\begin{pmatrix}0\\0\\1\end{pmatrix}\quad\text{and}\quad\boldsymbol{\beta}=\begin{pmatrix}\beta_x\\0\\\beta_z\end{pmatrix}.$$

This leads to

$$\mathbf{n}\times(\mathbf{n}\times\boldsymbol{\beta})=\begin{pmatrix}-\beta_x\\0\\0\end{pmatrix}.$$

The emission process occurs in a finite interval of time where acceleration is different from zero. Therefore, we can assume that in times before entering the undulator and after the exit from it, there is no emission: this allows us to restrict the integration between $t_{in} = 0$, for simplicity, and $t_{fin} = L_u/v_z$. In order to specify the time retarded condition, we assume that the observer is at a large distance from the source so that $\mathbf{n}$ is purely longitudinal. Using Eq. 3.9 we have

$$t_r - \frac{\mathbf{n} \cdot \mathbf{r}'(t_r)}{c} = t_r - \bar{\beta}_z t_r + \frac{K^2}{8\gamma^2 k_u c} \sin(2k_u c t_r),$$

so our integral becomes

$$\frac{dI(\omega)}{d\omega d\Omega} = \frac{e_0 \omega^2}{4\pi^2 c} \left| \int_0^{L_u/c} e^{i\omega\left[\left(1-\bar{\beta}_z\right)t_r + \frac{K^2}{8\gamma^2 k_u c}\sin(2k_u c t_r)\right]} \frac{K}{\gamma} \cos(k_u c t_r)\, dt_r \right|^2,$$

where we have substituted the expression for β_x. Using the Jacobi–Anger expansion we can write

$$e^{i\chi \sin(\psi)} = \sum_{m=-\infty}^{+\infty} e^{im\psi} J_m(\chi),$$

where $J_m(\chi)$ is n-th Bessel function of the first kind. In our case the quantities χ, ψ, ω_u are defined as

$$\chi = \frac{K^2}{8\gamma^2} \frac{\omega}{\omega_u} \quad \psi = 2\omega_u t_r \quad \omega_u = k_u c.$$

After the substitution we observe that the term χ doesn't depend on t_r. The sum and the Bessel functions can be carried out of the integral

$$\frac{dI(\omega)}{d\omega d\Omega} = \frac{e_0 \omega^2}{4\pi^2 c} \frac{K^2}{\gamma^2} \left| \sum_{m=-\infty}^{+\infty} J_m(\chi) \int_0^{L_u/c} e^{it_r\left[\left(1-\bar{\beta}_z\right)\omega + 2m\omega_u\right]} \cos(\omega_u t_r)\, dt_r \right|^2.$$

Using the exponential representation of the cosine, we have only one exponential We have therefore

$$\frac{dI(\omega)}{d\omega d\Omega} = \frac{e_0 \omega^2}{4\pi^2 c} \frac{K^2}{\gamma^2} \left| \sum_{m=-\infty}^{+\infty} J_m(\chi) \int_0^{L_u/c} e^{it_r\left[\left(1-\bar{\beta}_z\right)\omega + 2m\omega_u\right]} \frac{e^{i\omega_u t_r} + e^{-i\omega_u t_r}}{2} dt_r \right|^2 =$$

$$= \frac{e_0 \omega^2}{16\pi^2 c} \frac{K^2}{\gamma^2} \left| \sum_{m=-\infty}^{+\infty} J_m(\chi) \int_0^{L_u/c} \left[e^{it_r\left[\left(1-\bar{\beta}_z\right)\omega + (2m+1)\omega_u\right]} + e^{it_r\left[\left(1-\bar{\beta}\right)\omega + (2m-1)\omega_u\right]} \right] dt_r \right|^2.$$

The exponentials differ for the term $2m \pm 1$. By defining $2m \pm 1 = u$ with u odd, we can transfer this difference into the order of the Bessel function and then sum up the two exponentials

$$\frac{dI(\omega)}{d\omega d\Omega} = \frac{e_0\omega^2}{16\pi^2 c}\frac{K^2}{\gamma^2}\left|\sum_{u=-\infty}^{+\infty}\left[J_{\frac{u+1}{2}}(\chi) + J_{\frac{u-1}{2}}(\chi)\right]\int_0^{L_u/c} e^{it_r\left[\left(1-\bar{\beta}\right)\omega + u\omega_u\right]}dt_r\right|^2 .$$

The integral of the exponential is

$$\int_0^{L_u/c} e^{it_r\left[\left(1-\bar{\beta}\right)\omega+u\omega_u\right]}dt_r = \frac{e^{i\frac{L_u}{c}\left[\left(1-\bar{\beta}_z\right)\omega+u\omega_u\right]}-1}{i\frac{L_u}{c}\left[\left(1-\bar{\beta}_z\right)\omega+u\omega_u\right]} =$$
$$= ie^{i\frac{L_u}{2c}\left[\left(1-\bar{\beta}\right)\omega+u\omega_u\right]}\mathrm{sinc}\left(\frac{L_u}{2c}\left[\left(1-\bar{\beta}_z\right)\omega+u\omega_u\right]\right).$$

where the function *sinc* is defined as $(\sin x)/x$ and has the maximum in the limit $x \to 0$. We simplify the argument considering the expression of $\bar{\beta}_z$, we have

$$\frac{L_u}{2c}\left[\left(1-\bar{\beta}_z\right)\omega+u\omega_u\right] = \frac{L_u}{2c}\left[\frac{\omega}{2\gamma^2}\left(1+\frac{K^2}{2}\right)+u\omega_u\right] =$$

$$\frac{N\lambda_u\omega_u}{2c}\left[\frac{\omega}{2\gamma^2\omega_u}\left(1+\frac{K^2}{2}\right)+u\right] = N\pi\left(\frac{\omega}{\omega_0}+u\right) \quad \text{with} \quad \omega_0 = \frac{2\gamma^2\omega_u}{\left(1+\frac{K^2}{2}\right)}. \tag{3.15}$$

As a final step, we remove the phase factor in the modulus and we limit the sum to positive frequencies, occurring at negative values of the index u. ,We introduce $n = -u$ and using the fact that $J_{-n}(\chi) = (-1)^n J_n(\chi)$, we get

$$\frac{dI(\omega)}{d\omega d\Omega} = \frac{e_0\omega^2}{16\pi^2 c}\frac{K^2}{\gamma^2}\left|\sum_{n=1}^{+\infty}\left[J_{\frac{n-1}{2}}(\chi) - J_{\frac{n+1}{2}}(\chi)\right]\mathrm{sinc}\left[nN\pi\left(\frac{\omega-n\omega_0}{n\omega_0}\right)\right]\right|^2 . \tag{3.16}$$

This is the spectral brightness of the radiation emitted by a single electron traveling through a planar undulator. This relation can be generalized introducing an additional electromagnetic field (coming from an external source or a previous emission), as we reported in Appendix A. In Fig. 3.5, left plot, it is shown the behavior of the *sinc* function for different values of number of undulator periods N. The *sinc* function is maximized when its argument is zero. This indeed allowed us to limit the sum to positive n for positive frequencies. The sum over n in Eq.3.16 implies the presence of a sequence of higher order, odd harmonics of the fundamental, centered at ω_0. The process described in this section corresponds to the emission of light from a single charge traversing an undulator magnet. The electron produce a field impulse composed by a number

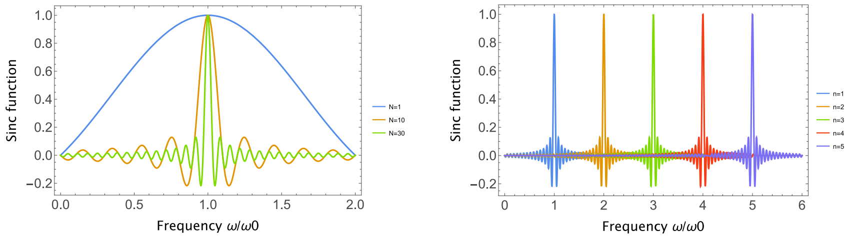

Figure 3.5: Left: Plot of the *sinc* function in Eq.3.14, for some values of the number of the undulator's periods N. Right: Plot of the *sinc* function for different harmonic number n with 30 periods.

of periods equal to the number of wiggles of the electron trajectory, and period length given by the resonance condition, Eq. 3.10. The spectrum is composed by a sequence of odd harmonics of the central wavelength Eq. 3.10. The relative spectral width of each harmonic is inversely proportional to the number of periods of the undulator, corresponding to the fact that a longer train or radiation periods leads to a narrower spectral linewidth. The emission of an ensemble of electrons will be characterized by a field that is the superposition of the field emitted by each particle. The properties of the field of this ensemble of particles depends therefore on the synchronization between the trajectories of these particles, and the electron dynamics in presence of a collection of electrons can be dominated by collective effects that alter the electron dynamics itself. This process will be analyzed in the next section.

3.2 FEL Amplifier

In the previous section we analyzed the dynamics of an electron traversing an undulator. The electron dynamics in presence of both the fields of the undulator and of an optical wave of wavelength close to the resonant wavelength Eq. 3.10 is governed by the pendulum equation [40]

$$\begin{cases} \frac{d\theta(t)}{dt} = n\omega_u \left(\frac{n\omega_0 - \omega_r}{n\omega_0}\right), \\ \frac{d\nu(t)}{dt} = a\left(\mathbf{r}, t\right)\cos\left[\theta\left(t\right) + \Phi\left(\mathbf{r}, t\right)\right], \end{cases} \tag{3.17}$$

where n is the harmonic number, ω_u ω_0 ω_r are, respectively, the undulator, resonance and radiation frequency, $a\left(\mathbf{r}, t\right)$ is the slowly varying amplitude of the radiation field and $\Phi\left(\mathbf{r}, t\right)$ is an arbitrary slowly varying phase of the radiation field, that is in general expressed as

$$E(\mathbf{r}, t) = a\left(\mathbf{r}, t\right) e^{i(k_r z - \omega_r t + \Phi(\mathbf{r}, t))}. \tag{3.18}$$

The variable

$$\theta\left(t\right) = \left(nk_u + k_r\right) z\left(t\right) - \omega_r t \tag{3.19}$$

represents the ponderomotive phase of the electron in the longitudinal phase space and the variable

$$\nu = n\omega_u \left(\frac{n\omega_0 - \omega_r}{n\omega_0} \right) \tag{3.20}$$

represents the electron energy detuning with respect to an ideal electron that has the resonance Eq. 3.10 at the wavelength of the optical wave and is proportional to the electron energy. These equations are derived from the Lorentz force equation Eq.3.3 averaging the fast oscillating terms due to the fast oscillations of the electromagnetic fields and of the undulator field observed by the ultra-relativistic electron. From the definition Eq. 3.17 we have that when the optical wave is close to the resonant frequency $\omega_r \simeq \omega_0$, we have that $d\theta/dt = \nu \simeq 0$ i.e. the ponderomotive phase θ represents a slowly varying variable indicating the electron phase with respect to the field. From the second of Eq.3.17 we have that the electron energy variation depends on the phase of the field. A bunch of electrons interacting with a radiation beam with a wavelength close to the resonant wavelength, is therefore periodically modulated in energy, with the period of the optical wave. The energy modulation will cause a periodic detuning of the electrons that according to the first of Eq.3.17 will shift forward ($d\theta/dt > 0$) or backward ($d\theta/dt < 0$) in phase depending on the energy modulation. This mechanism converts the energy modulation into a density modulation of the electron beam. The electrons with the same longitudinal coordinate emit radiation in phase causing an amplification of the field.
The variation of the radiation field is strictly related to the phase of the electrons

$$\frac{\partial}{\partial \tau} a(\tau) = -2\pi g_0 \frac{1}{N_e} \sum_{i=1}^{N_e} e^{-\imath\theta_i(\tau)}, \tag{3.21}$$

where g_0 is the gain coefficient [41] and the average term in RHS is referred as the bunching factor, which will be derived in the case of the seeded FEL, in Chapter 4. This term is related to the density modulation via the Fourier transform, in fact the density function (in the 1D limit) is

$$\rho(\tau) = \sum_{i=1}^{N_e} \delta(\tau - \tau_i),$$

and taking the Fourier transform we have

$$\widetilde{\rho}(\omega) = \int_{-\infty}^{+\infty} e^{\imath\omega\tau} \sum_{i=1}^{N_e} \delta(\tau - \tau_i)\, d\tau = \sum_{i=1}^{N_e} e^{\imath\omega\tau_i}.$$

$$|\widetilde{\rho}(\omega)|^2 = \sum_{i=1}^{N_e} e^{\imath\omega\tau_i} \sum_{j=1}^{N_e} e^{-\imath\omega\tau_j} = N_e + \sum_{i\neq j}^{N_e} e^{\imath\omega(\tau_i - \tau_j)}$$

This is important because, from this relation, we can see the contribution of this term to the radiation field. If the electrons are randomly distributed (as in the case of the SASE) the second term in the square brackets is zero, on average. In the case of correlated electrons (as in the case of a seeded FELs), term in the square brackets gives N_e^2. Therefore, seeding an electron beam provides a stronger emission of photons.

This amplification of the radiation field is the result of the positive feedback between two physical processes: the growth of the modulation induced by the interaction of the beam with the undulator field and the co-propagating laser wave and the emission of radiation from a this modulated electron beam. These processes, in a long undulator, lead to an exponential growth of the power (in the 1D theory [42, 43, 44])

$$P\left(z\right) \propto \frac{P_0}{9} e^{z/L_g} \quad \text{with} \quad L_g = \frac{\lambda_u}{4\pi\sqrt{3}\rho_{FEL}}.$$

where z is the position inside the undulator, λ_u is the undulator period, P_0 is the initial power (which could come from shotnoise, in the case of a SASE FELs, or from an external source, in the case of seeded FELs) and

$$\rho_{FEL} = \frac{1}{4\pi}\left[\frac{2\pi^2}{\gamma^3}\left(\frac{I_{peak}}{I_a \Sigma_e}\right)\left(\lambda_u K\left[JJ\right]\right)^2\right]^{1/3}, \tag{3.22}$$

is the Pierce parameter, a very fundamental quantity that affect all the variables in the FEL dynamics. Here, $[JJ] = J_0\left(\chi\right) - J_1\left(\chi\right)$ is the Bessel coupling [40], Σ_e is the traversal surface of the e-beam, I_a is the Alfven current and I_{peak} is the bunch current and. We have introduced here the gain length L_g representing the undulator length required to increase the radiation power by e Saturation in a FEL amplifier starting from a randomly distributed electron beam, where radiation emission is governed by the electron shot-noise (Self-Amplified Spontaneous Emission FEL, i.e. SASE FEL), is typically reached in $18-20$ times L_g . The FEL amplification can be speed up by preparing the beam with a modulation induced before the injection in the amplifier, as it happens at FERMI, a seeded FEL. In this case the saturation length is shorter. For the FERMI facility, we said that usual values for λ_u is a couple of centimeters, ρ_{FEL} is usually some 10^{-3}, therefore the gain length is $\sim 1m$. In Fig. 3.6 is reported a simulation of the energy growth along the second stage of FEL2 that reproduce the exponential evolution of the energy in the FEL pulse (linear plot on the left and log plot in the right).

So far we have introduced the high-gain case for the FEL dynamics in what is called *cold beam limit, i.e.* the limit in which just the longitudinal evolution is considered. In a more generic case, the transverse quantities affect negatively the light emission. Just consider the case in which the beam is no more mono-energetic but has some energy spread with the mean value centered at the resonance energy. It is clear that only the electrons at the resonance energy will emit at the resonance wavelength. The others have the effects of broadening the spectrum, which is a degradation effects for FEL quality. The transverse interactions cause similar worsening effects for the quality. In order to keep

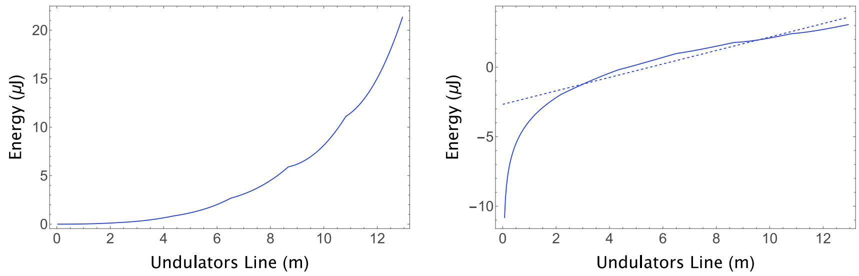

Figure 3.6: Left: Energy growth from a simulation with GENESIS1.3 [45] along the FERMI FEL2 line. Here we have the energy emitted from a bunch at $\gamma_0 = 1.3$GeV,along six undulators with $\lambda_u = 3.48$cm and $N = 66$ periods. Here is visible the exponential growth of the light field. Right: The same as in the left panel, but in logarithmic scale for the energy. This is useful in order to fit linearly the growth (dashed line) and obtain the gain length of the process, which in this case is of 1.8m.

trace of these degradating effects, without rework the whole path that led to the FEL equation, one can use the Xie relations.
The main results that Xie [46] obtained by studying the effects of the transverse and other degradating parameter are the following: first, the gain length and the output power of the light will be modified as

$$L_{gc} = \frac{L_g}{\chi} \quad \text{and} \quad P_{oc} = \chi^2 P_o,$$

where the c stands for corrected and P_o is the output power. The quantity χ is a function of several parameters that keep into account the degradating effects. Xie proposed these relations

$$\eta_d = \frac{L_g}{L_r}, \qquad \eta_\epsilon = \frac{4\pi\epsilon L_g}{\beta_T \lambda_0}, \qquad \eta_\gamma = \frac{4\pi\sigma_\gamma L_g}{\lambda_u \gamma},$$

in which, the first relation takes into account the natural diffraction of the radiation field, which sets a lower limit to the transverse size of the optical mode. The quantity $L_r = 4\pi\sigma_x^2/\lambda_0$ is the Rayleigh range of the radiation beam with wavelength $\lambda_0$and σ_x is the r.m.s. of the beam. The second relation is associated to the presence of transverse effects, in which ϵ is the beam transverse emittance and $\beta_T$is the transverse beta Twiss coefficient. The last relation describes the effects in presence of an energy spread in the e-beam, $\sigma_\gamma$is, in fact, the r.m.s. energy spread. From these relations, the parameter χ is given by

$$\chi\left(\eta_d, \eta_\epsilon, \eta_\gamma\right) = \left(1 + \sum_n a_n \eta_d^{\alpha_n} \eta_\epsilon^{\beta_n} \eta_\gamma^{\delta_n}\right)^{-1}.$$

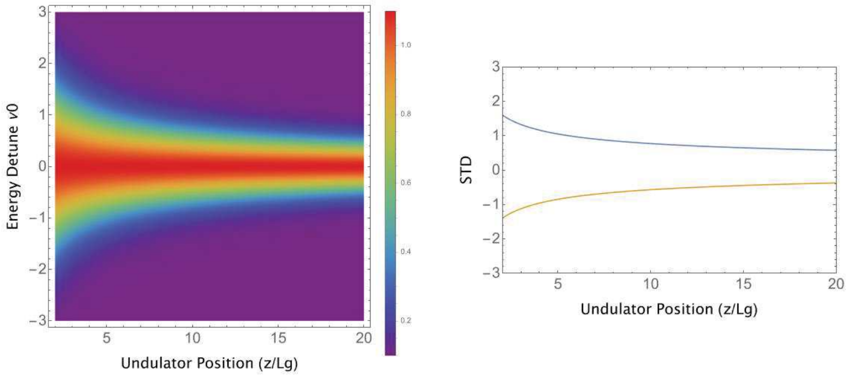

Figure 3.7: Plots of the gain function and its rms as a function of the energy detune and the position inside the undulator.

While the Xie relations can be evaluated analytically, the coefficients a_n and the powers of the η_i were evaluated numerically and tabulated. As final concept, we want to introduce the gain function, defined as

$$g\left(\nu_0, z\right) = \frac{\left|a\left(\nu_0, z\right)\right|^2}{\left|a\left(\nu_0, 0\right)\right|^2} - 1.$$

where $a\left(\nu_0, z\right)$ is the field amplitude of the emitted radiation, ν_0 is the energy detune and z is the position along the undulator. Assuming $\nu_0 = 0$, *i.e.* the maximum growth, we can the gain function can be written as

$$g\left(\nu_0, z\right) = \exp\left[\frac{z}{L_g} - \frac{1}{\sigma^2_{\Delta\omega/\omega}}\left(\frac{\omega_0 - \omega_r}{\omega_0}\right)^2\right].$$

where

$$\sigma_{\Delta\omega/\omega} = 2\rho_{fel}\sigma_\nu = \frac{6\rho_{fel}}{\sqrt{2z/L_g}}.$$

As we can see, not only the gain function increases exponential along the undulators line, but also has its bandwidth decreasing as the inverse of the square root, as reported in Fig. 3.7. At the end of process, when $z/L_g \sim 18 - 20$, the bandwidth is almost equal to the Pierce parameter, stressing the fact that has a fundamental role in the FEL process.

Up to now we have discussed the high-gain theory of FELs and we saw that the emission of energy from the e-beam can be exponential, but this process cannot last forever. At some point the energy of the electrons lower such that the resonance condition is no longer valid. At this point we have saturation. In the saturation regime, the FEL behaves like a small-gain process. Without an external seed, the amplification process starts from shotnoise. The amplification,

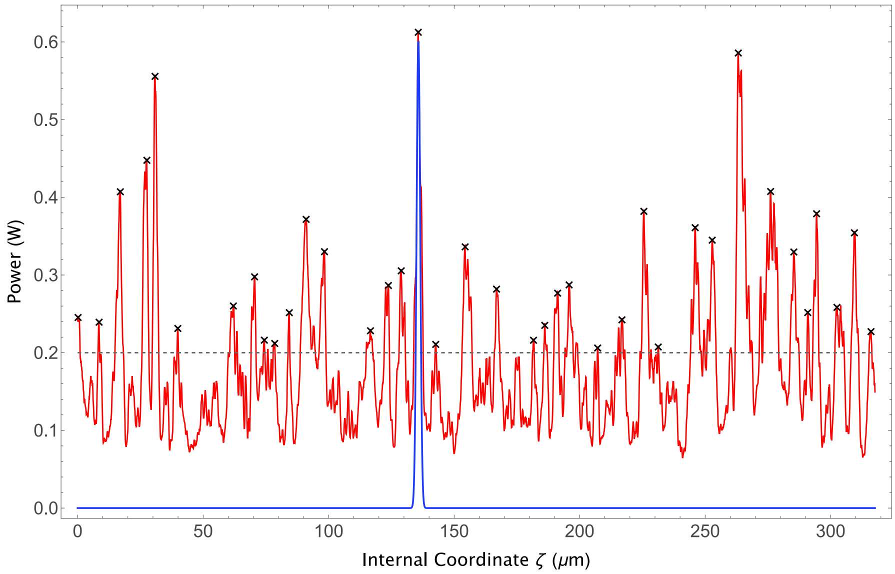

Figure 3.8: Example of power profile of a simulated SASE FEL at 14.67nm (red line). In blue is reported an example of single spike fit.

therefore, will produce a power profile that is an amplification of the shotnoise. In Fig. 3.8 is reported an example of a simulation of the power profile, at the end of the amplification process, at 14.67nm. This high-power, multi-spike structure is a characteristic of the power profile in a SASE FEL. It is complicate to estimate the time structure of these kind of profiles, in an analytical way, due to local fluctuations of the e-beam parameters, such as energy, energy spread, current, and so on. Despite this, [47] provide a statistical analysis of the time structure.

From the first order time correlations of the electrical field of the radiation, it is possible to obtain the rms coherence time of the single spike as

$$\tau_{coh} = \frac{\sqrt{\pi}}{\sigma_\omega}. \tag{3.23}$$

In this relation appears the standard deviation of the gain process σ_ω defined before. This relation is true only for the linear regime, therefore from the start-up to the exponential regime. The blue fit in Fig. 3.8 is an example of the structure of a single spike. The analysis of the peaks considered within a threshold of the 30% of the peak power gave us a result of $\delta t = 7.85 \pm 2.46$fs. This result is the mean of all the spike selected (marked with a cross). During the evolution, we saw that $\sigma_{\Delta\omega/\omega}$ decreases, indicates that the time structure of the single spike start at lower value and then increases until the end of the amplification. Since at the end of the exponential regime we saw that

$\sigma_{\Delta\omega/\omega} \sim \rho_{fel}$, we can conclude that the temporal structure can be estimate, at the end of the amplification process as $\tau_{coh} \sim (\rho_{fel} \cdot \omega)^{-1}$[48]. Finally, from a statistical point of view, we can estimate also the number of the spikes simply by consider the whole time window divided by the mean coherence time, $N_{spike} = T_{window}/\tau_{coh}$. In the figure above, we have considered only the main spikes but if we consider all of them, we obtain a mean number of 159 spikes. Since the time window is $\sim$ 1.2ps, the formula gives us N_{spike}=152, very close to the real number. One can measures the coherence time with an interferometric approach, and obtains the number of modes N_{spike} from a statistical analysis of the pulse energy distribution. From this, one can arrive at an estimate for the pulse duration [49]. As a final remarks, we want to briefly describe the effect of a chirped light. Suppose a laser field with a quadratic chirp phase and model it as

$$E(t) = A(t)\, e^{\imath\left(\omega_0 t + \alpha t^2\right)},$$

where α is the quadratic phase chirp (or linear in frequency) and $A(t)$ is the field amplitude. For a Gaussian pulse, we know that the Fourier Transform Limit condition has to hold, therefore $\sigma_t \sigma_\omega = 1/2$. This is true, if the light has no chirp, otherwise we have to take the Fourier transform of the electric field and, knowing the pulse duration σ_t,we can obtain the frequency bandwidth, modified by the presence of the chirp. So, putting in formulas we have

$$\int \left[e^{-\frac{t^2}{4\sigma_t^2}} e^{-\imath\left(\omega_0 t - \alpha t^2\right)} \right] e^{-\imath\omega t} dt = \sqrt{2\pi} C e^{-\frac{(\omega-\omega_0)^2}{4\left[\frac{1+\left(4\alpha\sigma_t^2\right)^2}{4\sigma_t^2}\right]}\left(1+4\imath\alpha\sigma_t^2\right)},$$

which is a bit complicated but, since the Fourier transformation of a Gaussian is a Gaussian, we can recover the frequency bandwidth by the definition of the Gaussian. Therefore, looking at the relation above, we can conclude that

$$\sigma_\omega^2 = \frac{1 + \left(4\alpha\sigma_t^2\right)^2}{4\sigma_t^2},$$

from which, if $\alpha = 0$, then we recover the FTL condition. This told us that the frequency bandwidth is enlarged by the presence of the chirp term and, from the frequency we can obtain

$$\frac{\sigma_\omega}{\omega} = \frac{\sigma_\lambda}{\lambda} \quad \Rightarrow \quad \sigma_\omega = \frac{2\pi c \sigma_\lambda}{\lambda^2}. \tag{3.24}$$

We can identify every single spike in a SASE power profile, as a single Gaussian peak with a pulse duration as described before, and a minimum duration given by the FTL condition. Using the relations above, we can make some examples of pulse durations: consider a 20nm FEL with a relative wavelength $\sigma_\lambda/\lambda = 10^{-3}$, the FTL pulse duration is, therefore, 5.3 fs rms or 12.5 fs FWHM but the coherent time provided by the gain function, Eq. 3.23, gives us 18.81 fs rms or 44.3 fs FWHM. This imply that, in order to shortening the pulse duration, also the gain function has to be modified in some ways. In the next chapter we are going to describe the seeded FELs and the coherent temporal structure in presence of an external seed.

Chapter 4

High Gain Harmonic Generation

In the previous section, we briefly discussed the principles of FEL dynamics, describing the main process causing the energy conversion from the electrons kinetic energy into light. The resonant interaction between the transverse motion of the wiggling electrons, the undulator magnetic field, and the emitted transverse electromagnetic field lead to an instability that converts the electron kinetic energy into the electromagnetic radiation. This energy conversion process is initiated by the presence of a modulation of the electron beam density, or by an input signal that seeds this modulation. The initial modulation can be stochastic, reflecting the arrival time of randomly distributed electrons at the entrance of the undulator, or may be the result of an existing per-modulation that can be induced at the electron emission from the cathode, exploiting the beam dynamics in the accelerator, or in a separated FEL just devoted to prepare the beam modulation. In this chapter we describe a specific FEL configuration where the beam modulation is prepared in a dedicated undulator where the electron beam interacts with an external laser beam, that we will seed the modulation. This configuration was introduced in [50] and extended later in several other variants [51, 52, 53].
A sketch of a high-gain harmonic generation FEL in shown in Fig. 4.1. The first element along the electron beamline is the modulator, a first undulator where the

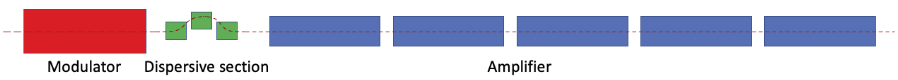

Figure 4.1: Sketch of the setup for an HGHG scheme (see text for details).

electron beam propagates with a laser beam tuned at the resonant wavelength of this undulator. Here the beam is modulated in energy. This energy modulation is then converted into density modulation due to a dispersive section, usually made by four dipoles (see Fig. 4.2). Then the bunch enters an undulators line, in which these undulators are tuned at a specific harmonic of the seed laser, and the amplification process is carried on, until saturation occurs. In the following we are going to enter into details of this scheme.
Seeding the amplifier with an external laser source, provides a number of advantages, as increased stability in pulse and photon energy, reduced size of the device, improved longitudinal coherence and more control on the pulse structure. Further, we also saw that the initial bunching factor plays a crucial role in the FEL process and higher is the bunching factor, higher is the value of the amplitude field. The combination of a dispersive section, that convert the energy modulation coming from the seed to a density modulation, and an undulators line that select a specific harmonics, is the key of the High Gain Harmonic Generation. Experiments conducted more than a decade ago, demonstrated the HGHG process at infrared [54] and UV wavelengths [55] employing the third harmonic. Further works are also made on different seeding techniques, such as [56, 57, 58]. More recent demonstrations at the FERMI FEL-1 facility [5] have extended the output wavelength range down to the XUV regime with power saturation having been achieved for harmonic 13. All these experiments have shown distinct advantages of HGHG seeding over the SASE configuration, such as improved output pulse energy and central wavelength stability, reduced spectral line width, and a larger longitudinal coherence length that can be comparable to the seed coherence length. FERMI FEL-1 has been in operation since 2012 as a user facility [59], with unprecedented performances in terms of control of the properties of the pulse: as polarization [60, 61], longitudinal coherence [62, 63], and the possibility of generating multiple pulses for pump and probe experiments [64, 65, 66]. The HGHG does have some limitation. The electron beam's incoherent energy spread σ_E at modulator input, together with the chromatic dispersion in the radiator, implies a limit in the harmonic number, beyond which the microbunching structure is not enough for the emission process. There are variations to the HGHG scheme that allows to bypass this limitation, but before, due to the importance of this scheme, we are going to analyze more closely the physics behind it. We are going to consider a seeded FEL and recall the main parameters that define the emission process in the high-gain regime. First of all the Pierce parameter, from Eq. 3.22, which is a universal scaling parameter and fundamental for the definitions of the processes. Typical values for ρ_{FEL} are in the range 10^{-3}–10^{-4}, depending on the FEL operation wavelength. The exponential evolution is carried out inside the undulators line, which is designed in order to reach saturation at the end of the line, and the characteristic length is defined by the gain length as

$$L_g = \frac{\lambda_u}{4\pi\sqrt{3}\rho_{FEL}}.$$

Other two important elements that play a key role are the dispersive section

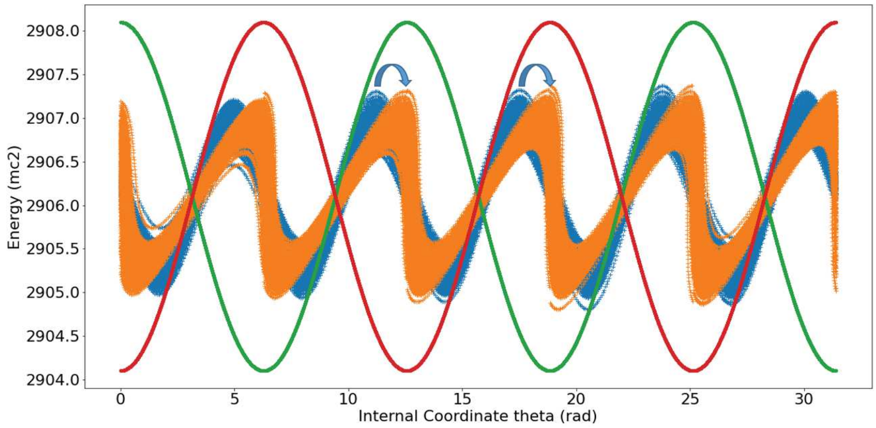

Figure 4.2: Example of phase-space before (blue dots) and after (orange dots) the dispersive section. The red and green dots are the separatrix in the phase-space. The simulation was done with GENESIS1.3 v4[45].

and the seed laser. As we already said, the seed laser imprints an energy modulation, clearly visible analyzing the longitudinal phase-space of the electron bunch, while the dispersive section converts the energy modulation into density modulations, in order to increase the initial bunching factor, accelerating the first part of the field evolution and decreasing the saturation length.
In Fig. 4.2 is represented an example of phase-space, before and after the dispersive section. As we can see the periodic modulation in the energy is establish by the seed laser (blue dots) and the coupling with the magnetic field inside the modulator. After the dispersive section, the phase-space appeared as locally rotated. In order to understand the implications of this effect we will give a briefly description of the physics behind. We start from two assumptions: we consider no gain in the modulator, since its main role is to impress the energy modulation into the bunch, and we assume also an uniform density modulation. We calculate an expression of the bunching factor after the dispersive section. In the assumption of negligible gain the amplitude of the field is a constant and we can integrate Eqs. 3.17

$$\nu'(\zeta) = \nu(\zeta, \tau = 1) = \nu(\zeta, 0) + |a(\zeta, 0)| \cos[\theta(\zeta, 0) + \Phi(\zeta, 0)],$$

$$\theta'(\zeta) = \theta(\zeta, \tau = 1) = \theta(\zeta, 0) + \nu(\zeta, 0) + \frac{1}{2}|a(\zeta, 0)| \cos[\theta(\zeta, 0) + \Phi(\zeta, 0)].$$

The parameter τ represents here a normalized coordinate of propagation along the undulator, i.e., at $\tau = 1$ we have $z = L_u$. At $\tau = 1$ the equations above provide the coordinates θ', ν' of an electron at the position ζ along the bunch, calculated at the end of the modulator. After the modulator, the beam enters the dispersive section. This is a purely magnetic device where the length of the trajectory depends on the particle energy. The dispersive section do not affect the particle energy, $\nu'' = const = \nu'$. At the exit of the dispersive section the coordinate θ becomes

$$\theta''(\zeta) = \theta(\zeta, \tau = 1 + \tau_{disp}) = \theta' + \nu'\tau_{disp} =$$

$$= \theta(\zeta, 0) + \nu(\zeta, 0)(1 + \tau_{disp}) + |a(\zeta, 0)| \cos[\theta(\zeta, 0) + \Phi(\zeta, 0)] \left(\frac{1}{2} + \tau_{disp}\right).$$

where we introduced the parameter $\tau_{disp} = \frac{R_{56}}{2N\lambda_0}$ corresponding to the dispersive strength R_{56} normalized to the characteristic dispersion of the modulator $2N\lambda_0$. The coordinates θ'', ν'' represent the position in the longitudinal phase space θ, ν after the modulator and the dispersive section. We assume a Gaussian energy distribution, independent on the coordinate ζ, and centered around ν_0

$$f(\nu, \zeta) = \frac{1}{\sqrt{2\pi}\sigma_\nu} exp\left[-\frac{(\nu - \nu_0)^2}{2\sigma_\nu^2}\right] \tag{4.1}$$

We recall that the parameter ν represents the frequency detuning and is a function of the beam energy

$$\nu = 2\pi N \left[\frac{n\omega_0(\gamma) - \omega_r}{n\omega_0(\gamma)}\right],$$

We calculate the bunching factor, defined as the discrete Fourier transform with period λ of the longitudinal electron density

.

$$b_n(s) = \frac{1}{\lambda} \int_\zeta^{\zeta+\lambda} d\zeta \int_{-\infty}^{+\infty} d\nu\, f(\nu)\, e^{-ik\theta''(\zeta)} \tag{4.2}$$

Substituting the expression of θ'' and $f(\nu)$, the bunching factor reads

$$b_n(s) = \int_{-\infty}^{+\infty} d\nu \frac{1}{\sqrt{2\pi}\sigma_\nu} e^{-\frac{(\nu-\nu_0)^2}{2\sigma_\nu^2}} \frac{1}{\lambda}$$

$$\times \int_\zeta^{\zeta+\lambda} d\zeta' e^{-\imath n\left[\theta(\zeta') + \nu(\zeta')(1+\tau_{disp}) + \left|a(\zeta')\right| \cos\left[\theta(\zeta') + \Phi(\zeta')\right]\left(\frac{1}{2} + \tau_{disp}\right)\right]}.$$

Looking at the integration in ν, we can easily perform it by including the $\nu(\zeta)$ term coming from θ''. Also, for simplicity, we call $1 + \tau_{disp} \approx t$. Using the Gaussian integration, we have

$$\int_{-\infty}^{+\infty} d\nu \frac{1}{\sqrt{2\pi}\sigma_\nu} e^{-\frac{(\nu-\nu_0)^2}{2\sigma_\nu^2}} e^{-\imath n\nu(\zeta)(1+t)} = e^{-\frac{1}{2}(nt\sigma_\nu)^2}.$$

The result above can be expressed in terms of the dispersion strength ,

$$\delta z = R_{56}\frac{\delta E}{E} \quad \Rightarrow \quad t = \frac{R_{56}}{2N\lambda_0},$$

where λ_0 is the seed wavelength and N is the number of wiggler of the modulator. Also, the frequency rms can be converted into the energy spread σ_γ as

$$\sigma_\nu = 2\pi N\sigma_\omega = 4\pi N\frac{\sigma_\gamma}{\gamma}.$$

Substituting into the exponential leads to

$$e^{-\frac{1}{2}(n\tau_{disp}\sigma_\nu)^2} = e^{-\frac{1}{2}\left(nk_0R_{56}\frac{\sigma_\gamma}{\gamma}\right)^2}.$$

Now, the bunching factor reads

$$b_n(s) = e^{-\frac{1}{2}\left(nk_0R_{56}\frac{\sigma_\gamma}{\gamma}\right)^2}\frac{1}{\lambda}\int_\zeta^{\zeta+\lambda} d\zeta' e^{-\imath n\left[\theta(\zeta')+|a(\zeta')|\cos\left[\theta(\zeta')+\Phi(\zeta')\right]t\right]}.$$

In order to solve this integral, we recall that $\theta(\zeta,0) = (k_r+k_u)\zeta \approx k_r\zeta$, since $k_r \gg k_u$ and using the Jacobi–Anger expansion we can write

$$b_n(s) = e^{-\frac{1}{2}\left(nk_0R_{56}\frac{\sigma_\gamma}{\gamma}\right)^2}\frac{1}{\lambda}\int_\zeta^{\zeta+\lambda} d\zeta' e^{-\imath nk_r\zeta'}\sum_{m=-\infty}^{\infty}(-\imath)^m J_m(nt|a(\zeta')|)\, e^{\left[\imath mk_r\zeta'+\Phi(\zeta')\right]}.$$

At this point, since we are integrating over one period at the position ζ, we can use the assumption that the field amplitude $|a(\zeta')|$ and phase $\Phi(\zeta')$ are slowly varying variables (SVEA approximation), and can be carried out of the integral. Therefore we have,

$$b_n(s) = e^{-\frac{1}{2}\left(nk_0R_{56}\frac{\sigma_\gamma}{\gamma}\right)^2}\sum_{m=-\infty}^{\infty}(-\imath)^m J_m(nt|a(\zeta)|)\, e^{\imath\Phi(\zeta)}\frac{1}{\lambda}\int_\zeta^{\zeta+\lambda} d\zeta' e^{-\imath(n-m)k_r\zeta'}.$$

The complex exponentials are orthogonal functions and the integral is a Kronecker's delta $\delta_{n,m}$.Only one term of the summation survives, for $m = n$ and the bunching factor reads

$$b_n(\zeta) = e^{-\frac{1}{2}\left(nk_0R_{56}\frac{\sigma_\gamma}{\gamma}\right)^2} J_n(nt|a(\zeta)|)\, e^{\imath\Phi(\zeta)}. \tag{4.3}$$

Finally, we observe that the field amplitude is equal to the variation of energy $\Delta\nu$ and using the definition of t, we can rearrange the argument of the Bessel as

$$nt|a(\zeta)| = n\frac{R_{56}}{2N\lambda_0}\Delta\nu = n\frac{R_{56}}{2N\lambda_0}4\pi N\frac{\Delta\gamma}{\gamma} = nk_0R_{56}\frac{\Delta\gamma}{\gamma},$$

so the final result is

$$b_n(s) = e^{-\frac{1}{2}\left(nk_0R_{56}\frac{\sigma_\gamma}{\gamma}\right)^2} J_n\left(nk_0R_{56}\frac{\Delta\gamma}{\gamma}\right) e^{\imath\Phi(\zeta)}. \tag{4.4}$$

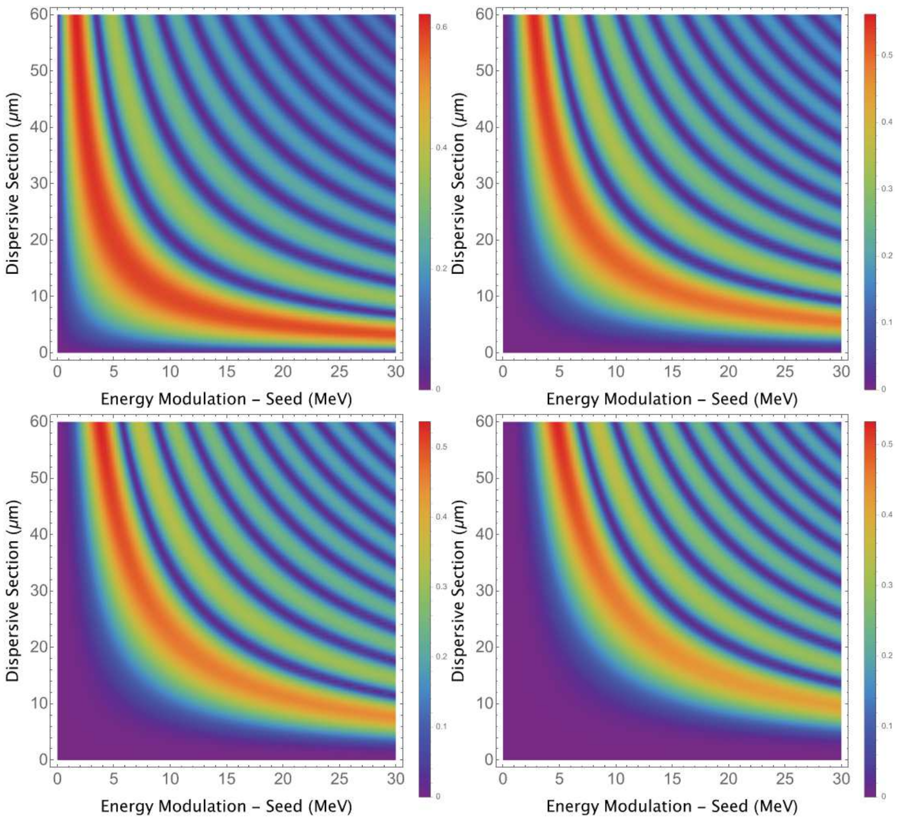

Figure 4.3: Density plots of the modulus of the bunching factor as a function of the dispersive section and the energy modulation impressed by the seed, above from left the first and the second harmonic. Below the third and the fourth harmonic.. Here $\gamma = 1.3\text{GeV}$, $\sigma_\gamma = 130\text{keV}$ and $\lambda_0 = 260\text{nm}$

In Fig. 4.3 we have plotted the absolute value of Eq. 4.4 for different values of dispersive strength R_{56} and energy modulation $\Delta\gamma$ [41]. The behavior of b_n is characterized by the hyperbola in the space $R_{56} - \Delta\gamma$. The stronger is the initial modulations the lower is the value of R_{56} required in order to reach an equivalent bunching factor. Increasing the harmonic order has the effect of pushing away the hyperbola from the origin. Furthermore, the higher is the harmonic, the stronger has to be the energy modulation, to reach the maximum initial bunching factor. From Eq. 4.4, we can understand which are the parameters that maximize the bunching factor. It's not possible to derive the extrema analytically because the equation is transcendent, but numerical approximations exist [67, 68]. According to [67] we can maximize the Bessel when the argument $X = nk_0R_{56}\frac{\Delta\gamma}{\gamma}$ is equal to X_M defined as

$$\frac{X_M}{n} = 1 + \sqrt{\frac{2}{3}}n^{-2/3}.$$

In this way we can estimate one parameter, knowing the others, and maximize the bunching factor. After the dispersive section, the bunch is ready to enters the radiators line and undergoing the exponential emission of light. The radiators are tuned in order to select a specific harmonics and dispersive section is optimized to reach saturation at the end of the line. We now address the question related to the pulse duration in a HGHG FEL. From Eq. 4.3 we observe that that the input field amplitude appears in the argument of the Bessel function, therefore the bunching factor and the generated FEL pulse will depend on the shape of the seed, through the non-linear deformation induced by the Bessel function of order equal to the harmonic order. The bunching factor seeds the amplification in the amplifier at the resonant harmonic n of the seed. The pulse shape in the early phases of the amplification process is therefore determined by the bunching factor. The amplification process has its characteristic bandwidth (see end of Chapter 3). Therefore if the bandwidth of the pulse resulting from the harmonic conversion is spectrally narrower than the gain bandwidth, the amplification process will leave unaltered the temporal properties of the pulse. Different is the case of a short seed producing a pulse spectrally broader than the gain bandwidth of the amplifier. We will analyze this condition in Chapter 6

Figure 4.4 shows the behavior of the bunching factor, for different harmonics. These results come from a simulation with GENESIS1.3v4 [45] where we have simulated a bunch going through the modulator and the dispersive section. From the right plot we observe that, higher is the harmonic number and lower is the peak of the bunching factor. Another important feature is coming from the width of the profiles. Suppose that we are able to keep the same peak value of the bunching, then the higher is the harmonic number and narrower is the profile and this is a characteristic inherited from the Bessel's function. Further, since the profile of the bunching is one of the main contributors to the profile of the field amplitude, the width of the bunching factor is tightly related to the time duration of the FEL pulse. In the article [67], they proved that the scaling

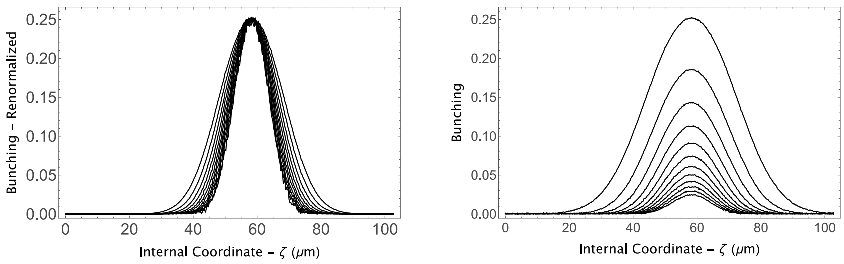

Figure 4.4: Bunching factor, after the dispersive section, for $n = 2$ to 13. The lower is the harmonic number and the higher is the peak value. The left plot is renormalized to the max value of the first harmonic.

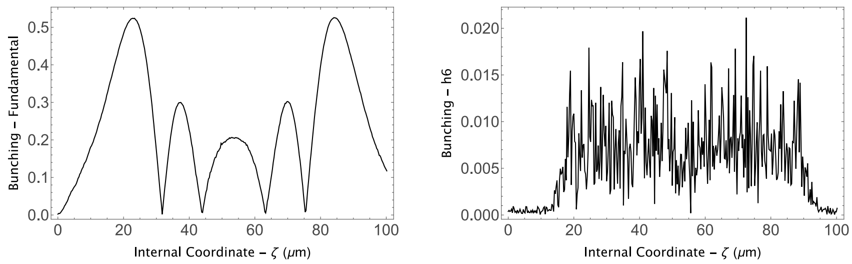

Figure 4.5: Bunching factor, after the dispersive section, for the fundamental and the sixth harmonics. In this case the dispersive section was tuned ten times higher than the optimum value, used in Fig. 4.4.

relation of the pulse duration, knowing the pulse duration of the seed, as σ_{seed}, is

$$\sigma_{\mathrm{FEL}} = \frac{7}{6}\frac{\sigma_{seed}}{n^{1/3}}. \tag{4.5}$$

This is an important relation for us, because it tells us that the shorter is the seed laser, the shorter is the pulse duration, at the beginning of the amplification process. We want to stress the fact that this relation give us the pulse duration after the harmonic conversion and not at the end of the amplification process. The temporal duration, defined by Eq. 4.5, evolves following the evolution of the gain bandwidth described by Eq. 3.23.

If the parameters are not optimized, in particular, if the dispersive section or the seed energy modulation is too high, then the profile of the initial bunching factor has no more a single Gaussian-like profile, as in Fig. 4.4, but rather has multiple peaks. This condition is called overbunching. The overbunching situation is reached also after the exponential evolution, in a HGHG scheme.

As reported in Fig. 4.5, the overbunched condition is characterized by multiple peaks, that come from the Bessel function and its oscillating behavior for large

values of the argument. The correspondent harmonic up-conversion, in this case we reported just the sixth harmonic, gives rise to a very noisy bunching, that reassemble the SASE behavior. Despite this bad behavior for a simple HGHG scheme, the overbunching condition can be used, conjointly to other setups, to provide a further expansion in the light productions. For example, if we consider a phase $\Phi(\zeta)$ in Eq. 4.4, with a controlled quadratic chirp, and a two peaks overbunching situation, we can tune both bunching peaks at a slightly different wavelength, therefore the FEL pulse will be the superimposition of two wavelength simultaneously. This light production scheme is called *two-color scheme* [65] and firstly observed in [69].
At FERMI, the two-color scheme was characterized by [65, 70]. In Fig. 4.6 is reported the analysis done in the experimental session: the bunching factor profile was studied as a function of the chirp in the phase of the seed laser. At the Fourier Transform Limit (FTL), when the quadratic chirp is zero, the FEL spectrum is inheriting the multi-peak behavior of the bunching factor. When the quadratic chirp is present (this is more clear looking at the bottom figure), the seed energy is slightly different between the head and the tail of the light pulse. This different energy in the seed, combined with the high energy modulation (therefore an overbunching situation), generates two pulses in the time domain with a different resonance condition. Since the two pulses are no longer at the same resonance condition, they cannot have the same wavelength and, therefore, there will be no interference pattern in the spectrum. In fact, the spectrum is made by two separated pulses in the wavelength domain. This scheme is currently an available possibility for the beamlines and already in use since a couple of years. With this we have finished the description of the HGHG scheme and in the next section we are going to describe how FERMI works.

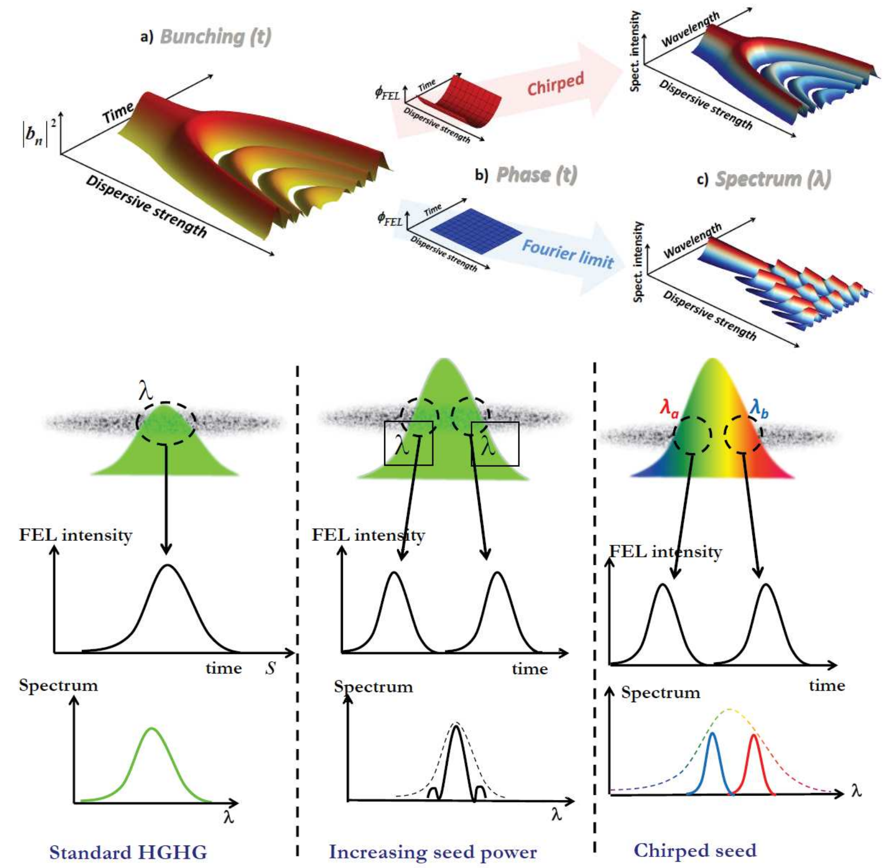

Figure 4.6: Above: the behavior of the bunching factor with respect to the seed phase. The FEL pulse can be shaped by manipulating the electron bunching envelope and FEL phase. The bunching envelope, which corresponds to the temporal FEL pulse shape, is optimized for maximum bunching just before bifurcation, resulting in a single peak. Increasing the dispersive strength leads to peak splitting and a multi-peak structure due to electron overbunching. The spectral map of the FEL spectrum strongly depends on the FEL phase, with a direct correspondence between the temporal and spectral domains for a significantly chirped FEL pulse. However, a Fourier-limited pulse with a flat phase develops distinctive features in the spectral map with increasing dispersive strength due to interference between the individual peaks in the multi-peak bunching structure. The bunching and spectral maps are normalized in amplitude for each value of the dispersive strength for visualization purposes.Below: the concept of the two-color scheme.

Chapter 5

FERMI Free Electron laser

5.1 LINAC

The FERMI accelerator is schematically shown in Fig.5.1 [71]. It consists of five linac segments L0 – L4, two bunch compressors (BC1 and BC2), a laser heater and a spreader, i.e. the transfer line where the beam is delivered to two FEL lines. The operation of the FEL lines is exclusive, that is, the two FELs are operated alternately, during different time periods. The electrons are generated at the electron gun cathode by the interaction of a ~ 5 ps laser pulse from the photoinjector laser (PIL) with the flat Copper wall of the cavity, and accelerated up to about 5 MeV by the radiofrequency gun [72]. After the gun, the bunch is accelerated up to about 100 MeV. Here a Laser Heater (LH), i.e. a device that adds a controlled amount of incoherent energy spread to the electron beam, is used to suppress microbunching instability growth via energy Landau damping [73]. At this stage the energy of the beam is ˜100 MeV. The beam here has approximately the same peak current 60-70 A, that had at the exit of the gun. The LINAC section L1 is then used both for increasing the electron-beam energy (up to about 300 MeV) and for inducing a controlled energy chirp, necessary for electron-beam compression. In order to achieve high peak current the electron beam must be manipulated in longitudinal phase space. The radiofrequency of some of the klystrons driving L1 is dephased by about 26 degrees with respect to the value providing the maximum energy, in order to induce a correlation between the energy and the position along the bunch. This correlation is exploited in the the first Bunch Compressor (BC1) to reduce the bunch length and to increase the peak current. The compressor BC1 consists of a chicane built from four rectangular bending magnets where the electron trajectory length is correlated to the energy. Since more energetic electrons follow shorter paths, the bunch, traveling through the bending magnets, will be compressed by a factor

$$C = \frac{1}{1 + hR_{56}},$$

where R_{56} is the dispersive value (negative by convention) and $h = dE/dz$

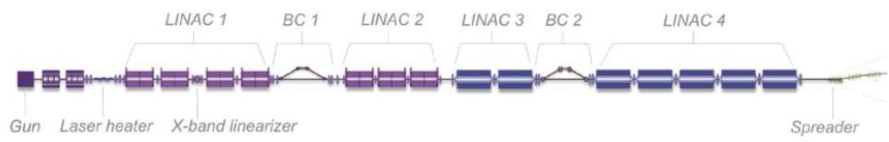

Figure 5.1: Schematic representation of the accelerator line at FERMI

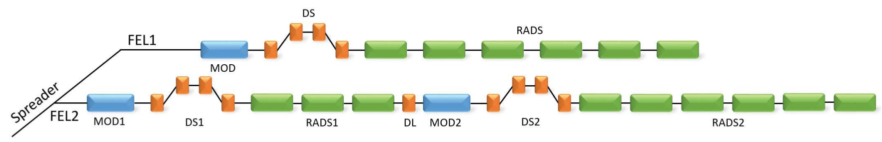

Figure 5.2: Schematic representation of the undulators lines FEL1 and FEL2 at FERMI

(negative by the cavity phase setting) is the linear chirp in the bunch energy. After the BC1 section the bunch is accelerated up to the desired value by the three remaining linac segments (L2,L3,L4). Between L3 and L4 there's a second bunch compressor, which is identical to BC1, and would allow a much stronger compression factor. At present this is not used in the baseline working mode of FERMI for its detrimental effect on the beam energy spread. At the end of acceleration line L4 the electron beam energy can range between 750 MeV up to 1.3/1.5 GeV (depending on the beam repetition rate, at 50/10 Hz respectively).The electron peak current after compression ranges from 500 A to higher values (up to 1000A), depending on the bunch length needed for the FEL operating modes. The nominal value for the current is 700 A.
After the accelerators line, a spreader line, which consists in rectangular bending magnets, deflects the electrons and select one of the two undulator lines: FEL-1 and FEL-2.

5.2 Undulators Lines

In Fig. 5.2 we have sketched the two undulators lines. Both rely on the High-Gain Harmonic Generation scheme, which was previously introduced. FEL-1 is based on one stage (one harmonic conversion). FEL-2 instead, uses two harmonic conversions to reach higher harmonic orders. The first stage of FEL-2 is equivalent to FEL-1 (same undulator's parameters, see Tab. 5.1).
The first modulator (MOD and MOD1), must satisfy FEL resonance over a nominal seed wavelength range of 240 to 360 nm, has 30 periods with length of 10 cm, for a total length of 3m. Inside the modulator, the seed laser is injected

	Undulator Parameters					
	FEL1			FEL2		
STAGE	N. Periods	Periods (cm)	Polarizations	N. Periods	Periods (cm)	Polarizations
Modulator	30	10.036	LH	30	10.036	LH
1° stage	42	5.52	LH/LV/RC/LC	42	5.52	LH/LV/RC/LC
Modulator				42	5.52	LH/LV/RC/LC
2° stage				62	3.48	LH/LV/RC/LC

Table 5.1: Undulators parameters at FERMI.

in order to modulate the electron beam. The seed is linearly polarized in the horizontal plane, the modulator has the same linear horizontal polarization to ensure the best coupling to the seed. After each modulator, a dispersive magnetic chicane (DS and DS1) converts the energy modulation into the coherent micro-bunching . For reasonably large input seed powers (*e.g.* $\geq$ 10 MW) and short wavelengths ($\lambda_0 \leq 300$ nm), the necessary R_{56} dispersion parameter is up to ~100 µm in the first stage modulator. The bunching structure is therefore impressed on the electron beam distribution and the bunch is ready to initiate the amplification process in the respective amplifiers, RADS and RADS1, where one of the higher order harmonics of the modulation seed are amplified. Both FEL-1 and the first stage of FEL-2 have radiators with 42 periods of length 5.52 cm, for a 2.4m total length. The radiators can be set for linear (horizontal and vertical) and circular (left and right) polarization. The spectral range of FEL-1 and of the first stage of FEL-2 covers the range 100-20 nm . On FEL-1, at the end of the radiators line, the electron bunch is deviated by a magnetic chicane and transported to the Main Beam Dump (MBD), where the bunch is stopped. The light pulses are instead transported by the photon line delivery system to diagnostics and to the experimental hall downstream. In FEL-2, after the first stage, a delay line (DL), which consist in a dispersive section with a larger dispersion that that of DS or DS1 , retards the electron bunch by ~300 fs, in order to shift the light coming from the first stage to a fresh, unseeded region of the bunch. Here a new energy modulation occurs, and the HGHG process is repeated starting from the short wavelength seed generated as the output of the first stage. This technique is called *Fresh-Bunch* scheme, was proposed in [74, 75] and demonstrated at FERMI for the first time [64]. The second modulator of FEL-2 (MOD2) has the same parameters of the first stage amplifier since the two have to share the same range of resonance wavelengths; the final amplifier of FEL-2 instead, after the second harmonic conversion covers the range of resonances from 20 nm to 4 nm, and requires therefore a shorter undulator period. These modulate are composed by 66 periods with a length of 3.48cm each, for a 2.3m of total length. After the radiators line, the bunch is deflected to MDB through the same line for FEL1.
FERMI uses the properties of free electron lasers to generate extremely intense,

ultra-short pulses of infrared, visible, and ultraviolet light. These high-intensity, highly-coherent light pulses are used in a wide range of scientific and industrial applications, including spectroscopy, imaging, and materials science. The light produced by FERMI is extremely intense, with peak powers reaching up to several GW, is highly coherent, meaning that the phases of the light waves are tightly synchronized. This coherence allows for precise measurements and manipulation of samples, light pulses produced at FERMI are very short, on the order of femtoseconds to attoseconds. This short pulse duration allows for the study of ultrafast processes and the precise control of chemical reactions. Further, the light can cover a broad range of wavelengths, from the far infrared to the soft X-ray region. These and other characteristics such as stability of the wavelength over shot-to-shot pulses, fine tunability and the ability to manipulate the light pulses in a various way enable scientists to study a wide range of phenomena at the atomic and molecular level with unprecedented precision and control.

As an example of some of the properties of FERMI capability, we have reported in Fig. 5.3 a collection of 2000 spectra acquired during a machine tuning, at 27nm. The analysis of the spectra reveals a very good stability in time, with a $\Delta\lambda/\lambda = 7.77 \cdot 10^{-4}$, indicating a very narrow bandwidth.

In general, FEL-1 is characterized by a high degree of longitudinal and transverse coherence and high wavelength stability (fluctuations <10-4 rms, typically). The seed is generated by an optical parametric laser amplifier (OPA). Covering the whole FEL tuning range (100-20 nm) requires the variation of the electron-beam energy, which is not possible during the same user beam time. Typical tuning ranges available for a given experiment are 65-20 nm or 100-30 nm. The FEL is available in four polarization states: linear horizontal, linear vertical, circular right and circular left. The best performance in terms of FEL power and spectro-temporal quality is obtained when the FEL is seeded using the third harmonic of the Ti:Sapphire amplifier (around 261 nm). In this case, the FEL light is produced at the integer harmonics of the seed.

In Fig. 5.4 are reported the wavelength of the FEL pulse achievable, versus the electron beam energy. The colors represent the estimated energy content in the FEL pulse, at the source, for circular polarization and linear polarizations. For FEL-2, the fresh bunch scheme allows the decreasing of the wavelength range towards EUV-soft X-rays, as reported in Fig. 5.5.

The seed laser system contains two Ti:Sapphire based regenerative amplifiers (RGA) seeded by a single mode- locked ultrafast oscillator (Vitara HP, Coherent). The latter is locked with high precision (relative timing jitter $\leq$ 3 fs RMS) to the reference timing signal by the use of a Balanced Optical Cross-correlator. In the case of FEL-1, for providing full tunability in the range 20-100 nm (covering also 18-20 nm at present), two OPA ranges need to be used, namely 232-267 nm (Second Harmonic Sum Frequency Signal OPA process, SHSFS) and 295-365 nm (fourth Harmonic Signal OPA process, FHS). In the case of FEL-2, the spectral range 4-20 nm has to be covered. Taking into account the need for higher peak power of the seed pulse and the higher losses of the grating compressor at shorter wavelengths, the seed tunability used in FEL-2 mode is

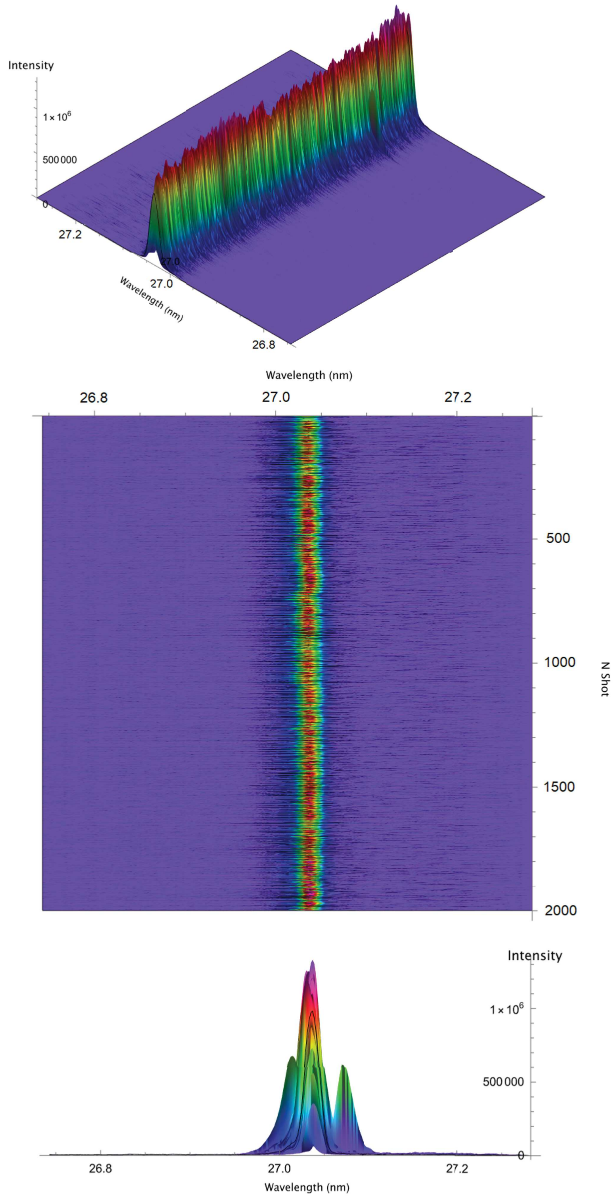

Figure 5.3: Example of the stability achievable at FERMI, FEL-1. A collection of 2000 spectra acquired during a beamtime preparation at 27nm with $\Delta\lambda/\lambda = 7.77 \cdot 10^{-4}$.

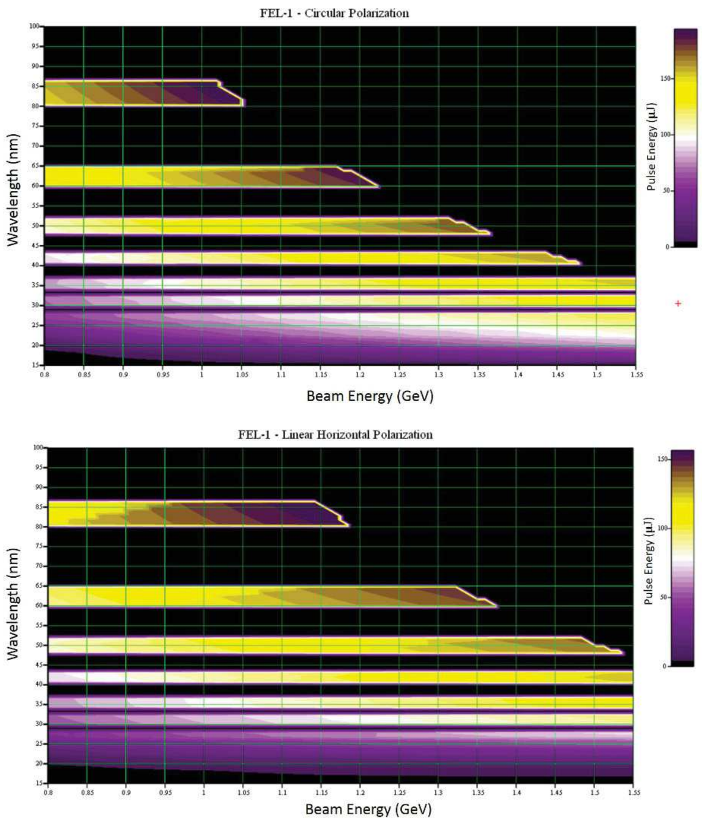

Figure 5.4: Plots of the wavelength achievable as a function of the Linac energy for FEL-1. The colors indicates the nominal energy per FEL pulse.

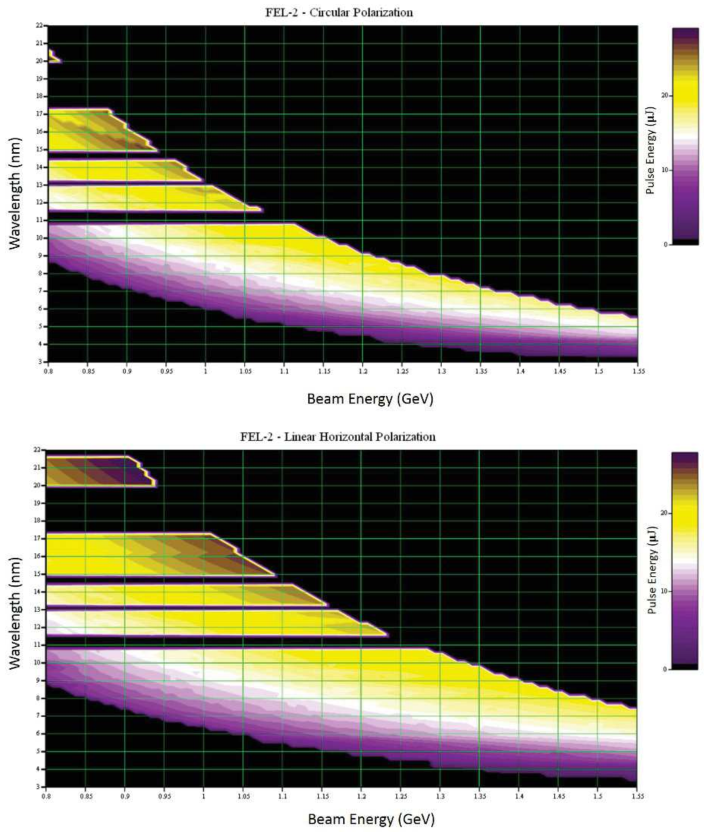

Figure 5.5: Plots of the wavelength achievable as a function of the Linac energy for FEL-2. The colors indicates the nominal energy per FEL pulse.

typically reduced to 238-267 nm, which allows one to obtain a nearly full coverage of the range. Seeding with THG (third harmonic generation) here has an advantage due to the higher peak power, pulse quality and stability compared to OPA generated pulses. THG seeding also permits pulses of duration < 50 fs FWHM. The usual pulse duration for the OPA is around 100fs [76]. The usual scheme for light production at FERMI is the HGHG for FEL-1 and HGHG + fresch bunch injection for FEL-2 [5, 64, 6]. During the years, different other schemes have been tested and commissioned for users availability: The generation of two-colour extreme ultraviolet pulses of controlled wavelengths, intensity and timing by seeding of high-gain harmonic generation free-electron laser with multiple independent laser pulses [77, 78]; A two-color scheme in which a single-pass free electron laser (FEL), in a dynamical regime, can be exploited to perform two-color pump-probe experiments in the vacuum ultraviolet or x-ray domain, using the free-electron laser emission both as a pump and as a probe[65]; The possibility to achieve ultrashort pulses at EUV-soft X-rays in a seeded FEL using a superradiant cascade [13, 79, 14]; A scheme to provide transversely separated pulses with parallel or crossed linear polarizations. This configuration permits to explore additional features, in particular, the possibility to excite a transient polarization grating on the sample [80]; Generation of FEL pulses at the water window by exploiting the so-called nonlinear harmonic regime, which allows generation of radiation at harmonics of the resonant FEL wavelength [81]. In the following we are going to enter into details of some of the schemes studied at FERMI for the generation of ultrashort pulses.

Chapter 6

Superradiance

Saturation is a nonlinear process in which the electrons have lost enough energy to be no longer in resonance with the field. As the evolution of the exponential regime goes on, the electrons rotates in the longitudinal phase space. When they reach the bottom of the bucket, the emission process ends and they start to re-acquire energy. While there isn't a net new contribution to the field amplitude, the light, already produced before, still interacts with the electrons. In particular, the light produced during the exponential evolution has one third of the speed of light in the electron's reference system. The slippage corresponds to the distance covered by the FEL pulse over the longitudinal coordinate of the bunch in the electron beam reference frame. During saturation, the light starts to recover its own speed. In this way, the slippage starts to increase and the light is able to modulate new, fresh, electrons, extracting new energy from them, while the electrons in the tail of the light pulse are no longer in condition to reabsorb the light, because it has slipped away. In this regime of operation the power extracted from the beam scales as the square of the bunch charge and it is known *as superradiant regime* [82] In the framework of FEL physics was first studied *in* [83, 84, 85, 86, 11, 87, 88, 89].
In Fig. 6.1 we have reported a simulated pulse along the FEL-1 amplifier. The length of the amplifier used in the simulation is actually twice the effective length of the amplifier of FEL-1 to observe the pulse evolution in strongly saturated conditions. The evolution is plotted as a density map of the peak power (color intensity), as a function of the undulator position (vertical axis) and the internal coordinate of the electron bunch (horizontal axis). The light pulse is moving along the internal coordinate ζ, while evolving along the undulators line. The slope drawn by the evolution of the pulse, over the space (ζ, z) represents the velocity of propagation of the pulse. This velocity is different at the beginning and the end of the process: during the exponential amplification the pulse travels over the current distribution at a velocity that is about $c/3$ in the beam frame. After the saturation the velocity increases up to c and the slippage increases as in the propagation in vacuum. This is one of the distinguishing features of the superradiant regime: the pulse duration decreases during the evolution.

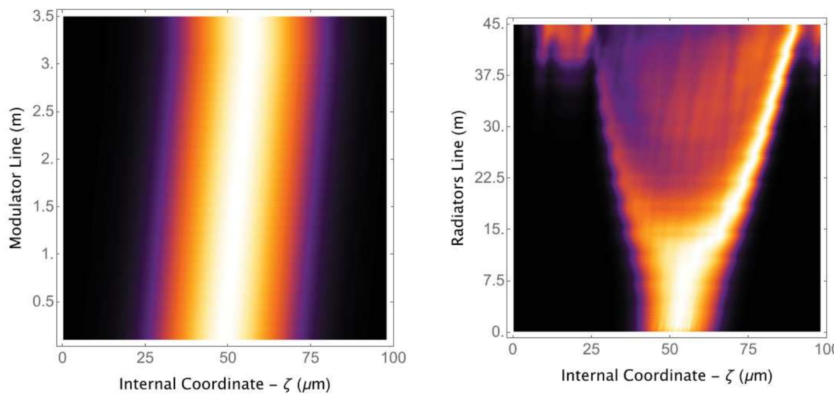

Figure 6.1: Evolution of the light pulse along the FEL1 line. The brighter zones corresponds to higher powers. The left plot is inside the modulator, while the right plot is inside the radiators line. (Simulations done with Genesis1.3v4. The radiators line is twice the actual length in order to reach the superradiance.)

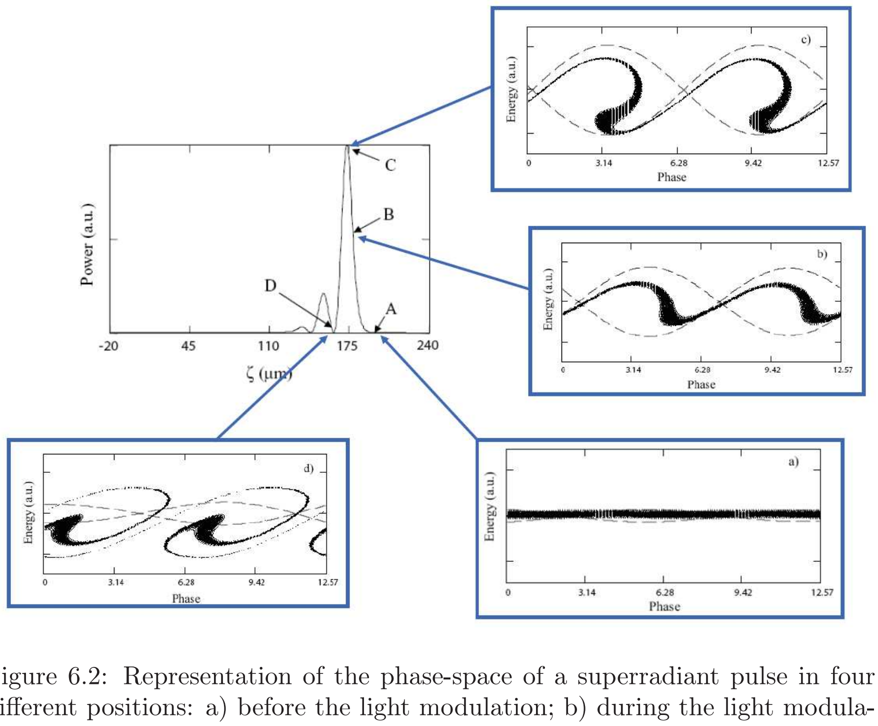

Figure 6.2: Representation of the phase-space of a superradiant pulse in four different positions: a) before the light modulation; b) during the light modulation; c) during the light modulation, at the maximum of the process; d) after the light modulation, when the pulse has slipped away.

In Fig. a simulated superradiant pulse is shown [11]. The figure represents a snapshot of the field distribution vs. ζ, at some fixed position along the undulator line. The plots, a,b,c,d represent the longitudinal phase-space in four different positions along the pulse . In a temporal sequence, considering that the radiation pulse is propagating over the beam, we may imagine that the phase-space plotted in point A will become the one in point B, then in the point C and finally in the point D. The first position (A) corresponds to the situation where the electrons are not yet affected by the interaction with the light pulse: the beam is not modulated in energy . In this situation the separatrix the motion whose amplitude is proportional to the square root of the field amplitude are close each other. The unmodulated beam is substantially not emitting any light, if we exclude a residual SASE background. The position corresponding to B is instead reached by the optical pulse. The bucket potential corresponding to the larger separation between the separatrices is deeper, the beam is modulated in energy and partially in phase, the electrons emit light in resonance with the wave that is indeed amplified . In plot c), corresponding to the position C along the pulse, the electron beam is fully modulated and has lost a consistent amount of energy. The energy loss has brought the density modulation out of phase with the field. This stops the amplification process and the field amplitude is is maximized and the pulse reach the peak power value. In D instead the phase mismatch increases up to bringing the electron bunching that is now completely out of phase with the field, to reabsorb all the energy available in the field at that position, causing the complete absorption of the field and the emission of a new pulse out of phase by π with respect to the main pulse. The number of electrons participating to the emission is reduced at each cycle because of the induced dispersion in energy and phase, therefore the amplitude of these secondary peaks decreases. In summary, in these conditions the light, traveling along the bunch, continuously modulates new electrons, extracts energy from them and slips away before the electrons are able to reclaim back the energy.
In order to understand why the pulse duration decreases and the others scaling laws, we consider the motion inside the buckets formed by the separatrix [11]. The electrons enter the bucket while they are distributed horizontally in the phase-space (see plot a) in Fig. 6.2). The motion is clockwise and the emission process will end when the electrons reach the bottom of the bucket, so after traveling 1/4 of the rotation period in the phase-space. Looking at the equations of motion, like Eq. 3.17 for example, we see that the frequency of the rotation, called synchrotron frequency is $\Omega_s = \sqrt{a}$. Therefore, the synchrotron period is $\delta\tau_s = 2\pi/\Omega_s$. In this time interval, the slippage length for a pulse propagating at c is $\Delta_s = \delta\tau_s N\lambda_0$, therefore, if the pulse length is comparable to the slippage length, in just a 1/4 of the period we have that

$$\sigma_s \approx \frac{\pi N\lambda_0}{2\sqrt{a}} \propto \frac{1}{P_{FEL}^{1/4}},$$

since the power scales with the square of the field amplitude. The energy carried by a pulse of duration σ_s is by definition

$$E_{FEL} \propto P_{FEL}\sigma_s \propto P_{FEL}^{3/4},$$

at the same time we may expect that the energy collected by the pulse is proportional to the distance covered by the pulse over the current, that is proportional to the trapped number of electrons, multiplied by the depth of the separatrix, that is proportional to the electron energy loss Ω_s

$$E_{FEL} \propto \zeta_s \Omega_s \tag{6.1}$$

where s is the number of trapped electrons inside the bucket and Ω_s can also be seen as the bucket depth. The number of the electrons can be estimated by considering a pulse with a group velocity c and so $\zeta_s = z - \beta_z t \simeq z_u \lambda_0/\lambda_u$, where z_u is the position along the undulator line. Combining also the elements we have

$$E_{FEL} \propto s\Omega_s \propto z_u P_{FEL}^{1/4} \Rightarrow \begin{cases} P_{FEL} \propto z_u^2, \\ E_{FEL} \propto z_u^{3/2}, \\ \sigma_s \propto z_u^{-1/2}. \end{cases} \tag{6.2}$$

The last of Eqs. 6.2 shows that the duration of the first peak in the pulse decreases with the square root of the position along the undulator. In the light of these explanations, we note in Fig. 6.1 during and after the exponential amplification the pulse duration grows At saturation the amplification stops, the peak power in the central part of the pulse saturating earlier decreases and the pulse splits in two peaks. The front peak, propagating over fresh electrons is favored with respect to the rear one, propagating over electrons heated by the FEL process. The pulse in the trailing edge as well as the central heated region affects the quality of the light and introduce spurious contributions. To further suppress the tails there are various ways, an higher energy spread can be impressed in the region associated to the tail, for example [90]. This contribution is also partially suppressed in a superradiant cascade, that represent an interesting method to reduce the pulse duration at FERMI.

6.1 Superradiant cascade

Using the higher harmonic radiation or premodulated e-beam from another FEL to seed a single-pass FEL section is a promising method for expanding the operating wavelength range of a FEL. This has been studied in literature and tested experimentally in a single stage configuration. However, when the beam is propagated in a FEL cascade, the growth of energy spread in the first stages can inhibit FEL gain in the following stages. One solution is the "fresh bunch injection technique" which uses a dispersive section between two FEL stages to remove residual bunching and shift the radiation pulse to a portion of electrons where the beam quality has not yet been affected by the FEL process.

This allows the FEL to restart with a fresh beam and initiate a new sequence of harmonic multiplication. The design of a device based on this scheme is challenging due to various factors, including the bunching at a given stage being affected by input signal, gain and length of undulator sections, and dispersion of intermediate sections. Additionally, a chain of amplifiers can amplify noise and degrade the signal-to-noise ratio. Despite these challenges, operating a FEL cascade is attractive for improvements in FEL radiation performance such as stability, linewidth, short pulse generation and pulse shape control. However, these difficulties limit the feasibility of a cascade with a high number of stages to extend final wavelength to the subnanometer range of the spectrum. The super-radiant solution is particularly interesting in a cascade because it is a stable configuration for the coupled system of fields and particles. Additionally, the higher-order harmonic emission demonstrates strong bunching on the front side of the pulse. When passing through a stage of harmonic multiplication in a cascade, the beam portion with a high nth harmonic bunching coefficient will coherently radiate the respective harmonic field, producing a short burst of radiation that will start slipping over the electron bunch. In the following we are going to provide experimental demonstration of a superradiant cascade configuration.

6.2 Experimental tests of a superradiant cascade at FERMI at the 18th harmonic of the seed

The superradiant cascade at FERMI has been studied and characterized in the last years as a method for producing short pulses while still delivering high pulse intensities, even in excess of the saturation power [14, 79]. This scheme was largely investigated on FEL-2. FEL-2 is configured as a three stages cascade where the three conversions are by a triple harmonic jump. Following Fig.6.3, the first modulator Md1 act as in the HGHG setup, modulating the seed and coupling it with the electron beam. Then, the first dispersive section DS1 is set to an high value, in order to reach saturation after the first conversion, already at the end of the first stage. The first stage is composed by only two of the radiators of the first stage (line Rd1 in fig. 6.3, a). Then the second stage is made by tuning the third radiator of the first stage and the second modulator MOD2 to an harmonic of Rd1. We indicate this radiator as Rd2. The delay line DL is set with a dispersion close to zero, its role is that of a a phaseshifter, as in this configuration the large fresh bunch injection typically required by FEL-2 is not desired. The second dispersive section is set to zero, because the beam reaches Rd3 already in saturated conditions. Rd3, is set to reach the final harmonic, in the example represented in Fig. 6.3it is h18 corresponding to 14.7 nm.

These experiments were carried out in 2019, on the FERMI FEL-2 line, during three experimental sessions, labeled A, B and C. The beam/undulator parameters changed slightly from one session to another and are listed in Table 6.1.

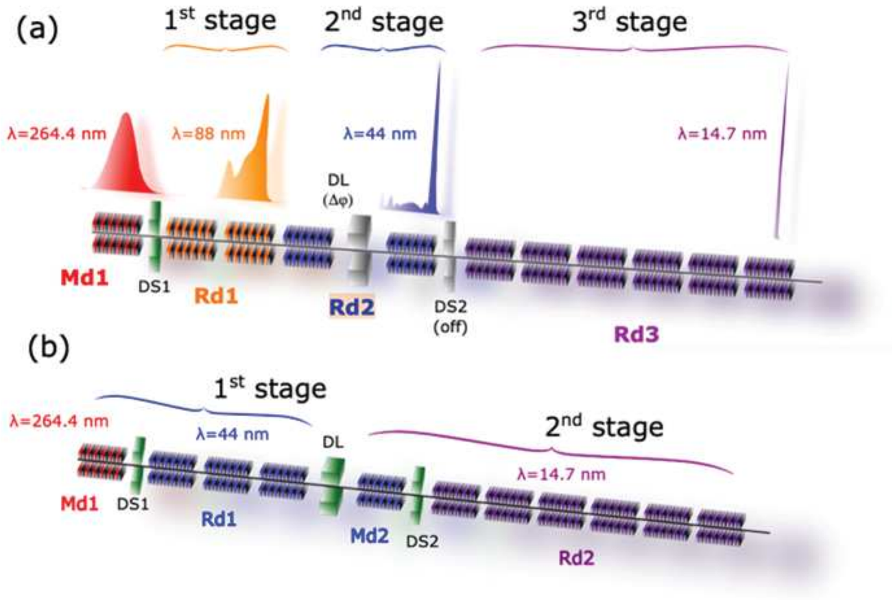

Figure 6.3: FEL layout. **a**, FEL-2 in SRC mode. Above the lines are reported the power profiles coming from simulations made with GENESIS, with the same parameters reported in Tab. 6.1, column **B**. **b**, FEL-2 layout for the HGHG mode

Beam/seed parameters	A (SRC/HGHG)	B (SRC)	C (HGHG)
Beam energy (MeV)	750 ± 1	900 ± 1	940 ± 1
Peak current (A)	700 ± 30	700 ± 30	700 ± 30
Energy spread (keV)	130 ± 30	<80	<80
Beam size (μm)	90 ± 10	92 ± 10	90 ± 10
Seed wavelength (nm)	264.4 ± 0.1	266.2 ± 0.1	250.0 ± 0.1
Seed energy (μJ)	40 ± 2	44 ± 2	31 ± 2
Seed duration (fs)	55 ± 5	55 ± 5	90 ± 5
Harmonics up-shifts	3 × 2 × 3 / 6 × 3	3 × 2 × 3	7 × 3
Undulator parameters (SRC/HGHG)			
Undulator		Period (cm)	Periods
MOD1		10.036	30
RAD1 and RAD2/RAD1 and MOD2		5.52	42
RAD3/RAD2		3.48	66

Table 6.1: Parameters of the machine during the different experimental sessions

The wavelength (14.7 nm) was chosen to be attainable from the seed (264.4 nm) as a triple harmonic jump, $3 \times 2 \times 3$. During the experimental sessions we acquired the spectra, the mean energy per pulse, the time duration of the light pulses and the energy as a function of the number of radiators of the last undulators line, in order to obtain the gain curve. All these data were filtered principally to remove the contribution of the jitter and the background.
From Fig.6.4, we can see some of the main features of the superradiant cascade, together with the power profiles that appears in Fig.6.3, above the correspondent sections of the radiators line. The first spectrum, has sidebands, one on the left and one on the right, that indicates the presence of overbunching. The spectrum then is cleaned by the harmonic conversion and the sidebands disappear, leaving just the right peak of the bunching. From the power profiles of the first and second stage, we see that there are two main peaks (the head and the tail). These two peaks can be seen as two sources of light with the same properties, therefore we expect to have a pattern of interference in the spectrum, coming from the Fourier transform of the two-point source power profile. We can also see that, by lowering the intensity coming from the tail, also the pattern of interference becomes weaker. The last stage almost completely clean the residual of the tail and the superradiant evolution is carried on in the remaining peak. The fringes that appear in the first and in the second stage are due to distance between the source and the spectrometer: since these are generated at the beginning of the line, the light mode can grows more and reach the dimensions of the vacuum chamber, with which interacts causing a diffraction pattern. Further, from the spectra at the end of the first and the second stage, we can clearly see that the distance between the peaks of the overbunching is shrinking: since spectrum and power profile are Fourier related, a lowering in the distance between two spectra peaks, imply and increase between the peaks in the temporal domain. As already discussed, the pulse duration of a superradiant pulse decreases with the inverse squared root of the position in the undulators line. In the experiments, we acquired 1000 spectra, in order to have a sufficient set of data and to properly

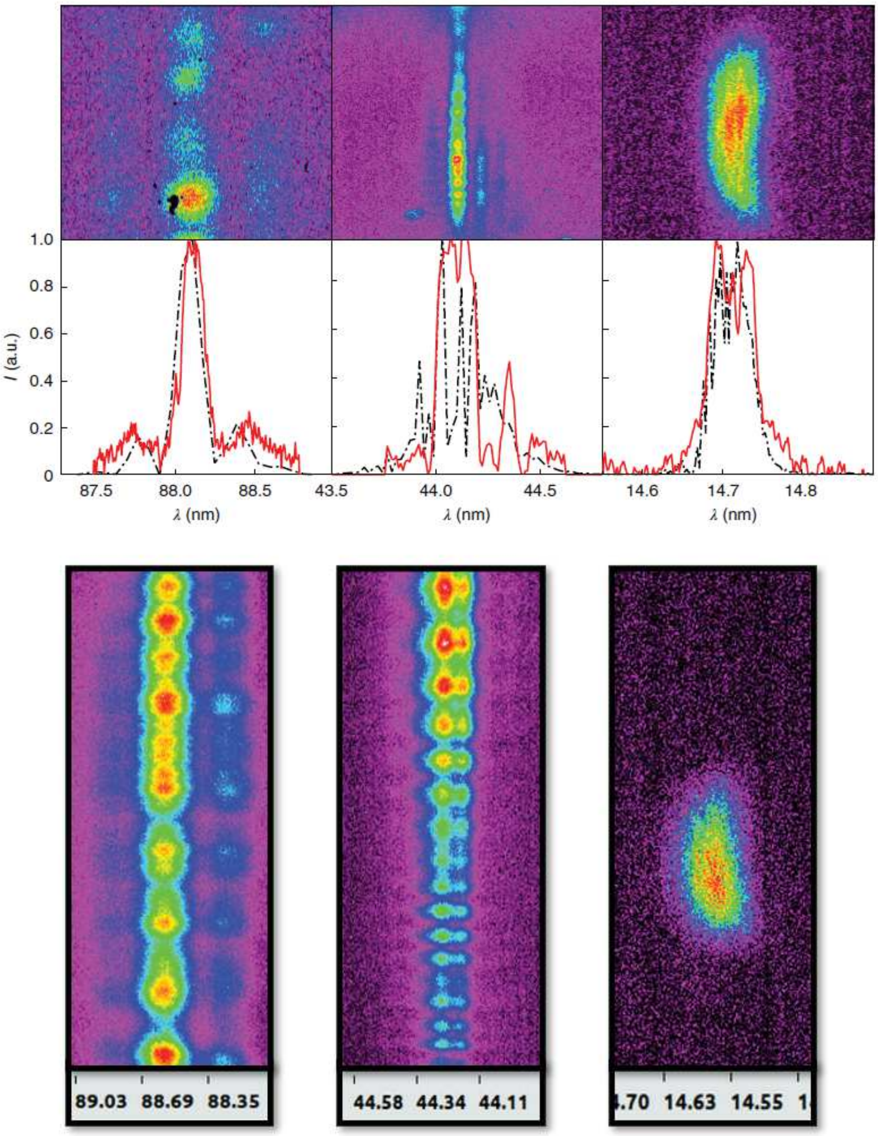

Figure 6.4: Example of spectra during the experimental session. From the left to right, respectively the first, the second and the last stage spectrum (scale in nm on the x-axis and intensity in a.u. on the y-axis). Top: measured (above) and simulated (below) spectra during the first experimental session. Bottom: measured spectra acquired during a second experimental session. The fringes are due to diffraction with the vacuum chamber (see text for details).

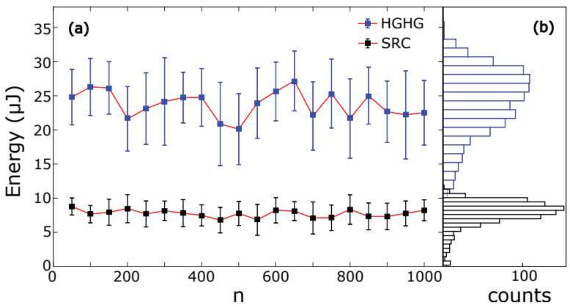

Figure 6.5: Top: Energy measurements for HGHG and SRC (**a**) and correspondent binning distribution (**b**)

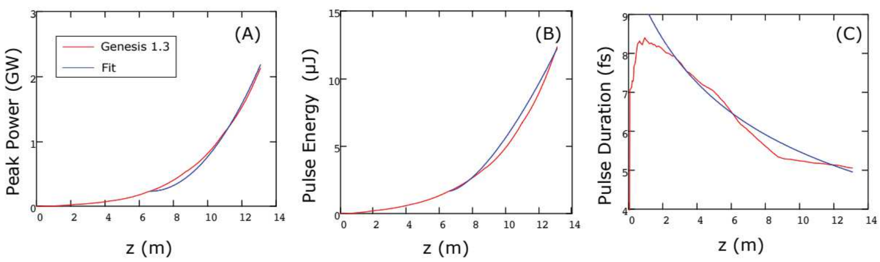

Figure 6.6: Comparison between the scaling laws in SCR and the simulated data from GENESIS simulation, respectively for peak power (A), pulse energy (B), pulse duration (C). The parameters used are the same reported in Tab. 6.1, column B

analyze them.
Figure 6.5 (**a** and **b**) shows the pulse energy measured in a sequence of 1000 consecutive pulses. The averages (± one standard deviation) of the energy distribution were 7.7 ± 1.8 µJ and 23.5 ± 5.2 µJ in SRC and HGHG mode respectively. The resulting shot-to-shot relative stability in the two configurations is comparable (24% in SRC vs. 22% in HGHG). The simulations (Fig. 6.6) reproduced very well the pulse energy and duration at the end of the cascade. We compared the behavior of peak power (A), pulse energy (B) and pulse duration (C) vs. coordinate along the undulator z (physical drifts of 1.35 m in between the undulators were removed). The trends are compared with the fit functions (in blue) for power $P_{peak}(z) = P_0 + \alpha_P(z - z_0)^2$, energy $E(z) = \alpha_E(z - z_0)^{3/2}$ and duration $\delta t(z) = \alpha_t(z - z_{t_0})^{-1/2}$ with the following fit parameters: $P_0 = 0.23$GW, E_0 =1.7 µJ, α_p =46.5 MWcm^2 , $\alpha_E = 0.64$µJm$^{3/2}$, $\alpha_t = 20.5$ m$^{-1/2}$,$z_0 = 6.5$ m and $z_t = -4$ m. In all of these cases, we have confirmed the scaling laws that characterize the superradiant process. The FEL amplification process is initiated by a strongly bunched, "short" region of the beam: in the early part

of the final radiator the field is generated by coherent harmonic generation, where the power grows as z^2 but where also the pulse duration is expected to grow, and not to decrease with z. The dynamics evolves from this regime to exponential regime and then to superradiance without a clear distinction between these different regimes. The self-similar pulse evolution, that we indicate as superradiance, becomes dominant after the trend of the pulse duration vs. z changes slope and starts to decrease, i.e. when saturation effects erode the rear part of the pulse and begin to shrink its duration. The experiment was designed to include an autocorrelation measurement, to provide direct evidence of the pulse duration.The FEL pulse passed through the FERMI split-and-delay line AC/DC [91] and we monitored the (energy resolved) photoelectron signal of two-photon above-threshold ionization (ATI) of Ar at the LDM (low density matter) beamline [92, 93]. A magnetic bottle electron spectrometer, was installed and configured to detect either electrons or ions. The spectrometer design has been previously described. Argon gas was injected into the source chamber using a pulsed valve and directed into the detector chamber through a skimmer. The electron time-of-flight signal was recorded shot-by-shot with a fast digitizer and saved for later analysis. The focal shape and position of the FEL beam were initially projected onto a YAG screen in the interaction region, and then optimized using a Shack-Hartmann wavefront sensor. The gas jet, the FEL beam and the spectrometer axis were arranged to be mutually perpendicular.

The autocorrelation traces for the SRC and the HGHG FEL configurations respectively, are shown in Figs.6.7 (**a**) and (**b**): the full width at half maximum (FWHM) pulse duration derived therefrom is $\delta t_{fel} = 4.7 \pm 0.6$fs in SRC mode; in HGHG mode is 22 ± 4 fs. The average spectral width, calculated as the FWHM of a Gaussian fit of the spectrum, was 0.063 ± 0.007 nm and 0.021 ± 0.007 nm for SRC and HGHG respectively. The uncertainty intervals represent the standard deviation of the width distribution. From these values we can estimate also the FTL condition for the processes: for the HGHG is $\sigma_\omega \sigma_t \sim 0.73$, while for SRC is ~ 0.52. For the SRC setup, this means that the main peak is almost at FTL but the contributions coming from the tail can affect the quality of this result. The spectral width observed in HGHG mode implies a FWHM pulse duration of at least 15 fs (at the FTL). This value is smaller than the duration of the measured pulse (22 fs), suggesting the presence of a residual non-linear phase chirp of the seed, that causes a $\sigma_\omega \sigma_t$ farther from the FTL. With the data acquired we can confirm that the main features of the superradiance process has been proofed. We have showed that the scaling laws are followed by the emission process in the last stage, from the simulations for every scaling law and from the energy measurement acquired during the experimental session. We also demonstrated that the time duration in the SRC is shorter, compared to the equivalent setup in HGHG scheme. From the time duration and the spectra acquired we have also proofed that the SRC allows the emission of pulses that are close to the FTL.

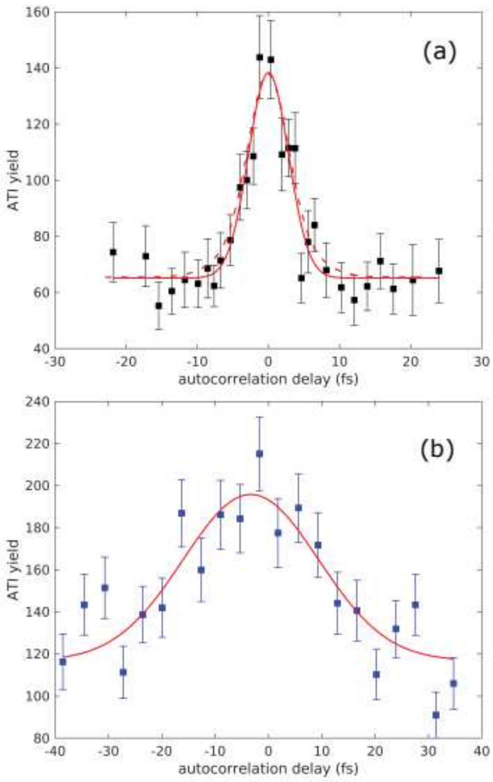

Figure 6.7: Pulse duration. Autocorrelation trace obtained from the Ar 3p ATI yield, with the FEL operating in SR (**a**) mode and HGHG (**b**) mode.

6.3 Frequency Pulling and superradiance

Frequency pulling is a phenomenon commonly observed in conventional lasers. In an atomic laser, the frequency of the laser output is determined by the natural frequency of the atoms in the laser cavity. However, if an external signal is applied to the laser, the frequency of the output can be shifted to match the frequency of the injection signal. This is because the external signal causes the atoms in the laser to oscillate at the frequency of the injection signal, effectively "pulling" the laser frequency to match it. From the theory of conventional lasers, this effect is described by the equation

$$\nu_L = \frac{\nu_0/\Delta\nu_c + \nu_c/\Delta\nu_0}{1/\Delta\nu_0 + 1/\Delta\nu_c}$$

where ν_0 is the center frequency and ν_c is the frequency of the cavity mode (see [94, 95] for a theoretical derivation). A parallel to conventional lasers is possible in a FEL considering the effect of the seed as that of an optical cavity. The FEL gain is indeed centered at some frequency depending on the undulator resonance, the feedback of the optical cavity is instead provided by the pulse seeding the process. By changing the resonance condition, a change in the frequency of the light will occur. [96] have showed how the duality, between the equations of this effect in standard lasers and in FELs, occurs. The result is that the frequency of the emitted light is

$$\nu_{FEL} = \nu_s - (\nu_s - \nu_u)\frac{\sigma_s^2}{\sigma_s^2 + \sigma_u^2}$$

where ν_s is the frequency of the seed laser, ν_u is the central frequency of the radiator gain curve, σ_s and σ_u are the FWHM of the seed and the gain spectra. This effect has been studied experimentally at FERMI in various occasions [96, 97] and lately in superradiant cascade regime [14]. From the relation above, we can see that, if $\sigma_s \ll \sigma_u$ then the frequency shift is really small and the final FEL frequency is principally determined by the seed. If instead $\sigma_s \gg \sigma_u$, the wavelength is shifted towards ν_u: this corresponds to the case of a SASE FEL, where the emission frequency only depends on the resonant condition. In Fig. 6.8 we plotted a simple simulation of the behavior of the frequency pulling: the idea is to move the center of the gain imposed by the resonance condition and to measure the variation of the position of the FEL bandwidth. It is clear that the FEL bandwidth in the spectrum domain is the product of the gain functions of seed and undulators line. Also, if we detune too much the undulators, the two Gaussian functions will become independent and the FEL bandwidth function will be zero.

In HGHG we always observed a weak coupling between the wavelength of the emitted light and wavelength set by the resonance condition of the undulators. Typically a shift of the resonant condition causes a modest frequency shift and mainly affects the FEL intensity. In superradiant regime the opposite has been observed: the coupling is much stronger and the output wavelength is dominated by the undulator resonance. In order to investigate and quantify this

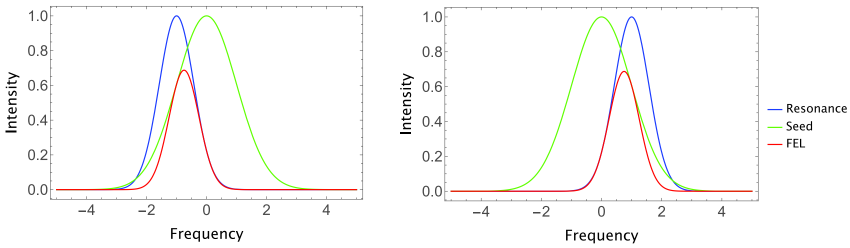

Figure 6.8: Example of the behavior of the frequency pulling: the green curve simulates the spectral bandwidth function of the seed laser, while the blue one indicates the gain generated by the resonance of the undulators line. The product of these two Gaussian functions gives a third Gaussian which describes the spectral bandwidth of the FEL spectrum (red line). Here we used $\mu_s = 0$, $\sigma_s = 3.0$, $\mu_u = 1.0$, $\sigma_u = 1.0$ (units are neglected). By moving the mean value μ_u from 1 to -1, the mean value of the FEL bandwidth is pulled in the same direction.

behavior, we slightly detune the gaps of the last radiators line, to shift the resonant wavelength. This, if the frequency pulling is strong, reflects in a change of the wavelength of the light acquired. We started from the central resonance condition and moved four steps above and below, acquiring 1000 spectra per step. The undulator gap and K-parameter data are converted to relative wavelength detuning $(\lambda_g - \lambda_s)/\lambda_s$, where λ_g is the resonant wavelength imposed by the undulator setting, using the standard magnetic calibration of the FERMI undulators (related to $\nu_u = c/\lambda_g$). For comparison, a similar measurement was carried out later in a typical HGHG mode. Each data point represents a sum of 1000 shots in superradiance mode and 100 shots in HGHG mode.
In Fig. 6.9 we have reported the results from the analysis described above, for SRC (**a**) and for HGHG (**b**) and the linear fitting from the two behaviors (**c**). It is very evident that in SRC the frequency pulling is strong. From the fitting of the central wavelength we obtained a value of

$$\eta = \frac{\sigma_s^2}{\sigma_s^2 + \sigma_u^2} = 0.91 \pm 0.02,$$

From the coefficient η we can estimate the gain bandwidth of the process, knowing the bandwidth of the seed and viceversa. Inverting the relation above, we can estimate the equivalent pulse duration/seed bandwidth that should initiate the amplification process to provide the observed trend of the shift. To match the measured value, we find

$$\sigma_s = \sigma_g \sqrt{\frac{\eta}{1-\eta}} = 4.5 \times 10^{-3}\text{nm},$$

which corresponds to an FTL equivalent rms seed duration $\sigma_t \approx 0.86$ fs. In the superradiant cascade, the final amplifier behaved as if the amplification

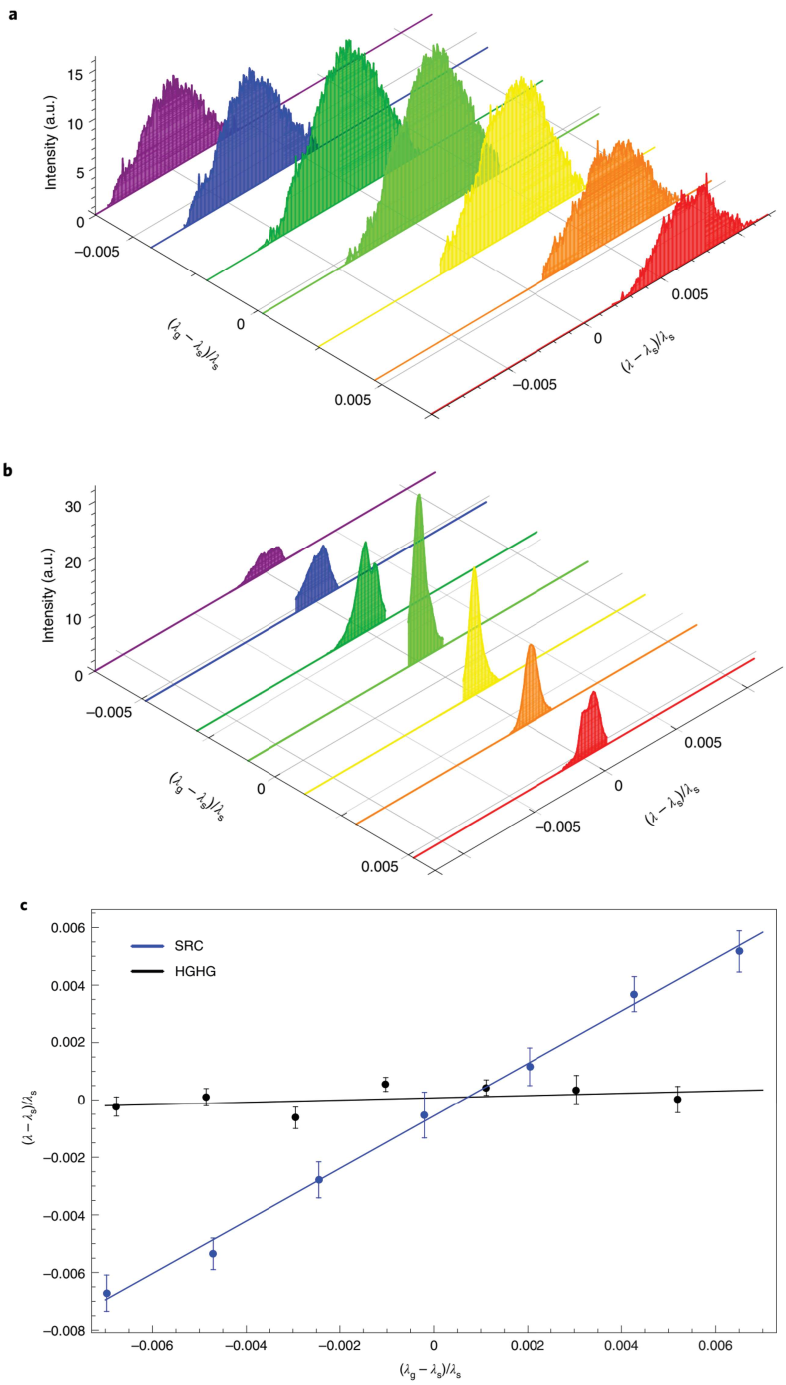

Figure 6.9: **a**, FEL spectra vs the final resonant frequency in SRC. **b**, FEL spectra vs the final resonant frequency in HGHG. **c**, Central emission frequency versus undulator resonant frequency in HGHG (black) and SRC (blue) mode of operation. In all the plots, λ is the wavelength acquired by the spectrometer.

	Bunch Parameters		Undulator Parameters	
Beam Energy (MeV)	900		N. Periods	Periods (cm)
Energy Spread (keV)	150	Modulator	30	10.036
Current (A)	700 – constant prof.	1° stage	42	5.52
Transverse Emit. (mm mrad)	1.2 – 1.2(x - y)	2° stage	42	5.52
Beam Size (μm)	82 – 94 (x - y)	3° stage	62	3.48
	Seed Parameters			
Wavelength (nm)	264			
Peak Power (MW)	200			
Duration FWHM (fs)	55			

Table 6.2: Parameters of the bunch and the undulators line for the simulations.

was initiated by a pulse as short as a single optical cycle of the optical seed, a substantial difference with the behavior of HGHG. For the HGHG case we see that the frequency pulling is very weak, almost negligible (Fig ...). The linear fitting shows that in our case we had $\eta = 0.039 \pm 0.035$, with a fast decay of the intensity while detuning the undulators. This strong difference led to the conclusion that the strong frequency pulling is a main feature of the superradiance process and can be used to characterize the behavior of the FEL in this condition.

6.3.1 Frequency pulling simulations of the superradiant cascade

The superradiant cascade was studied with Genesis 1.3 simulations We run several simulations with GENESIS1.3v4.2, in order to reproduce the machine in the same configuration as described in Tab. 6.2. We wanted to support the experimental results with simulations so we tried to set up the input parameters for mimic the machine the most realistic way. The beam generated was not simulated in a one-for-one condition due to the high computational time and resources. Further, previous simulations showed already a good output with a statistics of 24k macroparticles. Here we decided to use 120k macro particle, to increase the accuracy.

Since, in literature, there are already others experiment done in the HGHG scheme for the frequency pulling effect (ref.), and since our results are in agreement with these other results, we just simulated the SRC condition.

In GENESIS1.3 the linac line is not simulated, but we start directly from the modulator with the insertion of the seed light. Therefore, the bunch has to be generated with the characteristics similar to the real bunch, just before the modulator. The line simulated is the same as in Fig. 6.3, for the SRC scheme. The results of the simulations are in a good agreement with the results obtained in the experimental sessions. The method for simulating the frequency pulling is the same, we have changed the undulators' strength parameter about 0.7% above and below the value reported in Table 6.2, and evaluated the spectrum coming from the superradiant evolution. The simulations confirm the behavior seen during the experimental sessions. The emitted wavelength is follows the

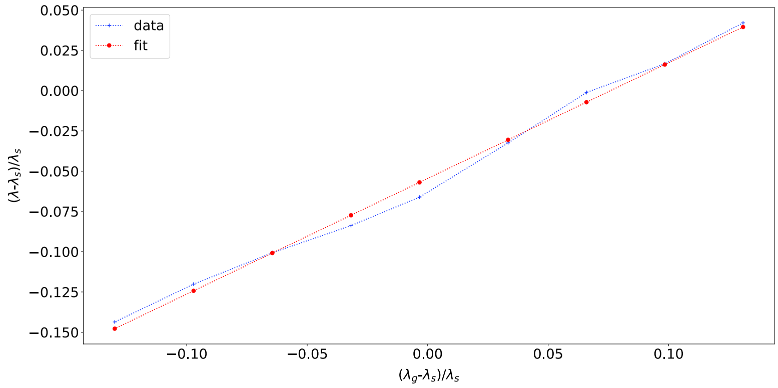

Figure 6.10: Linear fitting of the relative wavelength from the resonance condition $(\lambda_g - \lambda_s)/\lambda_s$ versus the relative wavelength from the light emitted $(\lambda - \lambda_s)/\lambda_s$. This is the equivalent of the plot in Fig. 6.9 (**c**).

change of the resonance condition, almost linearly. The results are reported in Fig. 6.10 and Fig. 6.11. It's interesting to note a small difference in the slope between the experimental data and the correspondent simulated set: the experimental data show a stronger dependence on the resonance condition. The offset that appears in the y-axis is due to the fact that the peak value of the gain of the FEL process is not perfectly centered, but is asymmetric as can be seen from Fig. 3.7, with the respect of the resonance energy.
Still the behavior that results from the simulations confirm the behavior of the machine in the experimental session. The final result is $\eta = 0.718 \pm 0.022$ and despite the fact that is a slightly lower value compared to the experimental results, simulation show a strong relationship between the emitted and the resonant wavelength. From this data we can conclude that also in the computational setup, the strong frequency pulling is a main feature of the SRC scheme. A future development of the simulations can be done by increasing the statistics of the simulated beam, using one-for-one simulations to reduce the noise that appears in the spectra (Fig. 6.11) and to increase the accuracy of the results.

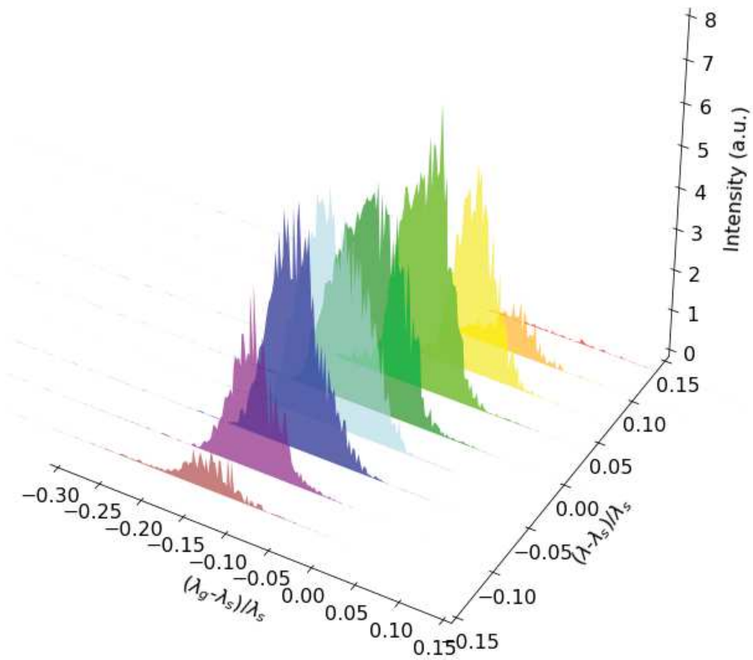

Figure 6.11: 3D plot of the relative wavelength from the resonance condition ($\Delta\lambda_k$) versus the relative wavelength from the light emitted ($\Delta\lambda_l$). This is the equivalent of the plot in Fig. 6.9 (**a**).

6.4 Experimental characterization of superradiant cascade at other output frequencies

The first experiment was carried out at h18 of the seed. Superradiance showed to be a powerful method to produce short pulses in a seeded FEL as FERMI. The possibility to set-up a superradiant cascade at other harmonic multiplication factors is therefore of primary interest to apply this scheme to experiments requiring not only short pulses, but also specific photon energy ranges. For these reasons, in other experimental sessions, the first setup described in Sect.6.2 was repeated and extended to three others harmonic orders: h36, h12 and h24. In order to reach h36 and h24 we have modified the usual SRC configuration, described in Fig. 6.3 (**a**), in such a way that the 3$^{\mathrm{rd}}$stage has been splitted in two stages: the firsts three radiators of the Rd3 were tuned at h18, as the usual setup, but then the last three radiators were tuned at h36, doubling the output frequency. The same was done for h12 and h24. For sake of clarity we will refer to the triple harmonic jump, as in Fig. 6.3, while we will call quadruple harmonic jump the setup to reach h36 and h24, described before. The machine

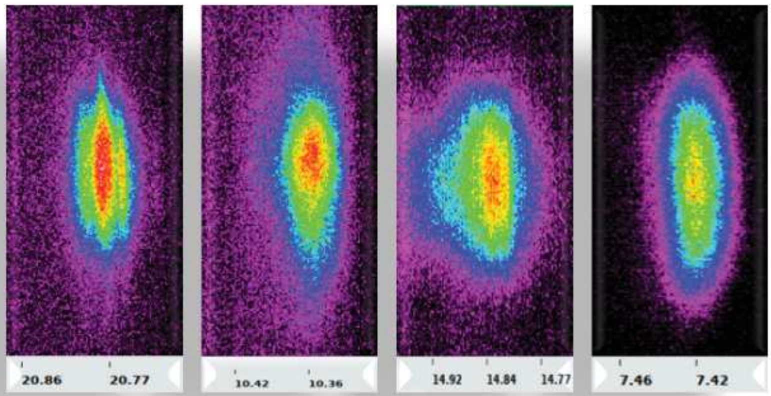

Figure 6.12: Examples of spectra acquired. From left, at h12, h24, h18 and h36. The spectrum at h24 was integrated at 0.1s

Parameter	h12	h24	h18	h36
Spectral Width (nm - FWHM)	0.069 ± 0.003	0.033 ± 0.008	0.076 ± 0.007	0.047 ± 0.008
Pulse Duration (fs - FWHM)	8.98 ± 0.11	4.69 ± 0.15	4.54 ± 0.17	1.7 ± 0.44
Energy per pulse (μJ)	38-40	0.5	16.6	0.1
Final Wavelength (nm)	20.6	10.3	14.67	7.3
Seed Laser (nm)	247.2	247.2	264	264
Frequency Pulling	0.847 ± 0.075	N/A	0.801 ± 0.008	N/A

Table 6.3: Results of the analysis for the four configurations

parameters are close to the ones used the first time, so we can refer to the Table 6.1. The seed laser at h12 and h24 had the wavelength different, at 247.2nm. The procedure of the data acquired is the same, so we are going to report just the results of these four working point.

In Fig. 6.12 and in Tab. 6.3 we have reported the principal results of this experimental session. In Fig. 6.12 are reported the single shot spectra for each configurations. Unfortunately, the h12 and h24 configurations were not very stable: a jitter of the intensity was observed and, for h24, the intensity was low in a way that it was not possible to to acquire single shot spectra. The reported measurements for h24 correspond to an integration up to 0.1s, equivalent to 5 FEL shots per data point. We could observe the increase in the spectral width that characterizes the spectrum of a superradiant FEL pulses. Due to the fact that a superradiant pulse is very close to the FTL condition, if we neglect the contribution coming from the tail, the pulse duration was inferred by the spectral width.

In Table 6.3 are reported the results of the main quantities. Except for h24, the others configuration were rather stable and with an acceptable quality. First, the repeatability of h18 has been confirmed. We recover almost the same values as obtained before. We also characterized the frequency pulling, which resulted to be slightly reduced with respect to first time.
In Fig.6.13 are reported the frequency pulling behavior for h12 and h18. For h12 we observed a plateau-like region in the middle. This behavior can be associated to a not perfect stability of the machine, during the acquisition but a further analysis has to made, in order to confirm this. Despite the fact the frequency pulling values are lower, compared to the first experimental session, its behavior at h18 was surprisingly stable and well aligned. The machine was characterized in three more working points and we also confirmed that in all of these working points we had ultra short pulse durations ($<$ 10fs), with 1.7fs FWHM at h36.

6.5 Superradiance and undulator tapering

Usually, the undulators are tuned through the nominal energy of the beam. Undulators however can be "tapered", i.e. the parameter strength of the undulators can be modified to detune the undulator resonance with respect to its predefined value. Here we report just a computational analysis in order to provide further extension to the experimental sessions carried on previously.
This technique is e.g. implemented to match the shift of the resonant condition due to the energy lost by the electrons during the emission (see for example [98, 99, 100]). During the evolution inside the undulators, the bunch converts part of its energy into radiation. Therefore, in the last undulators, the energy of the bunch is lower, usually a couple of MeV, depending on the nominal energy. It is straightforward to assume, then, that the last undulators are slightly off resonance. By moving the gap, so readjusting the strength parameter, it is possible to compensate the energy lost. This technique has the effect of moving the buckets, inside the longitudinal phase-space, down, if we have moved the gaps in order to lower the resonance energy. A complementary effect can be reached by moving the phaseshifter before entering the undulator ([101] as an example). These devices are the equivalent of one undulator's period and are able to retard the electrons up to one radiation wavelength, with respects to the traveling light. In this way we can move the phase, resulting in a movement towards left or right, of the bucket, inside the phase-space.
To probe this effect we have simulated a tapering condition, in the last undulator's line of FEL-2, both in SRC and HGHG at h18. The simulations were carried out by moving the phaseshifter, before the last undulator, such that the phase changed by 0.2 radiant, from 0 to 2π, and the undulator parameter strength, such that the equivalent resonance energy will be from -5MeV to $+5$MeV, with 0.5MeV steps. In Fig.6.14 are plotted the 2D maps of the situation described. The colors refer to the pulse time duration (rms in fs) in the left plots and the FEL energy pulse in μJ in the right plots. It is interesting to note that, while the energy maps are similar, the pulse durations maps are

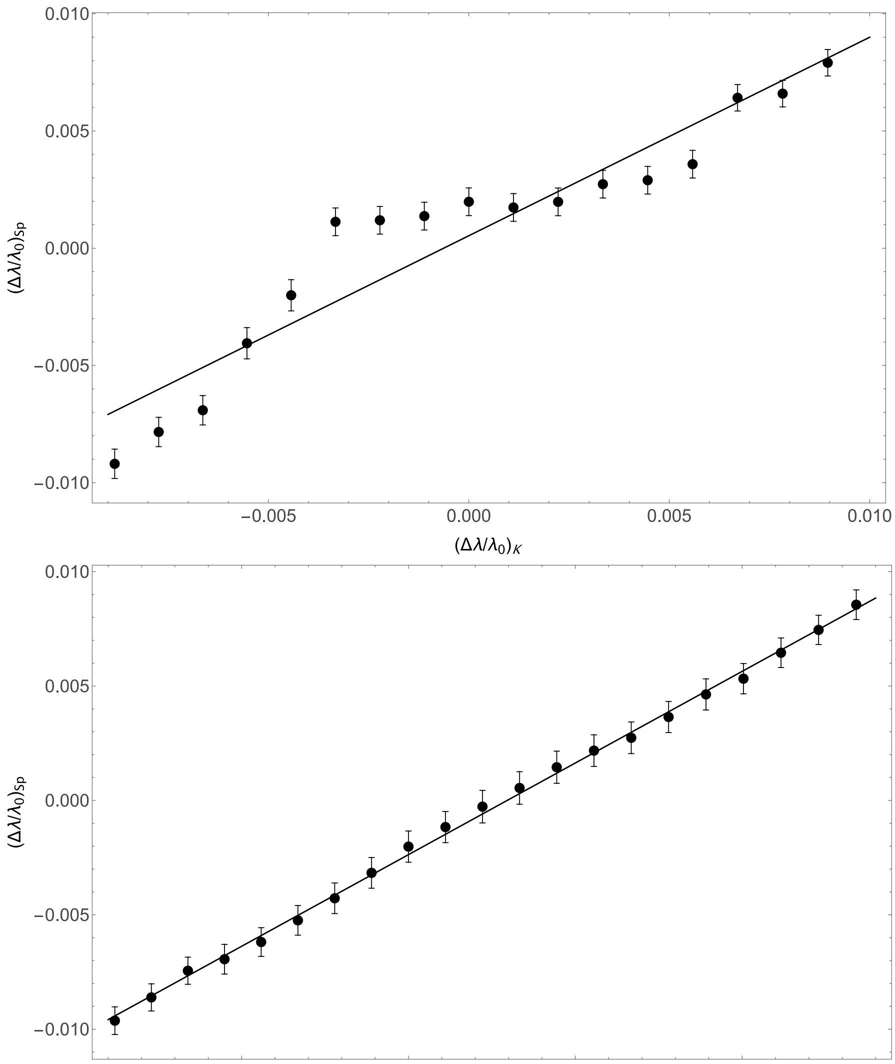

Figure 6.13: Top plot: Frequency pulling plot for h12, as the the relative wavelength from the resonance condition $(\Delta\lambda/\lambda_0)_k$ versus the relative wavelength from the light emitted $(\Delta\lambda/\lambda_0)_{sp}$. Bottom plot: the same for h18.

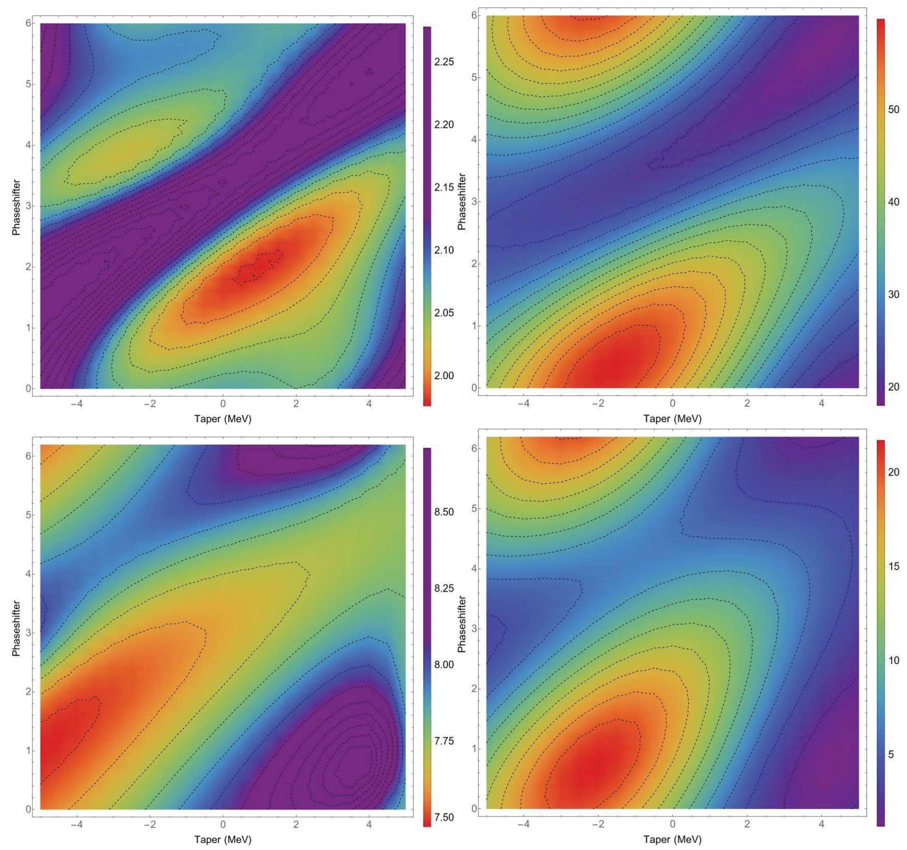

Figure 6.14: 2D maps of the taper equivalent resonance energy vs the shifted phase in the last undulators line. Top plots h18 in SRC. Left: pulse time duration (rms in fs). Right: FEL pulse energy (μJ). Bottom plots h18 in HGHG.

rather different. While the minimum in the SRC is located at positive taper values and a $2\pi/3$ of the nominal phase, the minimum in the HGHG is located at negative value of taper, which is the common situation since the taper is set in order to match the energy loss of the electrons. This is due to the different conformation of the buckets in the phase space. In particular, the fact that the pulse durations have opposite behavior (in HGHG the pulse evolves in order to reach a duration compatible to the cooperation length, while in SRC the pulse length decreases as $z^{-1/2}$), suggests that the phase space has a sort of opposite conformation.

Chapter 7

Scraper

Another method to provide shorter FEL pulse is the scraper technique, as pointed out in Chapter 2. The scraping is a way to reduce the electrons in the whole e-beam, in order to shortening the electron beam length. This is done by inserting two metal blades (the scraper), while the e-beam has a low kinetic energy. These blades spoils the tails of the beam, increasing the emittance in these regions of the bunch. The idea is to preserve intact just the core electrons and the same peak current, to avoid a weakening of the process (the FEL gain is proportional to the peak current).
In Fig.7.1 is reported the scheme of the scraper used at FERMI. The blades (gray rectangles) are placed inside the chicane of BC1, after the tilting of the e-beam by the first couple of dipoles, in order to cut the longitudinal length. Then, the bunch is rotated back by the last couple of dipoles, converting the effect of the scraper form the transverse plane to the longitudinal one.

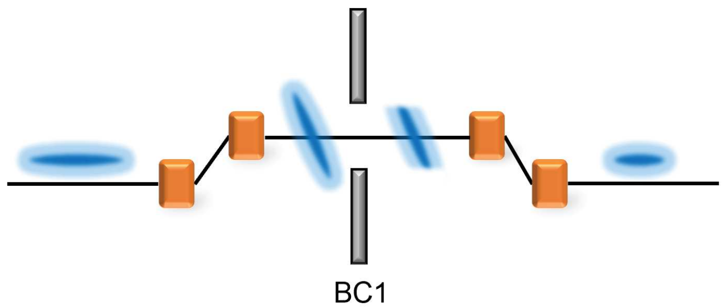

Figure 7.1: Sketch of the setup of the scraper used at FERMI.

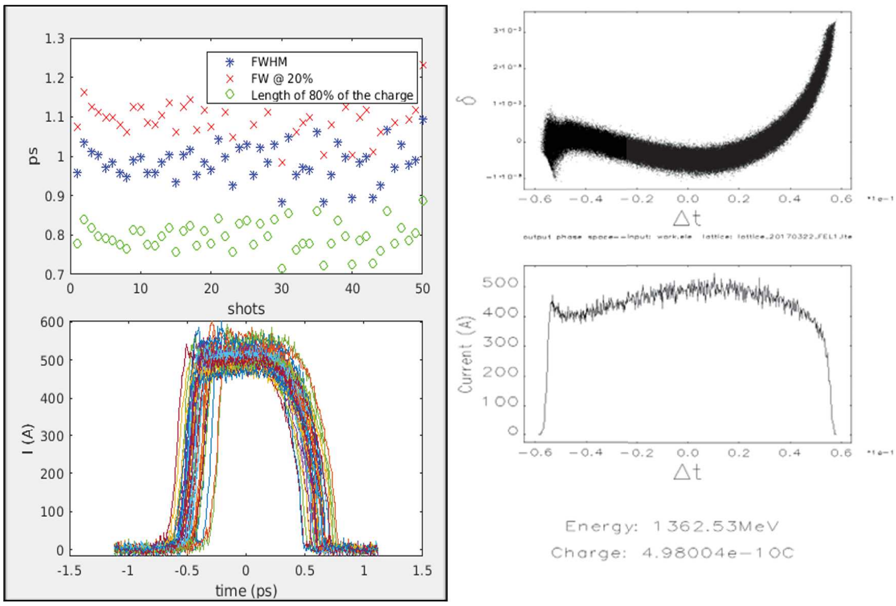

Figure 7.2: Example of longitudinal phase-space, without scraper. Left plots: measured at the end of the LINAC, with current distribution (below) and bunch length measures (above) at FWHM (blue), at 20% of the FW (red) and with 80% of the charge, *i.e.* excluding the tails in the distribution (green). Right plots: simulated in the same condition as in the right, with ELEGANT. Here are reported the longitudinal phase-space (above) and the current profile (below).

The current distribution of the bunches at FERMI is almost flat, but there are some tails, as reported in Fig.7.2. By closing the blades of the scraper, the electrons are removed form the tails and scattered away. In [15], they provided evidences that, while reducing the charge in the beam, the peak current remained constant. If this is true, we can select a specific aperture of the scraper, and therefore a specific length of the bunch, without degrading the gain of the FEL process. In the following we will report the description of the experimental setup and the results.

7.1 Experimental Session

In the first experimental session, we have first searched for proofs that the bunch length lowering is linear with the charge lost. The setup was simple, the scraper is located in BC1, as described before. Since the electrons are scattered by the scraper in this region, the amount of radiations emitted is very high and working continuously with the scraper for hours can be dangerous, especially if the components are not correctly protected against radiations. In order to show the behavior of the scrapered electron beam, we moved the blades, with a selected step, and measured in DBD zone the current profile and the bunch length. The charge was acquired by the charge monitor in the BC1 region, after the scraper. Furthermore, simulations were carried on, using ELEGANT, to compare the results with the real ones and explore the quality of the computational output. The scraper in ELEGANT acts by removing the electrons in the tail, instead of spoiling them, therefore the phase-space right after the scraper appears already cut.

The initial condition of the bunch was 500A of current profile, almost 500pC of electric charge and 1.2ps of bunch length. We proceed to close the blades at 1mm steps, from the open position, until we reached 1mm or so of aperture. Then we changed the step to sample better this narrow region. The results are plotted in Fig. 7.3, in which the top plot is the peak current value and the bottom plot is the behavior of the bunch length as a function of the scraper aperture. We can see that the behavior in the first part (larger aperture) are as expected: while the bunch length is lowering, the current profile is constant and at the nominal value. There are some mismatch in the first points, probably due to some residuals in the tails of the current distribution. The situation is more critical when the blades are narrower, from 1mm to below, because we start to touch the core electrons. While the behavior of the bunch shortening is still linear, there are some strange behaviors in the current profile. We confirmed that the problem was due to the calibration of the deflector: since the bunch length is smaller, it became hard to correctly calibrate the deflector, therefore some systematic errors were introduced. Also the simulated behavior was good enough and reproduced correctly the realistic behavior, with scraper apertures greater than 1mm. The last point acquired was at 0.3mm of aperture, in which we obtained an electron bunch 120fs long, 15 pC of electron charge and it is comparable with the FWHM of the seed usually used. After we confirmed the corrected behavior of the scarpered beam, the main goal is to use this beam to provide FEL emission.

First of all, we have analyzed the FEL emission from the computational point of view. We have selected two positions of the scraper, 0.35mm and 0.1mm. These points were, for us, the more interesting points, due to the fact that at 0.35mm, the bunch length is comparable with the seed duration and 0.1mm is the mechanical limit of the scraper implemented at FERMI. Also, in these points we expect to have troubles with the current peak value, since looking at Fig. 7.3, the calibration of the deflector is problematic and the measures coming from it cannot be trusted.

The simulations are performed by simulating the propagation of the bunch, through the Linac, using ELEGANT and the ouputs has been used as input for GENESIS simulations. For simplicity, we have simulated the FEL-1 line. In Tab. 7.1 are reported the settings of the simulations done.

Before discussing the results, a few words on the input parameters are needed. Despite the fact that we were able to reach a very low value of bunch length, very close to the seed duration, the quality of the beam is not as usual. The high level of scraping has produced a current profile that is Gaussian shaped. Further, the peak current has been heavily degraded because, at this level of bunch length,

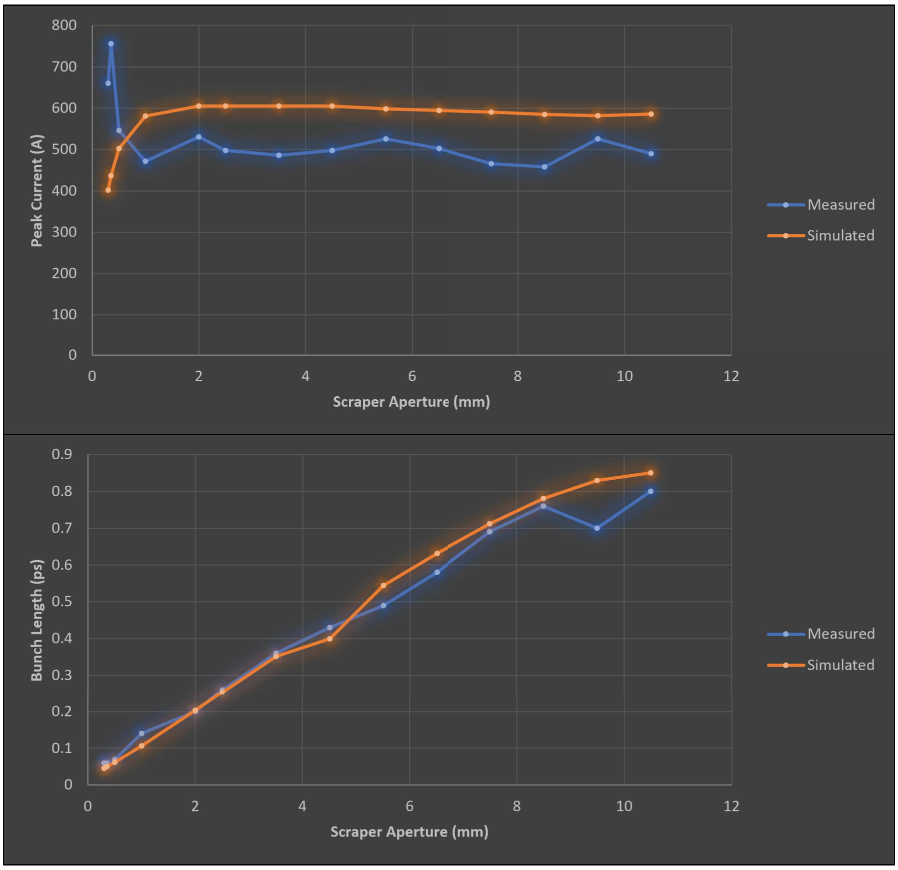

Figure 7.3: Results from the first experiments with the scraper, both measured and simulated. Here we have reported the behavior of the peak current vs the aperture of the scraper (top) and the length of the unspoiled beam vs the aperture of the scraper (bottom).

Beam/seed parameters	Scraper Aperture 0.35mm	Scraper Aperture 0.1mm
Beam energy (MeV)	1363.64	
Beam length (fs)	~120	~80
Peak current (A)	433 (Gaussian)	190 (Gaussian)
Energy spread (keV)	150	117.5
Beam size (μm)	40 x – 30 y (rms)	35 x – 30 y (rms)
Seed wavelength (nm)	255	
Seed peak power (MW)	200	
Seed duration (fs)	55	
Harmonics up-shifts	6	
Undulator parameters		
Undulator	Period (cm)	Periods
MOD1	10.036	30
RAD1	5.52	42

Table 7.1: Parameters of beam and undulators used for the simulation of the FEL emission with a scrapered beam

we have removed a portion of core electrons, losing over 50% of the peak current in the second configuration (0.1mm). In this situation, the emission of FEL light is concentrated where the process is stronger, that is around the current peak. Even if we used a seed longer of the bunch, the principal emission would have been still coming from the core of the bunch. Unfortunately, the current profile cannot be manipulated in order to recover the usual top flat profile made by the linac, therefore it is for us impossible to make the whole bunch emitting with the same intensity. The current profile is the dominating quantity in this setup and the power profile inherit its behavior.
The results obtained for the first case, with the scraper aperture at 0.35mm, are reported in Fig. 7.4. Overall, the FEL emission is quite good. The power profile shows that we obtained a pulse with 23fs, which is less than Eq. 4.5 provides. The spectrum evolution shows some sidebands, but a better optimization of the dispersive section shows the possibility to smooth away those sidebands. The important thing here is to keep a good degree of coherence and spectra quality. The same analysis is true for the simulation at 0.1mm of scraper aperture (Fig. 7.5). The evolution is somewhat chaotic at the beginning, but the final FEL pulse has a good quality. In this case, the output shows a pulse duration of 18fs. Usual pulse duration at FERMI, in a non-scrapered beam, are in the range between 40-45fs. Therefore, we can conclude that this setup can provide shorter pulses. As mentioned before, an higher level of scraping leads to an higher impact in the current profile, at

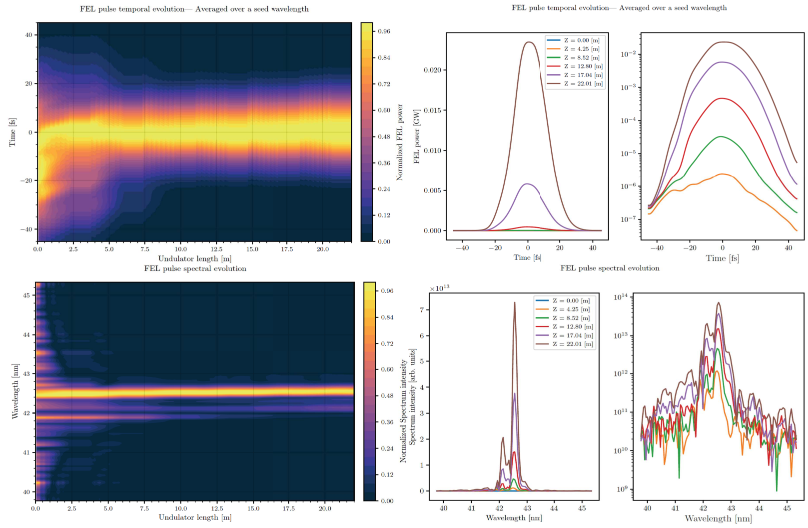

Figure 7.4: Output of the simulation made with the scraper at 0.35mm. Top plots: FEL peak power evolution and profiles. Bottom plots: FEL wavelength evolution and profiles

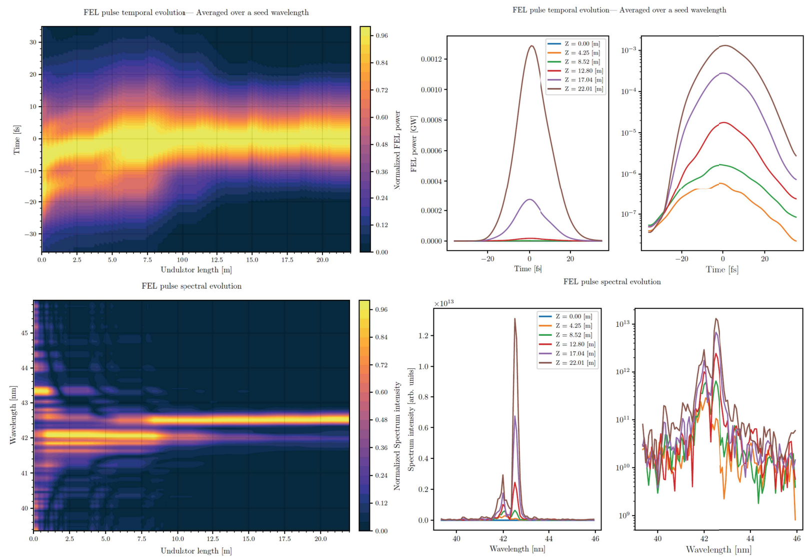

Figure 7.5: Output of the simulation made with the scraper at 0.1mm. Top plots: FEL peak power evolution and profiles. Bottom plots: FEL wavelength evolution and profiles

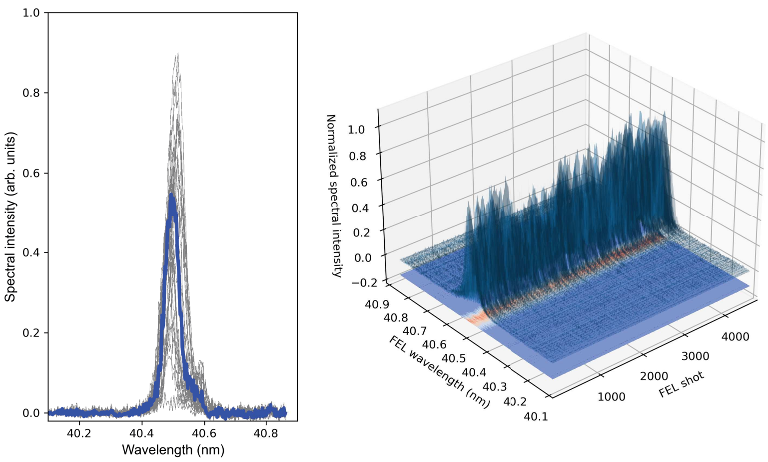

Figure 7.6: FEL spectra at 120pC (0.4mm of aperture). The blue profile on the left is an example of single spectrum inside the collection. We achieved a very good stability, with a 80uJ as mean energy per pulse.

the point that this quantity becomes almost the main variable in the FEL process. After the results of the simulations, we have tried to have machine time for test this configurations and confirm the results. During the first experimental session, we characterized the behavior of the charge and current profile, as a function of the aperture of the scraper (results shown before). We had a second experimental session, with the support of the DiProI beamline, in order to acquire the pulse duration of the FEL light produced with a scrapered beam.
We started the experiment with a scraper aperture of 0.4mm, which corresponded to a 120pC of charge. At this low value of charge the devices had troubles, especially the trajectory devices due to the smaller transverse sizes. Also, a shorter bunch is much more sensible to the time jitter, therefore also the stability was affected. Despite of that, we were able to produce FEL emission and obtained a stable situation with a mean energy per pulse of 80μJ. A series of 1000 spectra was acquired (Fig. 7.6) to provide evidence of the emission and stability of the process. Unfortunately, we weren't able to collect measurement for the pulse duration, for which another experimental session will be needed.

Chapter 8

Final Remarks

This thesis provided an analysis of schemes for the production of ultrashort pulses, focusing on some of the works carried on at FERMI. For the superradiance scheme, we have tested the machine in the SRC, at h18, and characterized the behavior in this point. We obtained a pretty stable spectrum with a $10 - 15\,\mu$J of energy per pulse. We confirmed the superradiant emission by proving that the energy follows the theoretical scaling law. By reproducing the machine condition with the simulations from GENESIS, we proved that also the time durations and the peak power followed the proper scaling laws. From the autocorrelation made of the LDM beamline, we confirmed the shortening of the pulse durations, down to 4.7 fs FWHM. Further, we have shown that in SRC, the FEL pulses are very close to the FTL condition. In the same situation of the machine, we have characterized the frequency pulling, showing that, while in HGHG this effect is very weak, in SRC the movement of the resonance wavelength is followed almost linearly by the FEL wavelength, implying a strong frequency pulling. As a further proofs, we simulated the same experimental session in GENESIS and obtained a similar behavior of the FEL, but with a weaker frequency pulling effect. Then we proceed to have an another experimental session in which we have characterized the machine in a more working points, starting from testing the reproducibility of h18, to other harmonics. Again, we confirmed the frequency pulling and the stability of the machine. This scheme allowed us to reach a pulse shortening of almost 80%, from the standard HGHG scheme.

For the scrapered beam, we were able to confirm the linear behavior between charge left in the bunch and scraper aperture, with an overall constant peak current. Of course, with a very small value of the scraper aperture, the current profile loses it's top flat behavior and the peak value start to decrease, caused by the scarpering of the inner electron in the bunch. We also had a good agreement of the values of charge, peak current and bunch length between the results coming from ELEGANT simulations and from the deflector at the end of the LINAC. The attempt to provide proofs of FEL emission with a shorter bunch was more troublesome, but, first we provided computational evidences that a

scrapered beam delivers shorter FEL pulses, using the results from ELEGANT and using them on GENESIS. Then, we tried to test the results with an experimental session, but we were just able to acquire spectra at a single position of the aperture of the scraper. Nonetheless, we reached a stable condition, both in the spectra quality and in the energy delivered. In this case we have an estimated reduction of the pulse duration of about 60%.
Despite that a scrapered beam cannot reach the levels of the superradiance shortening, still this method is useful for longer wavelength. In fact, it is more difficult to set up a superradiant cascade on FEL-1, due to the lower number of undulators. Superradiance on FEL-1 has been tested by using a double harmonic cascade, instead of the triple one, but the results showed a worse quality of the spectrum. Therefore, it is better to provide shorter pulses on FEL-2 with the superradiant cascade and on FEL-1 with the scraper. To date, instead, a spoiled beam on FEL-2 hasn't been studied yet, providing a way to further expand the studies on short pulses at FERMI. At the end we provided evidences of the generation of short pulses, down to 1.7fs, without impacting on the setup of the machine. As reviewed in Chapter 2, there are possibilities to achieve attosecond durations, but have the negative side that they rely on particular requirements such as specific radiators or specific instruments that need to be implemented on the machine.
Finally, the author (Sottocorona Filippo) wants to thank all the member of FERMI group and Elettra Sincrotrone for this experience, in particular the supervisor Luca Giannessi for all the knowledge and the patience during these three and half years.

Chapter 9

Appendix A - Rational Harmonics

We saw in Chapter 3 how to obtain the spectral brightness of the light produced by an electron moving in a undulated magnetic field. It is interesting to see what happen to this configuration, when we introduce another modulation, with different frequency. In the following calculations we consider an additional modulation coming from an external electromagnetic field (for example a seed laser or a light pulse emitted in a previous stage), coupled to the modulation of the undulator. We start from the definition of the electromagnetic fields,

$$\mathbf{B} = (0, B\sin(k_u z), 0) \quad \text{and} \quad \mathbf{E}_r = (E\cos(k_r z - \omega_r t - \psi_0), 0, 0) \quad \mathbf{B}_r = \frac{1}{c}\left(\mathbf{n} \times \mathbf{E}_r\right),$$

where $k_u$is the period of the undulator and k_r is the period of the modulation coming from the previous stage. From the equation of motion, we have

$$\frac{d\mathbf{p}}{dt} = e_0\left[\mathbf{E}_r + \mathbf{v} \times (\mathbf{B} + \mathbf{B}_r)\right] = m_0 c\gamma\dot{\beta},$$

From now on we consider an observer that lies completely in the z-axis. Therefore the radiation seen by the observer is in the $\mathbf{n} = (0, 0, 1)$ direction. This assumption leads to

$$\beta \times (\mathbf{n} \times \mathbf{E}_r) = \begin{pmatrix} -\beta_z E_x \\ 0 \\ \beta_x E_x \end{pmatrix} \qquad \beta \times c\mathbf{B} = \begin{pmatrix} -\beta_z c B_y \\ 0 \\ \beta_x c B_y \end{pmatrix}$$

and the equation of motion will become

$$\begin{cases} m_0 c\gamma\dot{\beta}_x = e_0\left[(1-\beta_z)E\cos(k_r z - \omega_r t - \psi_0) - \beta_z c B\sin(k_u z)\right], \\ m_0 c\gamma\dot{\beta}_y = 0, \\ m_0 c\gamma\dot{\beta}_z = e_0\left[\beta_x E\cos(k_r z - \omega_r t - \psi_0) + \beta_x c B\sin(k_u z)\right]. \end{cases}$$

We start from solving the first equation in system above. Integrating both sides, we get

$$\beta_x = \beta_{x0} + \frac{e_0}{m_0 c\gamma} \int\limits_0^t \left[(1-\beta_z)E\cos(k_r z - \omega_r t - \psi_0) - \beta_z cB\sin(k_u z)\right] dt.$$

Now, for the first integral we use $dz = c\beta_z dt$. Therefore

$$\beta_x = \beta_{x0} - \frac{e_0}{m_0 c^2\gamma} \int\limits_0^z \beta_z cB\sin(k_u z)\, dz + \frac{e_0 E}{m_0 c\gamma} \int\limits_0^t (1-\beta_z)\cos(k_r c\beta_z t - \omega_r t - \psi_0)\, dt =$$

$$= \beta_{x0} - \frac{e_0 B}{m_0 c\gamma k_u}\left[\cos(k_u z) - 1\right] + \frac{e_0 E}{m_0 c\gamma} \int\limits_0^t (1-\beta_z)\cos\left[k_r c(1-\beta_z)t + \psi_0\right] dt =$$

$$= \beta_{x0} - \frac{e_0 B}{m_0 c^2\gamma k_u}\left[\cos(k_u z) - 1\right] + \frac{e_0 E}{m_0 c\gamma}\frac{1}{k_r c}\left[\sin(k_r c(1-\beta_z)t + \psi_0) - \sin(\psi_0)\right].$$

In the calculations above, we have changed a sign in the last term, using the fact that the cosine is an even function. We define $K_m = e_0 B/(m_0 c k_u)$, the dual one for the electric component $K_e = e_0 E/\left[m_0 c^2 k_r\right]$ and $k_n = k_r(1-\beta_z)$. We have therefore $k_n z = k_r c\beta_z t - \omega_r t$.
Furthermore, by choosing the integration constant $\beta_{x0} = -K_m/\gamma + K_e\sin(\psi_0)/\gamma$ and we get

$$\beta_x = -\frac{K_m}{\gamma}\cos(k_u z) + \frac{K_e}{\gamma}\sin(k_n z + \psi_0).$$

With the traverse velocity, we can now compute the longitudinal velocity. Using the relation

$$\beta^2 = 1 - \frac{1}{\gamma^2} = \beta_x^2 + \beta_z^2 \qquad \Rightarrow \qquad \beta_z^2 = 1 - \frac{1}{\gamma^2} - \beta_x^2,$$

and substituting the horizontal velocity β_x in the above expression we have

$$\beta_z^2 = 1 - \frac{1}{\gamma^2} - \frac{K_m^2}{\gamma^2}\cos^2(k_u z) + \frac{2K_m K_e}{\gamma^2}\cos(k_u z)\sin(k_n z + \psi_0) - \frac{K_e^2}{\gamma^2}\sin^2(k_n z + \psi_0).$$

In order to simplify the expression above, we use the fact that

$$\cos^2(k_u z) = \frac{1+\cos(2k_u z)}{2} \text{ and } \sin^2(k_n z + \psi_0) = \frac{1-\cos\left[2(k_n z + \psi_0)\right]}{2}$$

and the expansion of the square root at the second order in γ. Therefore,

$$\beta_z = 1 - \frac{1}{2\gamma^2} - \frac{K_m^2}{2\gamma^2}\frac{1+\cos(2k_u z)}{2} + \frac{K_m K_e}{\gamma^2}\cos(k_u z)\sin(k_n z + \psi_0) +$$

$$-\frac{K_e^2}{2\gamma^2}\frac{1-\cos\left[2\left(k_n z+\psi_0\right)\right]}{2}$$

Now, reorganizing the terms in a more useful way, we have

$$\beta_z = 1 - \frac{1}{2\gamma^2}\left(1 + \frac{K_m^2 + K_e^2}{2}\right) - \frac{K_m^2}{4\gamma^2}\cos(2k_u z) +$$

$$+\frac{K_m K_e}{\gamma^2}\cos(k_u z)\sin(k_n z + \psi_0) - \frac{K_e^2}{4\gamma^2}\cos\left[2\left(k_n z+\psi_0\right)\right]$$

It is useful to define

$$\bar{\beta_z} = 1 - \frac{1}{2\gamma^2}\left(1 + \frac{K_m^2 + K_e^2}{2}\right)$$

Now we need to find the longitudinal trajectory, therefore we have to integrate the longitudinal velocity obtained. So

$$z(t) = \int_0^t c\beta_z dt = c\bar{\beta_z}t - \frac{K_m^2}{4\gamma^2}\int_0^t \cos(2k_u c\bar{\beta_z}t)dt +$$

$$+\frac{K_m K_e}{\gamma^2}\int_0^t \cos(k_u c\bar{\beta_z}t)\sin(k_n c\bar{\beta_z}t + \psi_0)dt - \frac{K_e^2}{4\gamma^2}\int_0^t \cos\left[2\left(k_n c\bar{\beta_z}t+\psi_0\right)\right]$$

For clarity, we're going to evaluate each integral separately

$$\int_0^t \cos(2k_u c\bar{\beta_z}t)dt = \frac{1}{2k_u c\bar{\beta_z}}\sin\left(2k_u c\bar{\beta_z}t\right)$$

$$\int_0^t \cos(k_u c\bar{\beta_z}t)\sin(k_n c\bar{\beta_z}t + \psi_0)dt =$$

$$= \frac{1}{2}\int_0^t \sin\left[\left(k_u+k_n\right)\bar{\beta_z}ct + \psi_0\right]dt - \frac{1}{2}\int_0^t \sin\left[\left(k_u-k_n\right)\bar{\beta_z}ct - \psi_0\right]dt =$$

$$= \frac{\left[\cos\left(\psi_0\right) - \cos\left[\left(k_u+k_n\right)\bar{\beta_z}ct+\psi_0\right]\right]}{2\left[\left(k_u+k_n\right)\bar{\beta_z}c\right]} - \frac{\left[\cos\left(\psi_0\right) - \cos\left[\left(k_u-k_n\right)\bar{\beta_z}ct+\psi_0\right]\right]}{2\left[\left(k_u-k_n\right)\bar{\beta_z}c\right]}$$

$$\int_0^t \cos\left[2\left(k_n c\bar{\beta_z}t+\psi_0\right)\right] = \frac{1}{2k_n c\bar{\beta_z}}\left[\sin\left[2\left(k_n c\bar{\beta_z}t+\psi_0\right)\right] - \sin\left(2\psi_0\right)\right]$$

And putting all together we get

$$z(t) = c\bar{\beta}_z t - \frac{K_m^2}{4\gamma^2}\frac{1}{2k_u c\bar{\beta}_z}\sin\left(2k_u c\bar{\beta}_z t\right) +$$

$$+\frac{K_m K_e}{\gamma^2}\left\{\frac{\left[\cos\left(\psi_0\right) - \cos\left[\left(k_u + k_n\right)\bar{\beta}_z ct + \psi_0\right]\right]}{2\left[\left(k_u + k_n\right)\bar{\beta}_z c\right]} - \frac{\left[\cos\left(\psi_0\right) - \cos\left[\left(k_u - k_n\right)\bar{\beta}_z ct + \psi_0\right]\right]}{2\left[\left(k_u - k_n\right)\bar{\beta}_z c\right]}\right\} +$$

$$-\frac{K_e^2}{4\gamma^2}\frac{1}{2k_n c\bar{\beta}_z}\left[\sin\left[2\left(k_n c\bar{\beta}_z t + \psi_0\right)\right] - \sin\left(2\psi_0\right)\right].$$

In order to simplify from now on we can neglect, in $\beta_z$and $z(t)$, all the terms in K_e. Now that we have the dynamical quantities, we can compute the spectral brightness

$$\frac{d^2 I\left(\omega\right)}{d\omega d\Omega} = \frac{e_0^2\omega^2}{4\pi^2 c}\left|\int_0^{L_u/c\bar{\beta}_z} e^{i\omega\left(t_{ret} - \mathbf{r}\left(t_{ret}\right)\cdot\mathbf{n}/c\right)}\left[\mathbf{n}\times\left(\mathbf{n}\times\beta\right)\right]_{ret} dt_{ret}\right|^2$$

Since we are looking for axial components, $\mathbf{n} = (0,0,1)$. In this way the triple cross product is equal to $-\beta_x$ and the exponential becomes

$$t_{ret} - \mathbf{r}\left(t_{ret}\right)\cdot\mathbf{n}/c = t_{ret} - z(t_{ret})/c = t_{ret}\left(1 - \bar{\beta}_z\right) + \frac{K_m^2}{8\gamma^2}\frac{1}{ck_u}\sin\left(2k_u ct_{ret}\right)$$

Focusing just on the integral and putting everything together, we get

$$\int_0^{L_u/c\bar{\beta}_z} e^{i\omega\left[t_{ret}\left(1-\bar{\beta}_z\right) + \frac{K_m^2}{8\gamma^2}\frac{1}{ck_u}\sin\left(2k_u ct_{ret}\right)\right]}\left\{\frac{K_m}{\gamma}\cos(k_u c\bar{\beta}_z t_{ret}) + \frac{K_e}{\gamma}\sin(k_n c\bar{\beta}_z t_{ret} + \psi_0)\right\} dt_{ret}$$

The first integral is well known and we have already deal with it in the Chapter 2 . We will compute just the lasts two. Therefore

$$\frac{K_e}{\gamma}\int_0^{L_u/c\bar{\beta}_z} e^{i\omega\left[t_{ret}\left(1-\bar{\beta}_z\right) + \frac{K_m^2}{8\gamma^2}\frac{1}{ck_u}\sin\left(2k_u ct_{ret}\right)\right]}\left[\frac{e^{i\left(k_n c\bar{\beta}_z t_{ret} + \psi_0\right)} - e^{-i\left(k_n c\bar{\beta}_z t_{ret} + \psi_0\right)}}{2i}\right] dt_{ret}$$

In order to take care of the sine in the exponential, we use the Jacobi–Anger expansion in Bessel terms

$$e^{i\chi\sin(\psi)} = \sum_{m=-\infty}^{+\infty} J_m\left(\chi\right) e^{im\psi} \quad\Rightarrow\quad e^{i\frac{\omega}{\omega_u}\frac{K_m^2}{8\gamma^2}\sin\left(2k_u ct_{ret}\right)} = \sum_{m=-\infty}^{+\infty} J_m\left(\frac{\omega}{\omega_u}\frac{K_m^2}{8\gamma^2}\right) e^{i2m\omega_u t_{ret}}$$

In this way the integrals above become

$$\frac{K_e}{2i\gamma}\sum_{m=-\infty}^{+\infty} J_m\left(\frac{\omega}{\omega_u}\frac{K_m^2}{8\gamma^2}\right)\left\{e^{i\psi_0}\int_0^{L_u/c\bar{\beta}_z} e^{it_{ret}\left[\omega\left(1-\bar{\beta}_z\right)+2m\omega_u+k_n c\bar{\beta}_z\right]}\right.$$
$$\left.-e^{-i\psi_0}\int_0^{L_u/c\bar{\beta}_z} e^{it_{ret}\left[\omega\left(1-\bar{\beta}_z\right)+2m\omega_u-k_n c\bar{\beta}_z\right]}\right\}$$

In order to simplify the quantity above we can assume that $\bar{\beta}_z \sim 1$, we define $\omega_r = k_r c$ and evaluate the quantities in the argument of the Bessel functions as $\chi = K_m^2/(4+2K_m^2)$, using the resonance condition and we relabel the series index as $u = 2m$. With these, the integrals above become

$$\frac{K_e}{2i\gamma}\sum_{m=-\infty}^{+\infty} J_m(\chi)\left\{e^{i\psi_0}\int_0^{L_u/c\bar{\beta}_z} e^{it_{ret}\left[\omega\left(1-\bar{\beta}_z\right)+u\omega_u+\omega_n\right]} - e^{-i\psi_0}\int_0^{L_u/c\bar{\beta}_z} e^{it_{ret}\left[\omega\left(1-\bar{\beta}_z\right)+u\omega_u-\omega_n\right]}\right\} =$$

$$= \frac{K_e}{2i\gamma}\frac{L_u}{c}\sum_{u=-\infty}^{+\infty} J_{\frac{u}{2}}(\chi)\left\{e^{i\psi_0}e^{i\frac{L_u}{2c}\left\{\omega\left(1-\bar{\beta}_z\right)+u\omega_u+\omega_n\right\}}\text{sinc}\left[\frac{L_u}{2c}\left\{\omega\left(1-\bar{\beta}_z\right)+u\omega_u+\omega_n\right\}\right]\right\}+$$

$$-\frac{K_e}{2i\gamma}\frac{L_u}{c}\sum_{u=-\infty}^{+\infty} J_{\frac{u}{2}}(\chi)\left\{e^{-i\psi_0}e^{i\frac{L_u}{2c}\left\{\omega\left(1-\bar{\beta}_z\right)+u\omega_u-\omega_n\right\}}\text{sinc}\left[\frac{L_u}{2c}\left\{\omega\left(1-\bar{\beta}_z\right)+u\omega_u-\omega_n\right\}\right]\right\}$$

Finally, put every pieces back together, the spectral brightness will be

$$\frac{d^2I(\omega)}{d\omega d\Omega} = \frac{e_0^2\omega^2L_u^2}{16\pi^2c^3\gamma^2}\left|K_m\sum_{u=-\infty}^{+\infty}\left[J_{\frac{u}{2}+1}(\chi)+J_{\frac{u}{2}-1}(\chi)\right]e^{i\frac{L_u}{2c}\left\{\omega\left(1-\bar{\beta}_z\right)+u\omega_u\right\}}\text{sinc}\left[\frac{L_u}{2c}\left\{\omega\left(1-\bar{\beta}_z\right)+u\omega_u\right\}\right]+\right.$$

$$-iK_e\sum_{u=-\infty}^{+\infty} J_{\frac{u}{2}}(\chi)\left\{e^{i\frac{L_u}{2c}\left\{\omega\left(1-\bar{\beta}_z\right)+u\omega_u+\omega_n\right\}+i\psi_0}\text{sinc}\left[\frac{L_u}{2c}\left\{\omega\left(1-\bar{\beta}_z\right)+u\omega_u+\omega_n\right\}\right]\right\}+$$

$$\left.+iK_e\sum_{u=-\infty}^{+\infty} J_{\frac{u}{2}}(\chi)\left\{e^{-i\frac{L_u}{2c}\left\{\omega\left(1-\bar{\beta}_z\right)+u\omega_u-\omega_n\right\}-i\psi_0}\text{sinc}\left[\frac{L_u}{2c}\left\{\omega\left(1-\bar{\beta}_z\right)+u\omega_u-\omega_n\right\}\right]\right\}\right|^2$$

Now, looking at the arguments of the Bessel, for the ones that are associated with K_m, we can rewrite them as

$$\frac{L_u}{2c}\left\{\omega\left(1-\bar{\beta}_z\right)+u\omega_u\right\} = \frac{N\lambda_u\omega_u}{2c}\left[\frac{\omega}{\omega_u}\frac{2\gamma^2}{(1+K_m^2/2)}+u\right] = N\pi\left(\frac{\omega}{\omega_0}+u\right)$$

In the same way, and using that $\omega_r = \omega_0/n$, with n as the harmonic number, we can analyze arguments of the Bessel, for the ones that are associated with K_e, therefore

$$\frac{L_u}{2c}\left\{\omega\left(1-\bar{\beta}_z\right)+u\omega_u\pm\omega_r\right\}=\frac{N\lambda_u\omega_u}{2c}\left[\frac{\omega}{\omega_u}\frac{2\gamma^2}{(1+K_m^2/2)}+u\pm\frac{\omega_r}{\omega_u}\right]=N\pi\left(\frac{\omega}{\omega_0}+u\pm\frac{1}{ng}\right)$$

with $1/g = 2\gamma^2/\left(1+K_m^2/2\right)$. From this relation we can see that the resonant peak in the brightness is no more centered at integer harmonics of the central frequency ω_0. The term $1/g$ is dominated by γ^2 which is of the order of 10^6, therefore we can no longer have a condition on u such that the argument of the *sinc* is equal to zero. To be precise there's a condition on u, but since we have to balance a term of 10^6 this would require an harmonic number of a million, which is impossible. This leads to the conclusion that the contribution of the external field, with the assumption of dropping all the terms in K_e in the velocity and trajectory, is canceled by an impossible condition on u. Using instead all the terms in the longitudinal velocity and trajectory, excluding just the non oscillating components, we want to see how the spectral brightness will change. Therefore we restart from

$$\int_0^{L_u/c} e^{i\left[\omega t_{ret}\left(1-\bar{\beta}_z\right)+\frac{\omega K_m^2\sin(2\omega_u t_{ret})}{8\gamma^2\omega_u}-\frac{\omega K_m K_e}{2\gamma^2}\left\{\frac{\cos[(\omega_u+\omega_n)t_{ret}+\psi_0]}{\omega_u+\omega_n}-\frac{\cos[(\omega_u-\omega_n)t_{ret}+\psi_0]}{\omega_u-\omega_n}\right\}-\frac{\omega K_e^2}{4\gamma^2}\frac{\sin[2(\omega_n t_{ret}+\psi_0)]}{2\omega_n}\right]}$$

$$\left\{\frac{K_m}{\gamma}\cos(\omega_n t_{ret})-\frac{K_e}{\gamma}\sin(\omega_n t_{ret}+\psi_0)\right\}dt_{ret}$$

in which we have already assumed that $\bar{\beta_z}\sim 1$, $\omega_u = k_u c$ and $\omega_n = k_n c$. We now expand all the oscillating functions in the exponential with

$$e^{i\chi\sin(\psi)}=\sum_{m=-\infty}^{+\infty}J_m\left(\chi\right)e^{im\psi}\quad\text{and}\quad e^{i\chi\cos(\psi)}=\sum_{m=-\infty}^{+\infty}i^m J_m\left(\chi\right)e^{im\psi}$$

and focusing on just the exponential term, it becomes

$$\sum_{\mu=-\infty}^{+\infty}\sum_{\nu=-\infty}^{+\infty}\sum_{\rho=-\infty}^{+\infty}\sum_{\sigma=-\infty}^{+\infty}J_\sigma\left(-\frac{\omega K_e^2}{8\gamma^2\omega_n}\right)J_\rho\left(\frac{\omega K_m K_e}{2\gamma^2\left(\omega_u-\omega_n\right)}\right)J_\nu\left(-\frac{\omega K_m K_e}{2\gamma^2\left(\omega_u+\omega_n\right)}\right)J_\mu\left(\frac{K_m^2\omega}{8\gamma^2\omega_u}\right)\times$$

$$\times e^{2i\sigma(\omega_n t_{ret}+\psi_0)+\rho\left[(\omega_u-\omega_n)t_{ret}+\tilde{\psi}_0\right]+\nu\left[(\omega_u+\omega_n)t_{ret}+\tilde{\psi}_0\right]+2\mu\omega_u t_{ret}+\omega\left[t_{ret}\left(1-\bar{\beta}_z\right)\right]}$$

Dropping the Bessel's arguments and evaluating the integrals, we have

$$\sum_{\mu,\nu,\rho,\sigma}J_\sigma J_\rho J_\nu J_\mu e^{i(2\sigma+\rho+\nu)\psi_0}\int_0^{L_u/c}e^{it_{ret}\left[(\rho+\nu+2\mu)\omega_u+(2\sigma-\rho+\nu)\omega_n+\omega\left(1-\bar{\beta}_z\right)\right]}\times$$

$$\times \left[\frac{K_m}{2\gamma} \left(e^{i\omega_u t_{ret}} + e^{-i\omega_u t_{ret}} \right) \right] dt_{ret} =$$

$$= \frac{K_m}{2\gamma} \sum_{\mu,\nu,\rho,\sigma} J_\sigma J_\rho J_\nu J_\mu e^{i(2\sigma+\rho+\nu)\psi_0} e^{i(\rho+\nu)\pi/2} \times$$

$$\left[\int_0^{L_u/c} e^{it_{ret}\left[(\rho+\nu+2\mu+1)\omega_u+(2\sigma-\rho+\nu)\omega_n+\omega\left(1-\bar{\beta}_z\right)\right]} dt_{ret} + \right.$$

$$\left. + \int_0^{L_u/c} e^{it_{ret}\left[(\rho+\nu+2\mu-1)\omega_u+(2\sigma-\rho+\nu)\omega_n+\omega\left(1-\bar{\beta}_z\right)\right]} dt_{ret} \right] = \frac{K_m L_u}{4\gamma c} \sum_{\mu,\nu,\rho,\sigma} J_\sigma J_\rho J_\nu J_\mu \times$$

$$\times e^{i(2\sigma+\rho+\nu)\psi_0} e^{i(\rho+\nu)\pi/2} \left\{ e^{i\frac{L_u}{2c}\left[(\rho+\nu+2\mu+1)\omega_u+(2\sigma-\rho+\nu)\omega_n+\omega\left(1-\bar{\beta}_z\right)\right]} \times \right.$$

$$\times \mathrm{sinc} \left\{ \frac{L_u}{2c} \left[(\rho+\nu+2\mu+1)\,\omega_u + (2\sigma-\rho+\nu)\,\omega_n + \omega\left(1-\bar{\beta}_z\right) \right] \right\} +$$

$$+ e^{i\frac{L_u}{2c}\left[(\rho+\nu+2\mu-1)\omega_u+(2\sigma-\rho+\nu)\omega_n+\omega\left(1-\bar{\beta}_z\right)\right]} \times$$

$$\left. \times \mathrm{sinc} \left\{ \frac{L_u}{2c} \left[(\rho+\nu+2\mu-1)\,\omega_u + (2\sigma-\rho+\nu)\,\omega_n + \omega\left(1-\bar{\beta}_z\right) \right] \right\} \right\}$$

Now we can rename the indices as

$$\begin{cases} \rho+\nu+2\mu+1 = a \\ 2\sigma-\rho+\nu = b \\ 2\sigma+\rho+\nu = d \\ \rho+\nu = 2e \end{cases} \quad \Rightarrow \quad \begin{cases} \mu = \frac{a-1}{2} - e \\ \nu = 2e - \frac{d-b}{2} \\ \rho = \frac{d-b}{2} \\ \sigma = \frac{d-2e}{2} \end{cases}$$

$$= \frac{K_m L_u}{4\gamma c} \sum_{a,b,d,e} \left(J_{\frac{d-2e}{2}} J_{\frac{d-b}{2}} J_{2e-\frac{d-b}{2}} J_{\frac{a-1}{2}-e} + J_{\frac{d-2e}{2}} J_{\frac{d-b}{2}} J_{2e-\frac{d-b}{2}} J_{\frac{a+1}{2}-e} \right) e^{ie\pi} e^{id\psi_0}$$

$$\left\{ e^{i\frac{L_u}{2c}\left[a\omega_u+b\omega_n+\omega\left(1-\bar{\beta}_z\right)\right]} \mathrm{sinc} \left\{ \frac{L_u}{2c} \left[a\omega_u + b\omega_n + \omega\left(1-\bar{\beta}_z\right) \right] \right\} \right\}$$

Integrating the other function, the electric sine

$$\sum_{\mu,\nu,\rho,\sigma} J_\sigma J_\rho J_\nu J_\mu e^{i(2\sigma+\rho+\nu)\psi_0} e^{i(\rho+\nu)\pi/2} \int_0^{L_u/c} e^{it_{ret}\left[(\rho+\nu+2\mu)\omega_u+(2\sigma-\rho+\nu)\omega_n+\omega\left(1-\bar{\beta}_z\right)\right]} \times$$

$$\times \left[\frac{K_e}{2i\gamma} \left(e^{i\omega_n t_{ret}} - e^{-i\omega_n t_{ret}} \right) \right] dt_{ret} =$$

$$= \frac{K_e}{2i\gamma} \sum_{\mu,\nu,\rho,\sigma} J_\sigma J_\rho J_\nu J_\mu e^{i(2\sigma+\rho+\nu)\psi_0} e^{i(\rho+\nu)\pi/2} \left[\int_0^{L_u/c} e^{it_{ret}\left[(\rho+\nu+2\mu)\omega_u+(2\sigma-\rho+\nu+1)\omega_n+\omega\left(1-\bar{\beta}_z\right)\right]} dt_{ret} + \right.$$

$$\left. - \int_0^{L_u/c} e^{it_{ret}\left[(\rho+\nu+2\mu)\omega_u+(2\sigma-\rho+\nu-1)\omega_n+\omega\left(1-\bar{\beta}_z\right)\right]} dt_{ret} \right] =$$

$$= \frac{K_e L_u}{4i\gamma c} \sum_{\mu,\nu,\rho,\sigma} J_\sigma J_\rho J_\nu J_\mu$$

$$e^{i(2\sigma+\rho+\nu)\psi_0} e^{i(\rho+\nu)\pi/2} \left\{ e^{i\frac{L_u}{2c}\left[(\rho+\nu+2\mu)\omega_u+(2\sigma-\rho+\nu+1)\omega_n+\omega\left(1-\bar{\beta}_z\right)\right]} \times \right.$$

$$\times \mathrm{sinc} \left\{ \frac{L_u}{2c} \left[(\rho+\nu+2\mu)\,\omega_u + (2\sigma-\rho+\nu+1)\,\omega_n + \omega\left(1-\bar{\beta}_z\right) \right] \right\} +$$

$$- e^{i\frac{L_u}{2c}\left[(\rho+\nu+2\mu)\omega_u+(2\sigma-\rho+\nu-1)\omega_n+\omega\left(1-\bar{\beta}_z\right)\right]} \times$$

$$\left. \times \mathrm{sinc} \left\{ \frac{L_u}{2c} \left[(\rho+\nu+2\mu)\,\omega_u + (2\sigma-\rho+\nu-1)\,\omega_n + \omega\left(1-\bar{\beta}_z\right) \right] \right\} \right\}$$

Now we rename the indexes as

$$\begin{cases} \rho+\nu+2\mu = a \\ 2\sigma-\rho+\nu+1 = b \\ 2\sigma+\rho+\nu = d \\ \rho+\nu = 2e \end{cases} \Rightarrow \begin{cases} \mu = \frac{a}{2} - e \\ \nu = 2e - \frac{d-b+1}{2} \\ \rho = \frac{d-b+1}{2} \\ \sigma = \frac{d-2e}{2} \end{cases}$$

$$= \frac{K_e L_u}{4i\gamma c} \sum_{a,b,d,e} \left(J_{\frac{d-2e}{2}} J_{\frac{d-b+1}{2}} J_{2e-\frac{d-b+1}{2}} J_{\frac{a}{2}-e} - J_{\frac{d-2e}{2}} J_{\frac{d-b-1}{2}} J_{2e-\frac{d-b-1}{2}} J_{\frac{a}{2}-e} \right) e^{ie\pi} e^{id\psi_0}$$

$$\left\{ e^{i\frac{L_u}{2c}\left[a\omega_u+b\omega_n+\omega\left(1-\bar{\beta}_z\right)\right]} \mathrm{sinc} \left\{ \frac{L_u}{2c} \left[a\omega_u + b\omega_n + \omega\left(1-\bar{\beta}_z\right) \right] \right\} \right\}$$

Finally we define

$$\chi_e = \frac{\omega K_e^2}{8\gamma^2 \omega_n}$$

$$\chi_{em}^{\pm} = \frac{\omega K_m K_e}{2\gamma^2 \left(\omega_u \pm \omega_n\right)}$$

$$\chi_m = \frac{K_m^2 \omega}{8\gamma^2 \omega_u}$$

, putting everything together

$$\frac{d^2 I(\omega)}{d\omega d\Omega} = \frac{e_0^2 \omega^2 L_u^2}{16\pi^2 c^3 \gamma^2} \Bigg| \sum_{a,b,d,e}$$

$$\Big\langle \Big[K_m J_{\frac{d-2e}{2}} (-\chi_e) J_{\frac{d-b}{2}} \left(\chi_{em}^-\right) J_{2e-\frac{d-b}{2}} \left(-\chi_{em}^+\right) \times \Big[J_{\frac{a-1}{2}-e} (\chi_m) + J_{\frac{a+1}{2}-e} (\chi_m) \Big] +$$

$$+ i K_e J_{\frac{d-2e}{2}} (-\chi_e) J_{\frac{a}{2}-e} (\chi_m)$$

$$\times \Big[J_{\frac{d-b+1}{2}} \left(\chi_{em}^-\right) J_{2e-\frac{d-b+1}{2}} \left(-\chi_{em}^+\right) - J_{\frac{d-b-1}{2}} \left(\chi_{em}^-\right) J_{2e-\frac{d-b-1}{2}} \left(-\chi_{em}^+\right) \Big] \Big] \times$$

$$\times e^{ie\pi} e^{id\psi_0} e^{i\frac{L_u}{2c}\left[\pi N \left(a + b\frac{\omega_n}{\omega_u} + \frac{\omega}{\omega_0}\right)\right]} \operatorname{sinc}\left\{ \pi N \left[a + b\frac{\omega_n}{\omega_u} + \frac{\omega}{\omega_0} \right] \right\} \Big\rangle \Bigg|^2$$

Clearly the brightness with the electric terms is much more different. First of all, it is quite easy to check that, if we take the limit $K_e \to 0$, we recover the usual definition of the brightness, with just the magnetic contribution. Also, now the *sinc* function has again the usual terms in the argument $a + \frac{\omega}{\omega_0}$, in which a plays the role of the harmonic number, but has also the term $b\omega_n/\omega_u$, which is a much smaller term compared to $1/g$, in the previous analysis. This term clearly move the resonance condition and allows the creation of further peaks around the original peak, centered at ω/ω_0. In order to give an idea of the contribution of the electric strength parameter, we give an example of its estimation. From

$$K_e = \frac{e_0 E}{m_0 c^2 k_r},$$

it is useful to rewrite the constants in a different way, using the following table and the fact that $k_r = 2\pi/\lambda_r$

Definitions

Velocity of light:	$c = 1/\sqrt{\epsilon_0 \mu_0}$	$2.997 \cdot 10^8$ m/s
Vacuum impedance:	$Z_0 = \sqrt{\mu_0/\epsilon_0} = 1/(c\epsilon_0)$	$377\,\Omega$
Alfvén current:	$I_A = e_0 c/r_0$	17040 A
Voltage $I_A Z_0$	$I_A Z_0 = 4\pi m_0 c^2/e_0$	$6.421 \cdot 10^6$ V
Electron classical radius:	$r_0 = (1/4\pi\epsilon_0)\, e_0^2/m_0 c^2$	$2.818 \cdot 10^{-15}$ m

So K_e will become

$$K_e = \frac{2E\lambda_r}{I_A Z_0}$$

Now, in order to evaluate the field quantity, we start from the power associated to the field, using the Poynting vector $\mathbf{S} = c^2 \epsilon_0 (\mathbf{E} \times \mathbf{B})$

$$P = c^2\epsilon_0\frac{1}{T}\int\limits_T\int\epsilon_0\left(\mathbf{E}\times\mathbf{B}\right)dSdt = \frac{1}{2}c\epsilon_0\Sigma_L\left|\eta\left(z,t\right)\right|^2 \quad \Rightarrow \quad \left|\eta\left(z,t\right)\right| = \sqrt{\frac{2P}{c\epsilon_0\Sigma_L}}$$

Therefore, assuming an energy of the radiation of $20\mu J$ and a pulse duration of $60fs$, one has $P = 20\cdot 10^{-6}/\left(60\cdot 10^{-15}\right) = 333MW$. Moreover with a cross-section of the beam up to $10^{-6}m^2$,we get $\left|\eta\left(z,t\right)\right| = 5\cdot 10^8\,V/m$.
For the K_e, we assume a lambda for the radiation up to $\lambda_r = 20\,nm$, so we get $K_e = 3.12\cdot 10^{-6}$

Bibliography

[1] Jialin Xie, Jiejia Zhuang, Yongzhang Huang, Yonggui Li, Shaobo Lin, Chengsheng Mao, Runjie Ying, Yuanyuan Zhong, Lingyi Zhang, Gang Wu, Yuzhen Zhang, Lihua Li, Ensheng Fu, and Weiren Liu. First lasing of the beijing fel. *Nuclear Inst. and Methods in Physics Research, A*, 341(1-3):34–38, 1994.

[2] U. Lehnert, P. Michel, W. Seidel, G. Staats, J. Teichert, and R. Wunsch. First experiences with the fir-fel at elbe. pages 97–100, 2007.

[3] P. Emma, R. Akre, J. Arthur, R. Bionta, C. Bostedt, J. Bozek, A. Brachmann, P. Bucksbaum, R. Coffee, F.-J. Decker, et al. First lasing and operation of an ångstrom-wavelength free-electron laser. *Nature Photonics*, 4:641–647, September 2010.

[4] T. Ishikawa, H. Aoyagi, T. Asaka, Y. Asano, N. Azumi, T. Bizen, H. Ego, K. Fukami, T. Fukui, Y. Furukawa, et al. A compact X-ray free-electron laser emitting in the sub-ångström region. *Nature Photonics*, 6:540–544, August 2012.

[5] E. Allaria, R. Appio, L. Badano, W. A. Barletta, S. Bassanese, S. G. Biedron, A. Borga, E. Busetto, D. Castronovo, P. Cinquegrana, S. Cleva, D. Cocco, M. Cornacchia, P. Craievich, I. Cudin, G. D'Auria, M. Dal Forno, M. B. Danailov, R. De Monte, G. De Ninno, P. Delgiusto, A. Demidovich, S. Di Mitri, B. Diviacco, A. Fabris, R. Fabris, W. Fawley, M. Ferianis, E. Ferrari, S. Ferry, L. Froehlich, P. Furlan, G. Gaio, F. Gelmetti, L. Giannessi, M. Giannini, R. Gobessi, R. Ivanov, E. Karantzoulis, M. Lonza, A. Lutman, B. Mahieu, M. Milloch, S. V. Milton, M. Musardo, I. Nikolov, S. Noe, F. Parmigiani, G. Penco, M. Petronio, L. Pivetta, M. Predonzani, F. Rossi, L. Rumiz, A. Salom, C. Scafuri, C. Serpico, P. Sigalotti, S. Spampinati, C. Spezzani, M. Svandrlik, C. Svetina, S. Tazzari, M. Trovo, R. Umer, A. Vascotto, M. Veronese, R. Visintini, M. Zaccaria, D. Zangrando, and M. Zangrando. Highly coherent and stable pulses from the FERMI seeded free-electron laser in the extreme ultraviolet. *Nature Photonics*, 6(10):699–704, 9 2012.

[6] L. Giannessi, E. Allaria, L. Badano, D. Castronovo, P. Cinquegrana, P. Craievich, M. Danailov, G. D'Auria, A. Demidovitch, et al. First

lasing of FERMI FEL-2 (1Â° Stage) and FERMI FEL-1 recent results. In *Proceedings of the 2012 FEL Conference, Nara, Japan*, page MOOB6, 2012.

[7] Alexander Malyzhenkov, Yunieski P. Arbelo, Paolo Craievich, Philipp Dijkstal, Eugenio Ferrari, Sven Reiche, Thomas Schietinger, Pavle Juranić, and Eduard Prat. Single- and two-color attosecond hard x-ray free-electron laser pulses with nonlinear compression. *Phys. Rev. Res.*, 2:042018, Oct 2020.

[8] S Schreiber. First Lasing at 32 nm of the VUV-FEL at DESY. 2005.

[9] Bernd Crasemann. *Atomic Inner-Shell Physics*. 2012.

[10] A Nazarkin, I Uschmann, E Forster, and R Sauerbrey. Coherent control of x-rays by laser-produced optical phonons and generation of extremely short x-ray pulses. *Applied Physics B*, 81(1):95–100, 2005.

[11] L. Giannessi, P. Musumeci, and S. Spampinati. Nonlinear pulse evolution in seeded free-electron laser amplifiers and in free-electron laser cascades. *Journal of Applied Physics*, 98(4):043110, 2005.

[12] L. Giannessi and P. Musumeci. The free-electron laser harmonic cascade. *New Journal of Physics*, 8(11):294–294, Nov 2006.

[13] L. Giannessi, M. Bellaveglia, E. Chiadroni, A. Cianchi, M. E. Couprie, M. Del Franco, G. Di Pirro, M. Ferrario, G. Gatti, M. Labat, et al. Superradiant cascade in a seeded free-electron laser. *Physical Review Letters*, 110:044801, Jan 2013.

[14] Najmeh S Mirian, Michele Di Fraia, Simone Spampinati, Filippo Sottocorona, Enrico Allaria, Laura Badano, Miltcho B Danailov, Alexander Demidovich, Giovanni De Ninno, Simone Di Mitri, Giuseppe Penco, Primož Rebernik Ribič, Carlo Spezzani, Giulio Gaio, Mauro Trovò, Nicola Mahne, Michele Manfredda, Lorenzo Raimondi, Marco Zangrando, Oksana Plekan, Kevin C Prince, Tommaso Mazza, Richard J Squibb, Carlo Callegari, Xi Yang, and Luca Giannessi. Generation and measurement of intense few-femtosecond superradiant extreme-ultraviolet free-electron laser pulses. *Nature Photonics*, 15(7):523–529, 2021.

[15] P. Emma, K. Bane, M. Cornacchia, Z. Huang, H. Schlarb, G. Stupakov, and D. Walz. Femtosecond and subfemtosecond x-ray pulses from a self-amplified spontaneous-emission based free-electron laser. *Physical Review Letters*, 92(7):074801, February 2004.

[16] P. Corkum and Zenghu Chang. The attosecond revolution. *Optics and Photonics News - OPT PHOTONICS NEWS*, 19, 10 2008.

[17] M Drescher, M Hentschel, R Kienberger, M Uiberacker, V. Yakovlev, A Scrinzi, Th Westerwalbesloh, Ulf Kleineberg, U Heinzmann, and F Krausz. Time-resolved atomic inner-shell spectroscopy. *Nature*, 419:803–7, 11 2002.

[18] M Uiberacker, Th Uphues, M Schultze, AJ Verhoef, V Yakovlev, MF Kling, J Rauschenberger, NM Kabachnik, H Schroder, M Lezius, KL Kompa, H-G Muller, M J J Vrakking, S Hendel, U Kleineberg, U Heinzmann, M Drescher, and F Krausz. Attosecond real-time observation of electron tunnelling in atoms. *Nature*, 446(7136):627–632, April 2007.

[19] M. Schultze, M. Fiess, N. Karpowicz, J. Gagnon, M. Korbman, M. Hofstetter, S. Neppl, A. L. Cavalieri, Y. Komninos, Th. Mercouris, C. A. Nicolaides, R. Pazourek, S. Nagele, J. Feist, J. Burgdorfer, A. M. Azzeer, R. Ernstorfer, R. Kienberger, U. Kleineberg, E. Goulielmakis, F. Krausz, and V. S. Yakovlev. Delay in photoemission. *Science*, 328(5986):1658–1662, 2010.

[20] K. Klünder, J. M. Dahlström, M. Gisselbrecht, T. Fordell, M. Swoboda, D. Guénot, P. Johnsson, J. Caillat, J. Mauritsson, A. Maquet, R. Tajeb, and A. L'Huillier. Probing single-photon ionization on the attosecond time scale. *Phys. Rev. Lett.*, 106:143002, Apr 2011.

[21] Eleftherios Goulielmakis, Zhi-Heng Loh, Adrian Wirth, Robin Santra, Nina Rohringer, Vladislav S Yakovlev, Sergey Zherebtsov, Thomas Pfeifer, Abdallah M Azzeer, Matthias F Kling, Stephen R Leone, and Ferenc Krausz. Real-time observation of valence electron motion. *Nature*, 466(7307):739–743, August 2010.

[22] Franck Lepine, Misha Y. Ivanov, and Marc J. J. Vrakking. Attosecond molecular dynamics: fact or fiction? *Nature Photonics*, 8(3):195–204, March 2014.

[23] G Sansone, F Kelkensberg, JF Perez-Torres, F Morales, MF Kling, W Siu, O Ghafur, P Johnsson, M Swoboda, E Benedetti, F Ferrari, F Lepine, JL Sanz-Vicario, S Zherebtsov, I Znakovskaya, A L'huillier, M Yu Ivanov, M Nisoli, F MartÃn, and M J J Vrakking. Electron localization following attosecond molecular photoionization. *Nature*, 465(7299):763–766, June 2010.

[24] F. Kelkensberg, W. Siu, J. F. Perez-Torres, F. Morales, G. Gademann, A. Rouzee, P. Johnsson, M. Lucchini, F. Calegari, J. L. Sanz-Vicario, F. Martin, and M. J. J. Vrakking. Attosecond control in photoionization of hydrogen molecules. *Phys. Rev. Lett.*, 107:043002, Jul 2011.

[25] W. Siu, F. Kelkensberg, G. Gademann, A. Rouzée, P. Johnsson, D. Dowek, M. Lucchini, F. Calegari, U. De Giovannini, A. Rubio, R. R. Lucchese,

H. Kono, F. Lépine, and M. J. J. Vrakking. Attosecond control of dissociative ionization of o_2 molecules. *Phys. Rev. A*, 84:063412, Dec 2011.

[26] Predrag Ranitovic, Craig W Hogle, Paula Riviere, Alicia Palacios, Xiao-Ming Tong, Nobuyuki Toshima, Alberto Gonzalez-Castrillo, Leigh Martin, Fernando Martin, Margaret M Murnane, and Henry Kapteyn. Attosecond vacuum uv coherent control of molecular dynamics. *Proceedings of the National Academy of Sciences of the United States of America*, 111(3):912–917, January 2014.

[27] F. Calegari, D. Ayuso, A. Trabattoni, L. Belshaw, S. De Camillis, S. Anumula, F. Frassetto, L. Poletto, A. Palacios, P. Decleva, J. B. Greenwood, F. Martin, and M. Nisoli. Ultrafast electron dynamics in phenylalanine initiated by attosecond pulses. *Science*, 346(6207):336–339, oct 2014.

[28] J. B. Rosenzweig, D. Alesini, G. Andonian, M. Boscolo, M. Dunning, L. Faillace, M. Ferrario, A. Fukusawa, L. Giannessi, E. Hemsing, et al. Generation of ultra-short, high brightness electron beams for single-spike sase fel operation. *Nuclear Instruments and Methods in Physics Research Section A: Accelerators, Spectrometers, Detectors and Associated Equipment*, 593(1-2):39–44, Aug 2008.

[29] A. A. Zholents and G. Penn. Obtaining attosecond x-ray pulses using a self-amplified spontaneous emission free electron laser. *Phys. Rev. ST Accel. Beams*, 8(5):050704, May 2005.

[30] Joseph Duris, Siqi Li, Taran Driver, Elio G Champenois, James P MacArthur, Alberto A Lutman, Zhen Zhang, Philipp Rosenberger, Jeff W Aldrich, Ryan Coffee, et al. Tunable isolated attosecond x-ray pulses with gigawatt peak power from a free-electron laser. *Nature Photonics*, 14(1):30–36, 2020.

[31] A. Marinelli et al. Optical shaping of x-ray free-electron lasers. *Physical Review Letters*, 116:254801, Jun 2016.

[32] E. L. Saldin, E. A. Schneidmiller, and M. V. Yurkov. Self-amplified spontaneous emission fel with energy-chirped electron beam and its application for generation of attosecond x-ray pulses. *Phys. Rev. ST Accel. Beams*, 9:050702, May 2006.

[33] L. Giannessi, A. Bacci, M. Bellaveglia, F. Briquez, M. Castellano, E. Chiadroni, A. Cianchi, F. Ciocci, M. E. Couprie, L. Cultrera, et al. Self-amplified spontaneous emission free-electron laser with an energy-chirped electron beam and undulator tapering. *Physical Review Letters*, 106:144801, Apr 2011.

[34] Donna Strickland and Gerard Mourou. Compression of amplified chirped optical pulses. *Optics Communications*, 56(3):3, dec 1985.

[35] D. Umstadter, L.H. Yu, E. Johnson, and D. Li. Ultrashort ultraviolet free-electron lasers. *Journal of X-Ray Science and Technology*, 4(4):263–274, 1994.

[36] David Gauthier, Enrico Allaria, Marcello Coreno, Ivan Cudin, Hugo Dacasa, Miltcho Boyanov Danailov, Alexander Demidovich, Simone Di Mitri, Bruno Diviacco, Eugenio Ferrari, et al. Chirped pulse amplification in an extreme-ultraviolet free-electron laser. *Nature Communications*, 7:13688, 12 2016.

[37] H. Motz. Applications of the radiation from fast electron beams. *Journal of Applied Physics*, 22(5):527–535, 1951.

[38] Peter Schmueser, Joerg Rossbach, and Martin Dohlus. *Ultraviolet and soft X-ray free-electron lasers. Introduction to physical principles, experimental results, technological challenges.* Jul 2008.

[39] John David Jackson. *Classical electrodynamics.* Wiley, New York, NY, 3rd ed. edition, 1999.

[40] W. Colson. The nonlinear wave equation for higher harmonics in free-electron lasers. *IEEE Journal of Quantum Electronics*, 17(8):1417–1427, Aug 1981.

[41] Luca Giannessi. *Seeding and Harmonic Generation in Free-Electron Lasers*, pages 1–27. Springer International Publishing, Cham, 2014.

[42] H. Haus. Noise in free-electron laser amplifier. *IEEE Journal of Quantum Electronics*, 17(8):1427–1435, Aug 1981.

[43] G. Dattoli, A. Marino, A. Renieri, and F. Romanelli. Progress in the hamiltonian picture of the free-electron laser. *IEEE Journal of Quantum Electronics*, 17(8):1371–1387, Aug 1981.

[44] R. Bonifacio, C. Pellegrini, and L. M. Narducci. Collective instabilities and high-gain regime in a free electron laser. *Optics Communications*, 50(6):373–378, Jul 1984.

[45] S. Reiche. GENESIS 1.3: a fully 3D time-dependent FEL simulation code. *Nuclear Instruments and Methods in Physics Research Section A: Accelerators, Spectrometers, Detectors and Associated Equipment*, 429(1-3):243–248, Jun 1999.

[46] Ming Xie. Design optimization for an x-ray free electron laser driven by SLAC linac. In *Proceedings Particle Accelerator Conference*, volume 1, pages 183–185. IEEE, May 1995.

[47] E. L. Saldin, E. A. Schneidmiller, and M. V. Yurkov. Statistical properties of radiation from vuv and x-ray free electron laser. *Optics Communications*, 148(4-6):383–403, Mar 1998.

[48] Zhirong Huang and Kwang-Je Kim. Review of x-ray free-electron laser theory. *Phys. Rev. ST Accel. Beams*, 10:034801, Mar 2007.

[49] Wilfried Wurth. *Characterization of the Time Structure of Free-Electron Laser Radiation*, pages 865–889. Springer International Publishing, Cham, 2016.

[50] I. Boscolo and V. Stagno. The converter and the transverse optical klystron. *Nuovo Cimento B*, 58(2):267–285, 1980.

[51] R. Bonifacio, L. De Salvo Souza, P. Pierini, and E. T. Scharlemann. Generation of xuv light by resonant frequency tripling in a two-wiggler fel amplifier. In *Free Electron Laser Conference, 1989. Proceedings of the Eleventh International*, pages 787–790, Aug 1989.

[52] R. Barbini, F. Ciocci, G. Dattoli, A. Dipace, L. Giannessi, G. Maino, C. Mari, C. Marina, C. Ronsivalle, E. Sabia, and A. Torre. 80 nm fel design in an oscillator amplifier configuration, in proceedings of the prospects for a 1 a free electron laser, sag harbor, new york, april 22-27, j. c. gallardo editor (bnl 52273). In *Proceedings of the Prospects for a 1 A Free Electron Laser, Sag Harbor, New York, April 22-27, J. C. Gallardo Editor (BNL 52273)*, 1990.

[53] L. H. Yu. Generation of intense uv radiation by subharmonically seeded single-pass free-electron lasers. *Physical Review A*, 44:5178, 1991.

[54] L.-H. Yu, M. Babzien, I. Ben-Zvi, L. F. DiMauro, A. Doyuran, W. S. Graves, E. D. Johnson, S. Krinsky, R. Malone, I. Pogorelsky, J. Skaritka, G. Rakowsky, L. Solomon, X. J. Wang, M. Woodle, V. Yakimenko, S. G. Biedron, J. N. Galayda, E. Gluskin, J. Jagger, V. Sajaev, and I. Vasserman. High-gain harmonic-generation free-electron laser. *Science*, 289(5481):932–934, Aug 2000.

[55] L. H. Yu, L. DiMauro, A. Doyuran, W. S. Graves, E. D. Johnson, R. Heese, S. Krinsky, H. Loos, J. B. Murphy, G. Rakowsky, J. Rose, T. Shaftan, B. Sheehy, J. Skaritka, X. J. Wang, and Z. Wu. First ultraviolet high-gain harmonic-generation free-electron laser. *Physical Review Letters*, 91(7):074801, Aug 2003.

[56] E. Allaria, R. Appio, L. Badano, W. A. Barletta, S. Bassanese, S. G. Biedron, P. Bolognesi, C. Bracco, F. Braico, M. Carpanese, M. Castellano, D. Castronovo, P. Cinquegrana, M. B. Danailov, R. De Monte, A. Demidovich, S. Di Mitri, B. Diviacco, A. Fabris, W. M. Fawley, E. Ferrari, F. Frassetto, G. Gaio, G. Gatti, L. Giannessi, L. Giannessi, D. Giove, F. Greer, R. Ivanov, G. Kurdi, A. A. Lutman, B. Mahieu, M. Milloch, S. V. Milton, M. Musardo, I. Nikolov, F. Parmigiani, G. Penco, C. Pellegrini, E. Polo, L. Raimondi, P. Rebernik, F. Rossi, L. Rumiz, C. Scafuri, C. Serpico, P. Sigalotti, S. Spampinati, C. Spezzani, P. Sutcliffe,

M. Trovo, M. Umer, A. Vascotto, M. Veronese, M. Zaccaria, D. Zangrando, B. Zaniol, and M. Zangrando. High-gain harmonic-generation free-electron laser seeded by harmonics generated in gas. *Physical Review Letters*, 107:224801, 2011.

[57] M. Labat, M. Bellaveglia, M. Bougeard, B. Carré, F. Ciocci, E. Chiadroni, A. Cianchi, M. E. Couprie, L. Cultrera, M. Del Franco, G. Di Pirro, A. Drago, M. Ferrario, D. Filippetto, F. Frassetto, A. Gallo, D. Garzella, G. Gatti, L. Giannessi, G. Lambert, A. Mostacci, A. Petralia, V. Petrillo, L. Poletto, M. Quattromini, J. V. Rau, C. Ronsivalle, E. Sabia, M. Serluca, I. Spassovsky, V. Surrenti, C. Vaccarezza, and C. Vicario. High-gain harmonic-generation free-electron laser seeded by harmonics generated in gas. *Physical Review Letters*, 107:224801, Nov 2011.

[58] James P. Cryan, Joseph Duris, Marc W. Guetg, Zhirong Huang, Jacek Krzywinski, Henrik Loos, Agostino Marinelli, Juhao Wu, Alberto A. Lutman, Ryan Coffee, Georgi L. Dakovski, Yuantao Ding, David H. Dowell, Alan S. Fisher, Alan R. Fry, Sasha Gilevich, Philippe Hering, W. H. Huang, Hartawan Laksmono, Henrik T. Lemke, H. Li, Timothy J. Maxwell, Ankush Mitra, Stefan Moeller, Shawn Osier, Franz Peters, William F. Schlotter, Joshua J. Turner, and Diling Zhu. Seeding the harmonic cascade of a free-electron laser amplifier. *Physical Review Letters*, 105:214801, 2010.

[59] E. Allaria, L. Badano, S. Bassanese, F. Capotondi, D. Castronovo, P. Cinquegrana, M. B. Danailov, G. D'Auria, A. Demidovich, R. De Monte, G. De Ninno, S. Di Mitri, B. Diviacco, W. M. Fawley, M. Ferianis, E. Ferrari, G. Gaio, D. Gauthier, L. Giannessi, F. Iazzourene, G. Kurdi, N. Mahne, I. Nikolov, F. Parmigiani, G. Penco, L. Raimondi, P. Rebernik, F. Rossi, E. Roussel, C. Scafuri, C. Serpico, P. Sigalotti, C. Spezzani, M. Svandrlik, C. Svetina, M. Trovó, M. Veronese, D. Zangrando, and M. Zangrando. The FERMI free-electron lasers. *Journal of Synchrotron Radiation*, 22(3):485–491, May 2015.

[60] E. Allaria, B. Diviacco, C. Callegari, P. Finetti, B. Mahieu, J. Viefhaus, M. Zangrando, G. De Ninno, G. Lambert, E. Ferrari, J. Buck, M. Ilchen, B. Vodungbo, N. Mahne, C. Svetina, C. Spezzani, S. Di Mitri, G. Penco, M. Trovò, W. M. Fawley, P. R. Rebernik, D. Gauthier, C. Grazioli, M. Coreno, B. Ressel, A. Kivimäki, T. Mazza, L. Glaser, F. Scholz, J. Seltmann, P. Gessler, J. Grüunert, A. De Fanis, M. Meyer, A. Knie, S. P. Moeller, L. Raimondi, F. Capotondi, E. Pedersoli, O. Plekan, M. B. Danailov, A. Demidovich, I. Nikolov, A. Abrami, J. Gautier, J. Lüning, P. Zeitoun, and L. Giannessi. Control of the polarization of a vacuum-ultraviolet, high-gain, free-electron laser. *Physical Review X*, 4(4), dec 2014.

[61] E. Ferrari, E. Allaria, J. Buck, G. De Ninno, B. Diviacco, D. Gauthier, L. Giannessi, L. Glaser, Z. Huang, M. Ilchen, G. Lambert, A. A. Lutman,

B. Mahieu, G. Penco, C. Spezzani, and J. Viefhaus. Single shot polarization characterization of xuv fel pulses from crossed polarized undulators. *Sci. Rep.*, 5:13531, Aug 2015.

[62] Giovanni De Ninno, David Gauthier, Benoît Mahieu, Primož Rebernik Ribič, Enrico Allaria, Paolo Cinquegrana, Miltcho Bojanov Danailov, Alexander Demidovich, Eugenio Ferrari, Luca Giannessi, Giuseppe Penco, Paolo Sigalotti, and Matija Stupar. Single-shot spectro-temporal characterization of XUV pulses from a seeded free-electron laser. *Nature Communications*, 6(1):8075, aug 2015.

[63] David Gauthier, Benoît Mahieu, Primož Rebernik Ribič, Enrico Allaria, Paolo Cinquegrana, Miltcho Bojanov Danailov, Alexander Demidovich, Eugenio Ferrari, Luca Giannessi, Giuseppe Penco, et al. Single-shot spectro-temporal characterization of xuv pulses from a seeded free-electron laser. 2015.

[64] E. Allaria, D. Castronovo, P. Cinquegrana, P. Craievich, M. Dal Forno, M. B. Danailov, G. D'Auria, A. Demidovich, G. De Ninno, S. Di Mitri, and et al. Two-stage seeded soft-x-ray free-electron laser. *Nature Photonics*, 7(11):913–918, Oct 2013.

[65] G. De Ninno, B. Mahieu, E. Allaria, L. Giannessi, and S. Spampinati. Chirped seeded free-electron lasers: Self-standing light sources for two-color pump-probe experiments. *Physical Review Letters*, 110:064801, Feb 2013.

[66] B. Mahieu, E. Allaria, D. Castronovo, M. B. Danailov, A. Demidovich, G. De Ninno, S. Di Mitri, W. M. Fawley, E. Ferrari, L. Fröhlich, et al. Two-colour generation in a chirped seeded free-electron laser: a close look. *Optics Express*, 21:22728, 2013.

[67] P. Finetti, H. Höppner, E. Allaria, C. Callegari, F. Capotondi, P. Cinquegrana, M. Coreno, R. Cucini, M. B. Danailov, A. Demidovich, et al. Pulse duration of seeded free-electron lasers. *Physical Review X*, 7(2):021043, 2017.

[68] Milton Abramowitz and Irene A. Stegun. *Handbook of Mathematical Functions with Formulas, Graphs, and Mathematical Tables.* Dover, New York, ninth dover printing, tenth gpo printing edition, 1964.

[69] M. Labat, N. Joly, S. Bielawski, C. Szwaj, C. Bruni, and M. E. Couprie. Pulse splitting in short wavelength seeded free electron lasers. *Phys. Rev. Lett.*, 103:264801, Dec 2009.

[70] Eugenio Ferrari, Carlo Spezzani, Franck Fortuna, Renaud Delaunay, Franck Vidal, Ivaylo Nikolov, Paolo Cinquegrana, Bruno Diviacco, David Gauthier, Giuseppe Penco, et al. Widely tunable two-colour seeded free-electron laser source for resonant-pump resonant-probe magnetic scattering. *Nature Communications*, 7:10343, 2016.

[71] C.J. Bocchetta and et al. Fermi@elettra cdr. 2007.

[72] Luigi Faillace. Recent advancements of rf guns. *Physics Procedia*, 52:100–109, 12 2014.

[73] Z. Huang, M. Borland, P. Emma, J. Wu, C. Limborg, G. Stupakov, and J. Welch. Suppression of microbunching instability in the linac coherent light source. *Phys. Rev. ST Accel. Beams*, 7:074401, Jul 2004.

[74] I. Ben-Zvi, K. M. Yang, and L. H. Yu. The "fresh-bunch" technique in FELS. *Nuclear Instruments and Methods in Physics Research A*, 318:726–729, Jul 1992.

[75] L.-H. Yu and I. Ben-Zvi. High-gain harmonic generation of soft X-rays with the "fresh bunch" technique. *Nuclear Instruments and Methods in Physics Research A*, 393:96–99, Feb 1997.

[76] L. Giannessi, C. Masciovecchio, and et al. Fermi@elettra cdr. 2021.

[77] E. Allaria, F. Bencivenga, R. Borghes, F. Capotondi, D. Castronovo, P. Charalambous, P. Cinquegrana, M. B. Danailov, G. De Ninno, A. Demidovich, S. di Mitri, B. Diviacco, D. Fausti, W. M. Fawley, E. Ferrari, L. Froehlich, D. Gauthier, A. Gessini, L. Giannessi, R. Ivanov, M. Kiskinova, G. Kurdi, B. Mahieu, N. Mahne, I. Nikolov, C. Masciovecchio, E. Pedersoli, G. Penco, L. Raimondi, C. Serpico, P. Sigalotti, S. Spampinati, C. Spezzani, C. Svetina, M. Trovò, and M. Zangrando. Two-colour pump-probe experiments with a twin-pulse-seed extreme ultraviolet free-electron laser. *Nature Communications*, 4(1):2476, September 2013.

[78] M. Labat, N. Joly, S. Bielawski, C. Szwaj, C. Bruni, and M. E. Couprie. Pulse splitting in short wavelength seeded free electron lasers. *Physical Review Letters*, 103:264801, Dec 2009.

[79] N.S. Mirian, S. Spampinati, and L. Giannessi. Fel pulse shortening by superradiance at fermi. pages 38–41, 2017.

[80] G. Perosa et al. Transversally Separated Crossed Polarized FEL Subpulses. presented at FEL2022, Triest, Italy, Aug. 2022, paper TUP76, unpublished.

[81] G. Penco, G. Perosa, E. Allaria, and et al. Nonlinear harmonics of a seeded free-electron laser as a coherent and ultrafast probe to investigate matter at the water window and beyond. *Physical Review A*, 105(5), 2022.

[82] R. H. Dicke. Coherence in spontaneous radiation processes. *Physical Review*, 93(1):99–110, jan 1954.

[83] R. Bonifacio and F. Casagrande. The superradiant regime of a free electron laser. *Nucl. Instrum. Methods Phys. Res. A*, 239(1):36–42, aug 1985.

[84] R. Bonifacio, L. De Salvo Souza, P. Pierini, and N. Piovella. The superradiant regime of a fel: Analytical and numerical results. *Nuclear Instruments and Methods in Physics Research Section A: Accelerators, Spectrometers, Detectors and Associated Equipment*, 296(1-3):358–367, Oct 1990.

[85] R. Bonifacio, F. Casagrande, G. Cerchioni, L. De Salvo Souza, P. Pierini, and N. Piovella. Physics of the high-gain fel and superradiance. *Rivista del Nuovo Cimento*, 13(9):1–69, 1990.

[86] R. Bonifacio, N. Piovella, and B. W. J. McNeil. Superradiant evolution of radiation pulses in a free-electron laser. *Physical Review A*, 44(6):R3441–R3444, sep 1991.

[87] R. Bonifacio, C. Maroli, and N. Piovella. Slippage and superradiance in the high-gain fel: Linear theory. *Optics Communications*, 68(5):369–374, 1988.

[88] T. Watanabe, X. J. Wang, J. B. Murphy, J. Rose, Y. Shen, T. Tsang, L. Giannessi, P. Musumeci, and S. Reiche. Experimental characterization of superradiance in a single-pass high-gain laser-seeded free-electron laser amplifier. *Physical Review Letters*, 98:034802, Jan 2007.

[89] D. A. Jaroszynski, P. Chaix, N. Piovella, D. Oepts, G. M. H. Knippels, A. F. G. van der Meer, and H. H. Weits. Superradiance in a short-pulse free-electron-laser oscillator. *Phys. Rev. Lett.*, 78:1699–1702, Mar 1997.

[90] Xi Yang, Najmeh Mirian, and Luca Giannessi. Postsaturation dynamics and superluminal propagation of a superradiant spike in a free-electron laser amplifier. *Physical Review Accelerators and Beams*, 23(1):010703, jan 2020.

[91] M. Zangrando et al. Recent results of PADReS, the photon analysis delivery and reduction system, from the FERMI FEL commissioning and user operations. *J. Synchr. Rad.*, 22:565, 2015.

[92] R. Mitzner, A. A. Sorokin, B. Siemer, S. Roling, M. Rutkowski, H. Zacharias, M. Neeb, T. Noll, F. Siewert, W. Eberhardt, M. Richter, P. Juranic, K. Tiedtke, and J. Feldhaus. Direct autocorrelation of soft-x-ray free-electron-laser pulses by time-resolved two-photon double ionization of he. *Physical Review A*, 80(2):025402, aug 2009.

[93] Cristian Svetina, Cesare Grazioli, Nicola Mahne, Lorenzo Raimondi, Claudio Fava, Marco Zangrando, Simone Gerusina, Michele Alagia, Lorenzo Avaldi, Giuseppe Cautero, Monica de Simone, Michele Devetta, Michele Di Fraia, Marcel Drabbels, Vitaliy Feyer, Paola Finetti, Raphael Katzy, Antti Kivimäki, Viktor Lyamayev, Tommaso Mazza, Angelica Moise, Thomas Möller, Patrick O'Keeffe, Yevheniy Ovcharenko, Paolo Piseri, Oksana Plekan, Kevin C. Prince, Rudi Sergo, Frank Stienkemeier,

Stefano Stranges, Marcello Coreno, and Carlo Callegari. The low density matter (ldm) beamline at FERMI: optical layout and first commissioning. *Journal of Synchrotron Radiation*, 22(3):538–543, apr 2015.

[94] Orazio Svelto and David C Hanna. Principles of lasers. 1, 2010.

[95] Anthony E Siegman. *Lasers*. University Science Books, 1986.

[96] E. Allaria, G. De Ninno, and C. Spezzani. Experimental demonstration of frequency pulling in single-pass free-electron lasers. *Opt. Express*, 19(11):10619–10624, May 2011.

[97] E. Allaria, M. Danailov, and G. De Ninno. Tunability of a seeded free-electron laser through frequency pulling. *Europhysics Letters*, 89(6):64005, apr 2010.

[98] E.L. Saldin, E.A. Schneidmiller, and M.V. Yurkov. The features of an fel oscillator with a tapered undulator. *Optics Communications*, 103(3-4):297–306, 1993.

[99] William M. Fawley, Zhirong Huang, Kwang-Je Kim, and Nikolai A. Vinokurov. Tapered undulators for sase fels. *Nuclear Instruments and Methods in Physics Research, Section A: Accelerators, Spectrometers, Detectors and Associated Equipment*, 483(1-2):537–541, 2002.

[100] W.B. Colson and R.D. McGinnis. The free electron laser with inverse taper. *Nuclear Instruments and Methods in Physics Research, Section A: Accelerators, Spectrometers, Detectors and Associated Equipment*, 445(1-3):49–52, 2000.

[101] Daniel Ratner, Alex Chao, and Zhirong Huang. Enhancing fel power with phase shifters. pages 69–72, 2007.